Universiteit Gent
Faculteit Toegepaste Wetenschappen
Vakgroep Informatietechnologie

# Leaky-Waveguide-Based Integrated Spot-Size Converters for Alignment-Tolerant Optical Fiber Coupling

Marko Galarza Galarza

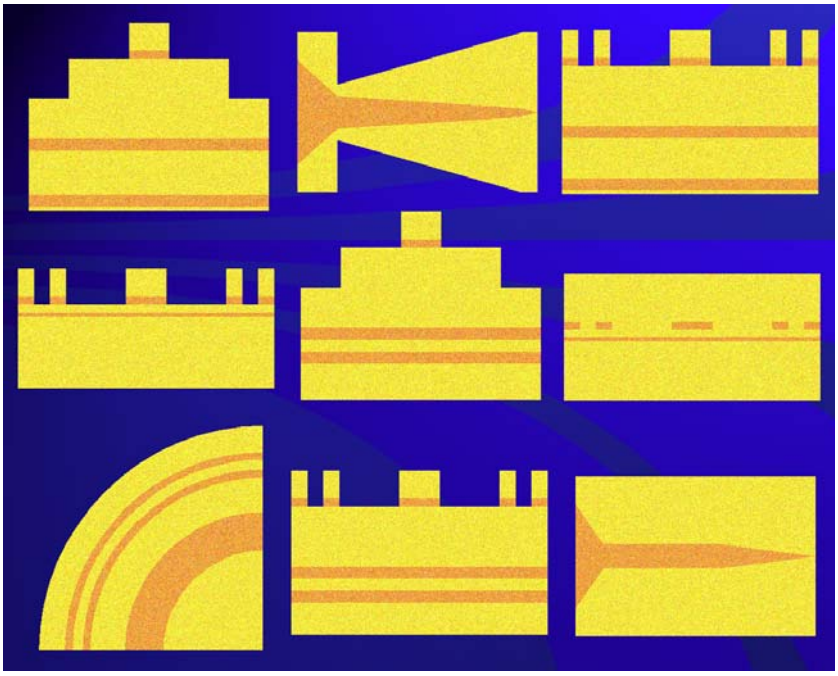

In collaboration with

Universidad Pública de Navarra
*Nafarroako Unibertsitate Publikoa*

A Dissertation for the Degree of
Doctor in Applied Sciences
Academic Year 2002-2003

**Promotors**:

| | |
|---|---|
| Prof. Roel Baets | INTEC, Ghent University, Belgium |
| Prof. Manuel López-Amo | IEE, Public University of Navarre, Spain |
| Dr. Ir. Cándido Aramburu | IEE, Public University of Navarre, Spain |

**Examining Committee**:

| | |
|---|---|
| Prof. Jan Van Campenhout | ELIS, Ghent University, Belgium |
| Prof. Jos Van Der Tol | TU Eindhoven, Holland |
| Prof. Patrick De Visschere | ELIS, Ghent University, Belgium |
| Prof. Paul Lagasse | INTEC, Ghent University, Belgium |
| Prof. Ingrid Moerman | INTEC, Ghent University, Belgium |
| Dr. Ir. Dries Van Thourhout | INTEC, Ghent University, Belgium |

Ghent University
Faculty of Applied Sciences

Department of Information Technology (INTEC)
Sint-Pietersnieuwstraat 41
B-9000 Ghent
Belgium

Tel.: +32 92643316
Fax.: +32 92643593

Amatxo ta Nereari

# Acknowledgments

The present dissertation is the result of the collaboration between the Department of Information Technology of the University of Ghent, and the Electric and Electronic Department of the Public University of Navarre. Therefore, I would like to thank Professors P. Lagasse and Manuel López-Amo, the heads of both departments, for providing the needed infrastructure and the possibility of a dynamic cooperation.
I want to express my gratitude towards Professors Roel Baets, Manuel López-Amo and Cándido Aramburu for their guidance, motivation and direction during the realization of this PhD thesis. I am grateful to them for kindling in me a strong interest for integrated optics, and for their vision in guiding this thesis work.
Obviously, I would like to acknowledge the Public University of Navarre, as well as the Government of Navarre for their support through a doctoral fellowship. This work has also been partially supported by the Spanish CICYT under Projects TIC2001-0877-C02-02 and TIC98-397-C03.
My thanks to the University of Ghent for allowing me to finish this doctorate study and to submit it to the Faculty of Engineering.
I would like to thank each member of the OMC and OTE groups of INTEC, headed by Professors Ingrid Moerman and Peter Van Daele, respectively, for the growth and processing of the components. Special mention for Steven Verstuyft, the main responsible person of processing activities.
Special thanks for Kurt De Mesel for his support and help during all these years. Certainly, this PhD thesis would not have been the same without his invaluable suggestions (and corrections).
Of course, I will not (ever) forget Tom Van Caenegem, who made possible the beginning of this fruitful collaboration and who always has had priceless advices for me.
Ik zou ook graag de OCS-groep van INTEC, geleid door professor Roel Baets, vermelden. Het was een plezier om samen te werken met zo'n vriendelijke, competente en vaak ook grappige groep mensen die altijd klaar stonden om onbaatzuchtig te helpen als het nodig was. Ik heb heel wat dingen geleerd van hen.

Tesi hau egiterakoan, België ezagutzeko aukera izan dut. Batez ere bere jendeak, jatorrak eta zabalak, oso zabalak. Hain herri txikia izatean ohituta daude inguruko herrialdeko jendeekin elkarbizitzen eta lanegiten. Oso oroimen ona eta polita utzi behar naute. Pensatzen dut luzerako izango dela. Egin ditugun lagunak bezalaxe...

Marko Galarza Galarza

Ghent, December, 2002

# Contents

## List of Publications Included in the Thesis

[A] M. Galarza, K. De Mesel, D. Fuentes, R. Baets, M. López-Amo, "Modeling of InGaAsP–InP 1.55 $\mu$m lasers with integrated mode expanders using fiber matched leaky waveguides", *Appl. Phys. B–Lasers Opt.*, vol. 73, no. 5–6, pp. 585–588, Oct. 2001.

[B] M. Galarza, K. De Mesel, S. Verstuyft, C. Aramburu, I. Moerman, P. Van Daele, R. Baets, M. López-Amo, "1.55 $\mu$m InP–InGaAsP Fabry-Pérot lasers with integrated spot size converters using antiresonant reflecting optical waveguides", *IEEE Photon. Technol. Lett.*, vol. 14, no. 8, pp. 1043–1045, Aug. 2002.

[C] M. Galarza, K. De Mesel, S. Verstuyft, C. Aramburu, M. López-Amo, I. Moerman, P. Van Daele, R. Baets, "Mode-expanded 1.55 $\mu$m InP–InGaAsP Fabry-Pérot lasers using ARROW waveguides for efficient fiber coupling", *IEEE J. Sel. Top. Quantum Electron.*, Accepted for publication, Nov./Dec. 2002.

[D] M. Galarza, K. De Mesel, T. Van Caenegem, S. Verstuyft, C. Aramburu, I. Moerman, P. Van Daele, R. Baets, M. López-Amo, "InGaAsP–InP 1.55 $\mu$m lasers with integrated mode expanders using fiber-matched leaky waveguides", *LEOS '01 Annual Meeting*, San Diego, California, USA, pp. 798–799, Nov. 2001.

[E] M. Galarza, K. De Mesel, S. Verstuyft, C. Aramburu, M. López-Amo, I. Moerman, P. Van Daele, R. Baets, "A new spot-size converter concept using fiber-matched antiresonant reflecting optical waveguides", *J. Lightwave Technol.*, vol. 21, no. 1, Jan. 2003.

[F] M. Galarza, K. De Mesel, A. Martínez, C. Aramburu, M. López-Amo, R. Baets, "Compact spot-size converters using fiber-matched antiresonant reflecting optical waveguides", Submitted to *Applied Optics*, Nov. 2002.

[G] M. Galarza, K. De Mesel, I. Christiaens, C. Aramburu, M. López-Amo, R. Baets, "Simple low-loss waveguide bends using ARROW effect", Submitted to *Optics Letters*, Nov. 2002.

# Chapter 1
# Introduction

The explosion in demand for network bandwidth is largely due to the growth in data traffic, specifically Internet Protocol (IP) based traffic. Leading service providers report bandwidths doubling on their backbones about every six to nine months. This is largely in response to the 300 percent growth per year in Internet traffic, while traditional voice traffic grows at a compound annual rate of only about 13 percent. This high demand—coupled with high usage rates, a deregulated telecommunications environment, and high availability requirements—is rapidly depleting the capacities of fibers that, when installed 10 years ago, were expected to suffice for the foreseeable future.

## 1.1 Fiber Optic Transmission

Light has an information-carrying capacity 10.000 times greater than the highest radio frequencies. Additional advantages of fiber over copper include the ability to carry signals over long distances, low error rates, immunity to electrical interference, security, and light weight.

Aware of these characteristics, researchers in the mid-1960's proposed that optical fiber might be a suitable transmission medium. There was an obstacle, however, that was the attenuation seen in the glass they were working with. In 1970 Corning produced the first communication-grade fibers with attenuation less than 20 dB/km.

AT&T first standardized transmission at 45 Mbps for multimode fibers (MMF). Soon thereafter, single-mode fibers (SMF) were shown to be capable of transmission rates 10 times that of the older type. In the early 1980's, MCI, followed by Sprint, adopted single-mode fibers for its long-distance network in the U.S.

Further developments in fiber optics are closely tied to the use of the specific regions on the optical spectrum where optical attenuation is low. These *transmission windows*, lie between areas of high absorption. The earliest systems were developed to operate around 850 nm, the first window in silica-based optical fiber. A second window at 1310 nm, soon proved to be superior because of its lower attenuation, followed by a third window at 1550 nm with an even lower optical loss.

The next step in the evolution of fiber optical communications was the development of erbium-doped fiber amplifiers (EDFA) that can provide high amplification of the signal in the third window. Today, a fourth window near 1625 nm is under development and early deployment, thanks to a modification of the amplifier design. Raman amplifiers are already being the next evolution step in optically amplified transmission systems since they are capable of providing gain over the entire transmission window of optical fibers.

### 1.1.1 Mutiplexing Techniques

Until the end of the 1990's the capacity of the optical fiber was exploited by means of electronic time division multiplexing (ETDM). However, the electronic circuitry that makes this possible is complex and costly, both to purchase and to maintain. The alternate solution is to increase the number of wavelengths in the SMF fiber. Using wavelength division multiplexing (WDM) technology several wavelengths, or light colors, can simultaneously multiplex signals of 2.5 to 40 Gbps each over a strand of fiber. Without having to deploy new fiber, the effective capacity of existing fiber plant can routinely be increased by a factor of 16 or 32.

The second generation of WDM networks aim to, not only, increase the transmission capacity of the optical fiber but also to increase the flexibility of the optical networks based on WDM introducing functions of the physic, link and net layers in the optical domain. One example would be the application of the IP protocol directly over WDM, instead of being supported by ATM (Asynchronous Transfer Mode) and SDH (Synchronous Digital Hierarchy). Due to the promise of large device markets, very aggressive research is being done on components crucial to WDM, such as optical (de)multiplexers (MUX/DEMUX), optical add-drop multiplexers (OADM), optical cros connects (OXC), and optical wavelength converters (OWC).

### 1.1.2 Technology of the Elements of the Optical Network

A diverse technology is used to implement the highly functional opto-electronic components of the new and more and more complex optical networks. The most widely used material systems in optical network componentry include glass fibers, silica ($SiO_2$) based planar circuits, and indium phosphide (InP) [1].

**Fibers** The glass fibers technology is the most established optical guided-wave technology and should not be regarded anymore as simple passive transmission media. It can implement for various other interesting functionalities such as the production of lasers, amplifiers, polarization controllers, couplers, filters, switches, and attenuators.

**Silica** The silica on silicon (Si) technology is the most widely used planar technology. Waveguides made using this technology present low fiber-coupling loss and low propagation losses. The principal drawback is their too large dimensions due to the low refractive index contrast that results in too large bend radius. In order to avoid this drawback two other new technologies have been developed: silicon on insulator (SOI) and silicon oxinitride ($Si_3N_4$). They present higher refractive index contrast so that the dimensions of the circuit can be reduced. Naturally, the fiber coupling loss increases. Another disadvantage is that it is not possible to integrate fast functions because the external control is usually thermic. Active functionalities, such as amplification and wavelength conversion

have been experimentally proved by doping the Si with Er, similarly to erbium doped fibers.

**InP/InGaAsP** The InGaAsP III–V material system is one of the few semiconductor materials that can be used to produce both active and passive optical devices. It is based on relatively high index contrasts that result in thin waveguides and low bending radius. Nevertheless, such high index differences make the fiber coupling losses increase because of the mode mismatch. The ability to match the lattice constant of InP to that of $In_xGa_{1-x}As_{1-y}P_y$ over the wavelength region of 1.0 to 1.7 $\mu$m makes semiconductor lasers in this material system the preferred optical sources for fiber optic telecommunications. The indium phosphide platform is used to produce lasers, semiconductor optical amplifiers (SOA), detectors, electro-absorption modulators, couplers, filters, and switches.

### 1.1.3 Monolithic versus Hybrid Integration

Planar monolithic integration is the way to integrate as much as possible the different active and passive functionalities of the opto-electronical component on a single substrate or carrier, resulting in small and compact units. It offers a significant reduction in production cost due to the batch processing of wafers. Monolithic integration also leads to space reduction (sometimes by a factor of 10 relative to hybrid construction). Several active-passive integration techniques exist for III–V semiconductors: selective area growth (SAG) [2], Selective etching and regrowth, vertical integration, shadow mask growth (SMG), and quantum well intermixing.

One disadvantage that arises with monolithic integration is that the design of each component in a photonic integrated circuit (PIC) is mostly the result of some compromise in order to achieve the integration and therefore the components might not have the same quality characteristics as the best discrete devices. Monolithic devices also require complex epitaxial growth and processing. Furthermore, monolithic integration does not provide a solution for the fiber alignment and attachment (pigtailing) problem during the packaging although this may account for over 90 % of the component cost.

As an alternative for the monolithic PICs, several companies developed a hybrid integration technology. Hybrid integration tries to combine the best of different material systems ($SiO_2$–InP) in a single opto-electronic device. Therefore, unlike monolithic integration, each part of the component can be optimized separately. Nevertheless, as the cost associated with optical alignment of the different sub-parts due to the increasing amount of sub-components is believed to dominate the cost of the opto-electronic component, low cost assembly techniques are essential.

The method used to reduce assembly costs is the *passive alignment technique* where, as opposed to active techniques, there is no measurement of the coupling efficiency during the alignment. The components are assembled on a carrier and positioned by means of alignment marks or bumps on the carrier and mating

features on the components. Even if this may imply more complex substrate and device processing in order to relax the alignment tolerances, the cost incurred at wafer processing is greatly outweighed by the reduction in the final assembly cost, resulting in a net lowering of the component price.

## 1.2 Increasing the Optical Mode

The typical refractive index difference $\Delta n$ in a III–V semiconductor waveguide is generally larger than 0.1, leading to mode sizes smaller than 2 $\mu$m. Besides, due to the planar technology used in the fabrication of semiconductor waveguides, the mode shape is highly asymmetric. The very small refractive index difference in a single mode glass fiber or silica waveguide ($\Delta n < 5 \times 10^{-3}$) results in a weakly guided circular mode with a typical mode size of 8–10 $\mu$m. Direct butt-coupling between an optoelectronic device and a silica fiber or waveguide causes typically 7–10 dB loss.

The use of an optical element, such as lensed fiber, in order to reduce and adapt the broader mode shape to that of the smallest mode allows a more improved match between modes that increases the coupling efficiency. Nevertheless, as the light spots are very small the alignment tolerances are reduced to values below 1 $\mu$m [3]. Hence, it is a much better solution to enlarge the shape of the smallest mode in order to improve the coupling efficiency and to keep the alignment tolerances high enough for the requirements of the passive alignment techniques. That objective can be achieved by integrating spot-size converters (SSC) in the III–V semiconductor chip.

Figure 1.1 shows the two rationales for the use of SSC's. Figure 1.1(a) schematizes the hybrid integration of a III-V semiconductor opto-electronic component, such as a laser, a SOA, or a PIC with a silica planar lightwave circuit (PLC) on a silicon motherboard. And Figure 1.1(b) shows the pigtailing of a monolithicaly integrated PIC made in III-V semiconductor. There is a third configuration in which the use of SSC's can be really useful to reduce alignment problems and, hence, costs: the hybrid integration of passive and active components in InP [4]. In spite of the fact that the shape of both modes matches, their small dimensions makes the alignment tolerances to be sub-micron.

## 1.3 Present Work

Numerous techniques have been reported in the literature for the realization of efficient mode transformers. However, most of these require cumbersome growth and processing techniques. In this dissertation, the work is focused on developing mode-expanded devices using standard growth and fabrication techniques. We have investigated new structures based on Antiresonant Reflecting Optical Waveguides (ARROW's) for the development of two new concepts for spot-size converters. The first mode expander uses a vertically confined fiber (or silica waveguide)-matched ARROW waveguide. The second spot-size converter applies ARROW confinement for both vertical and lateral directions.

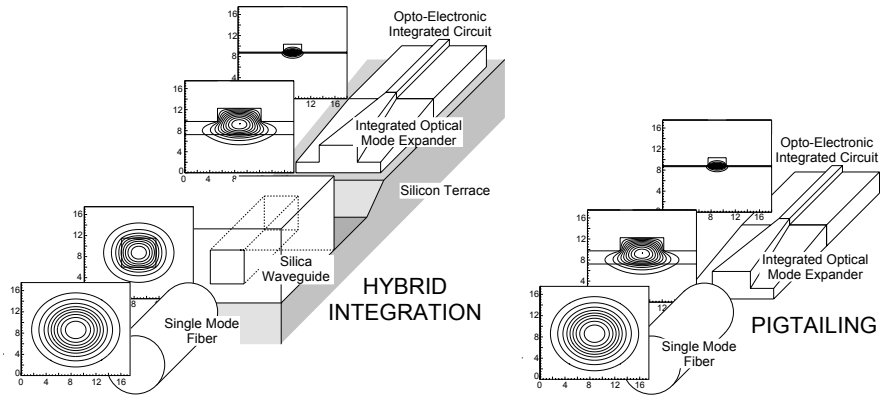


(a) (b)

Figure 1.1: Coupling problem in (a) hybrid integration and (b) fiber pigtailing of opto-electronic devices.

The ARROW concept has also been applied to another key component in the evolution of the integrated opto-electronics: the *waveguide bends*. The radiated leakage of light in a bend can be reduced considerably applying the same ARROW effect used for the confinement of light in the SSC's.

To summarize the contribution of the present work to the field of the SSC's and waveguide bends, we list some of the first time contributions.

1. We have realized a quantum-well semiconductor rib laser using an adiabatic SSC in InP/InGaAsP having an antiresonant reflecting optical waveguide as fiber (or silica)-matched waveguide. The main merit of such a device is that the broad core needed for the broad guide is of InP which is easy to grow. The confinement of the light over the InP substrate is achieved by a set of cladding layers that provide ultra-high reflection for the fundamental mode. The possibility of compact designs of the tapers is also demonstrated.

2. We have demonstrated high performance SSC's integrating them with semiconductor lasers that can be fabricated in the same processes as the standard rib waveguide. The merit of such device is the simplification of, not only the growth of the layer stack, but also the processing to the minimum fabrication steps needed for a standard waveguide: *one growth and one etching step*. This is the simplest SSC concept reported so far.

3. We have demonstrated by simulation the previous SSC concept also in buried heterostructures (BH) which are widely used by commercial companies. Such structures need one regrowth but again, no additional process is needed to integrate the SSC.

4. We have proposed new rib SSC's that use a thin core layer near cutoff instead of a thicker core layer needed in the first two cases. The growing is easier and the applicability of the lateral leaky confinement is relaxed.

5. We report a new concept for the design of low-loss bends. Its application in silica waveguides in which the big radius is the main disadvantage is the objective. High bend-loss reduction is achieved without introducing new fabrication steps.

# Chapter 2
# State of the Art of Integrated Spot-Size Converters

During the past ten years much research has been done on the development of new structures for efficient mode expansion. The reason for such a wide variety of spot-size converters (SSC) is the different fabrication technologies employed in the manufacturing of the integrated optical devices. A good SSC must be compatible with the fabrication process of the component it is integrated with, and this integration should not involve processes that worsen the performance of the device. It turns out that there is no universal SSC. In this chapter we give an overview and a classification of different taper designs in order to place the present work in a proper perspective. An interesting list of the most important groups in the world that work on or make use of SSC's in their commercial optoelectronic products is also presented.

## 2.1 InP–$SiO_2$ Coupling

Figure 1.1 shows the shape and the size of the fundamental mode of a 3 $\mu$m wide standard InP waveguide, a buried silica-on-silicon planar waveguide, and a standard single-mode glass fiber. The coupling efficiency between two waveguides is essentially given by the complex overlap integral of the modes of both waveguides. In the real situation where the two waveguides are not butt-joined, the mode of the transmitting device can be propagated using free space Gaussian beam analysis in order to obtain the mode at the separation distance [5]. The alignment tolerances are a measure of the excess power loss sensitivity as a function of displacement in the transverse, lateral or axial directions. These misalignment tolerances play a critical role in the design of any passive alignment scheme.

### 2.1.1 Alignment Tolerances

To illustrate the nature of the coupling for conventional devices, we use the analysis of [5] to obtain the plot of the coupling efficiency as the waveguide positions is varied in the transverse (vertical $\times$ lateral) directions. Figure 2.1 shows the plots of the coupling efficiency between two standard SMF's (F-F), a standard InP waveguide and a lensed fiber (WG-LF), and a waveguide and a fiber (WG-F). We observe good coupling when the size and the shape of the faced modes matches. However, the broader the spots are, the more relaxed the alignment tolerances are. We can also check in Figure 2.1(a) the low coupling efficiency for a InP waveguide-to-fiber butt coupling. Only a 12.6 % of the

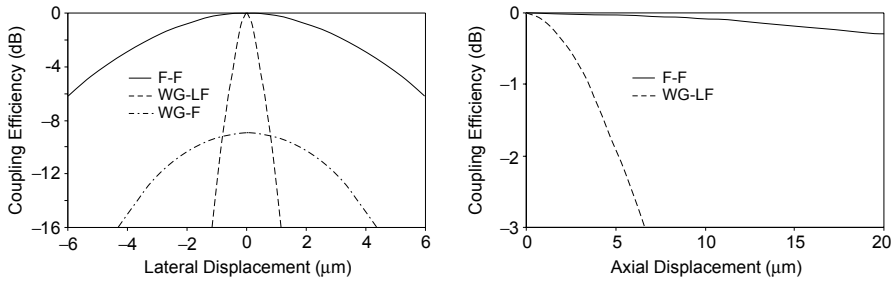


(a) (b)

Figure 2.1: Coupling efficiency scan in (a) the transverse direction $x$ and (b) the axial direction $z$ for standard fiber-to-fiber (F-F) and InP waveguide-to-lensed-fiber (WG-LF) coupling.

optical power is transferred from one guide to the other. Figure 2.1(b) shows the coupling efficiency scan along the axial direction $z$. Again tight tolerances for small sizes and really high tolerances for two fibers butt coupled are obtained.

As we already mentioned in Chapter 1, the conclusion we extract from these results is the need of SSC in the III–V semiconductor chip that expands and transforms the small mode of the waveguides. Then, we will be able to reach the $\pm 1$ $\mu$m tolerance the passive alignment techniques require.

## 2.2 Spot-Size Converters

Over the last twelve years, many approaches have been proposed and demonstrated to transform the mode on chip and improve the coupling to cleaved

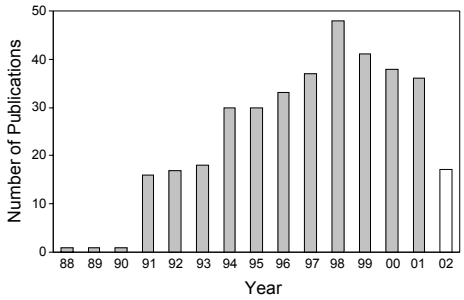


Figure 2.2: Number of publications about integrated optical SSC's published in specialized reviews since 1988 till October 2002.

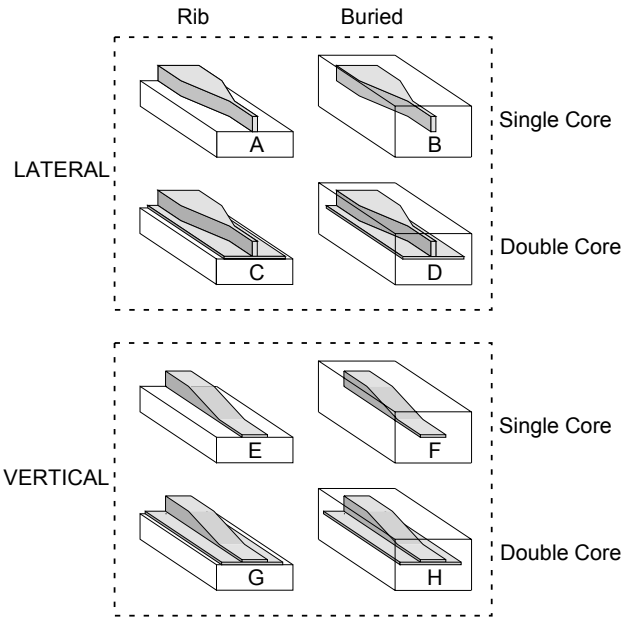


Figure 2.3: Classification diagram of eight main optical-mode transformer structures. (a), (b), (e), (f) correspond to single-core waveguides. (c), (d), (g), (h) correspond to double-core ones.

SMF's and PLC's. From the bibliographic search shown in Figure 2.2 we can see the evolution of the works on SSC's published in the best specialized optical reviews since 1988. We can consider the year 1991 as the beginning year of the research in SSC's. A growing evolution carries on in the following years reaching a maximum of publications in the year 1998. In December of 1997 a special issue of *IEEE Journal of Selected Topics in Quantum Electronics* about SSC's was published. Then, a negative evolution starts in 1999 that carries on till the current year (2002). However, most of the new structures proposed during this period are already commercialized by many companies as we will see in Tables 2.1 and 2.2.

### 2.2.1 SSC Classification

Several classifications of the existing tapers as a function of the modelling method [6]–[8] or from an optical point of view [9] have been published. All spot-size transformers are based on the volume reduction of the waveguide core (active in the case of lasers, SOA's, etc.) along the propagation axis in order to decrease the confinement of the mode and to match in geometry and width a semiconductor mode waveguide to another or that of a SMF or silica waveguide. This decrease may be *vertical* and/or *lateral*. Spot size may hence be broadly classified in

| CLASS | Device | Group | Ref. |
|---|---|---|---|
| 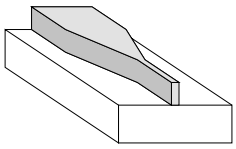 | LD | MIT Lincoln Lab | [10, 11] |
| | LD | Hitachi | [12] |
| | PIC | Bellcore | [13] |
| 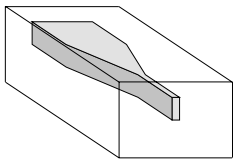 | LD | Alcatel | [14] |
| | LD | Matsushita | [15] |
| | LD | MIT Lincoln Lab | [16] |
| | LD | NEC | [17] |
| | LD | ETRI | [18] |
| | DBR | NTT | [19] |
| | SOA | Alcatel | [20] |
| | SOA | SDL | [21] |
| | PIC | Deutsche Telek. | [22] |
| | PIC | NTT | [23] |
| 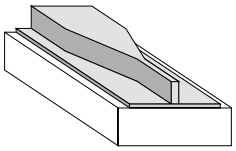 | LD | Alcatel | [24] |
| | LD | IMEC, U Ghent | [25] |
| | LD | U of Maryland | [26] |
| | LD | Sandia NL | [27] |
| | DBR | Princeton U | [28] |
| | PD | Siemens | [29] |
| | PIC | Marconi | [30] |
| | PIC | Bellcore | [13] |
| 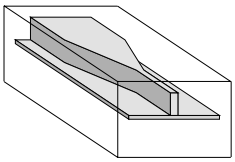 | LD | AT&T | [31] |
| | LD | BTL | [32] |
| | LD | CSELT | [33] |
| | LD | Deutsche Telek. | [34] |
| | LD | Furukawa | [35] |
| | LD | NTT | [36] |
| | DFB | Alcatel | [37] |
| | SOA | Alcatel | [38, 39] |
| | SOA | CNET | [40] |
| | PIC | ANT | [41] |
| | PIC | Deutsche Telek. | [22] |
| | PIC | U Colorado | [42] |
| | Switch | NTT | [43] |

Table 2.1: Overview of laterally tapered optoelectronic devices and the groups and companies that work on them.

| CLASS | Device | Group | Ref. |
|---|---|---|---|
| 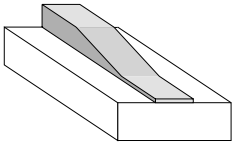 | LD | IMEC, U Ghent | [44] |
| | PIC | Bellcore | [45] |
| | PIC | MIT Lincoln Lab | [46] |
| 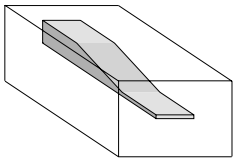 | LD | NTT | [47] |
| | LD | Korea U | [48] |
| | LD | Furukawa | [49] |
| | LD | NEC | [50] |
| | LD | Fujitsu | [51] |
| | LD | Hitachi | [52] |
| | LD | Mitsubishi | [53] |
| | LD | IMEC, U Ghent | [54] |
| | SOA | NTT | [55] |
| | SOA | Samsung | [56] |
| | SOA | Lucent | [57] |
| | PIC | Siemens | [58] |
| 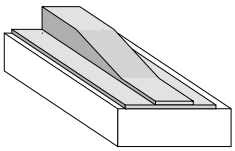 | LD | ETHZ | [59] |
| | LD | IMEC, U Ghent | [60] |
| | PIC | Delft U | [61] |
| | PIC | Heinrich-Hertz I | [62] |
| | PIC | Siemens | [63] |
| | Switch | Siemens | [64] |
| 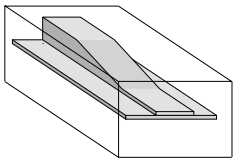 | LD | Hitachi | [65] |
| | LD | Lucent | [66] |
| | LD | NTT | [67] |
| | LD | SDL | [68] |
| | SOA | Lucent | [69] |
| | SOA | NEC | [70] |
| | PIC | CNET | [71] |
| | PIC | Deutsche Telek. | [72] |
| | PIC | ETHZ | [73] |
| | PIC | NTT | [74] |
| | PIC | Siemens | [75] |

Table 2.2: Overview of vertically tapered optoelectronic devices and groups.

two families: *lateral tapers*, where only the width of the tapered waveguide is varied; and *vertical tapers*, the thickness of which is varied , but where the width may also be changed. For both families, the waveguiding structure may be of the *rib* or *buried* type, *single* or *double-core*. Most of the present tapers are schematically represented in Figure 2.3, and consist in eight basic structures. Of course, combinations of taper designs (above all, lateral and vertical ones) have also been reported. Among all the configurations, only several of them have been widely utilized, the choice of a particular taper depending not only in the specific application and optoelectronic component manufacturing process, but also largely on the technological know-how existing in each laboratory.

A list of the most important groups that have worked on SSC's is outlined in Tables 2.1 and 2.2. We have focused the list on research laboratories of companies that have commercialized any kind of SSC integrated with any kind of optoelectronic device. The class of the used SSC and the integrated device are also shown. One or two references are shown corresponding to each group and device.

### Lateral SSC's

In a laterally tapered device the width of the guiding layer(s) is changed. From a fabrication point of view, lateral single core SSC's are the most straightforward because they can be defined in the same growing and lithography processes used for the device they are integrated with, but they are not being used widely.

In Figures 2.3(c) and (d) a narrow and thin waveguide is transferred into a wide and thick waveguide by means of a single lateral overlapping waveguide taper. The waveguide at the end of the taper is a fiber-matched waveguide. A disadvantage of this type of taper, is the need for a sharp termination point of the upper waveguide, which complicates somewhat the taper fabrication process.

### Vertical SSC's

In a vertical taper, the thickness of the guiding layer(s) is changed along the device. Also in this group, the lateral dimensions of the small mode are changed. In contrast to lateral tapers, where standard processing techniques can be used for the definition of the taper, special growth and etching techniques are required to change the thickness along the taper. A wide variety of technologies have therefore been developed to gradually change the thickness of a guiding layer.

Similarly to the single-core lateral tapers, the single-core vertical tapers are not widely used because of the critical thickness variation. In Figures 2.3(g) and (h), the small mode of a waveguide is transformed into a large fiber-matched mode by means of a wedge-shaped vertical taper. Such a configuration is much more useful in practice.

### Special SSC's

There also exist alternative taper designs which cannot be simply classified in lateral or vertical tapers. One of such designs is the multimode interference

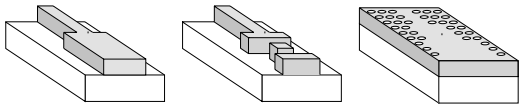


Figure 2.4: Special spot-size converters: (a) multimode interference, (b) segmented, and (c) photonic-crystal.

(MMI) spot-size converter, shown in Figure 2.4(a). Mode transformers of this class excite several modes [76, 77]. The position of the output facet is chosen such that the interference of these multiple modes yields a maximum coupling. This class of SSC's has the advantage of being much shorter than adiabatic spot-size transformers, but they are, however, less flexible and only allow a limited enlargement of the spot size.

The nonperiodic segmented waveguide described in [78, 79] and sketched in Figure 2.4(b) is an example of a interference spot-size converter, since many modes are excited at the consecutive discontinuous transitions. Photonic crystals (PC) have generated a great deal of interest recently because they have the potential to be used to control the propagation of light in very compact devices. SSC's made of photonic crystals (see Figure 2.4(c)) have been demonstrated by NEC Research Laboratories in Japan [80].

For an overview of SSC fabrication methods, we refer to [6].

## 2.3 Qualitative comparison of SSC's

A quantitative comparison of the performance of reported SSC's has been published in several works [6, 8, 61]. However, one must be careful when comparing the data because each taper is demonstrated for one concrete length, and as most of them are based on a *adiabatic* mode evolution (see Section 2.4), the longer the taper design is, the lower the transformation loss is and the higher the coupling efficiency to a fiber can be. Therefore, we will outline some different considerations that have arisen during the realization of the present work and that can be interesting for the reader.

1. It has already been mentioned that the lateral tapers are easier to fabricate because they are compatible with the standard planar growth technology and waveguide processing. Nevertheless, a huge effort and research has been carried out in order to allow vertically tapered layers, so that, at this moment no technological differences are considered between both concepts.

2. Buried waveguides have superior performance characteristics for active de-

vices (lasers or SOA's) compared to rib waveguides. They have better electrical confinement and lower internal losses that result in lower threshold currents and efficiencies. That is the reason why more groups work on SSC's for buried waveguides than for rib waveguides (see Tables 2.1 and 2.2).

3. Moreover, the fact that the core layer is entirely surrounded by the same transparent material, which is not the case for rib waveguides, makes the transformation of the optical mode much more efficient. So, shorter lengths are needed for buried tapers to obtain good coupling efficiencies.

4. The fabrication of single-core SSC's have been found to be more critical than the double-core ones [22]. The reason is that the single-core tapers base their mode expansion in down-tapered weakly guiding fiber-matched waveguides which work point is very critical to the core width.

## 2.4 Adiabaticity

The majority of the SSC's are based on an *adiabatic* mode evolution whereby the small and asymmetric fundamental mode of the waveguide is gradually transformed to a larger and more circular profile. The term *adiabatic* indicates that all power is kept in one mode during propagation. Adiabaticity simply requires a 'slow enough' evolution along the taper. As expected, the longer the taper, the more adiabatic its operation and the less its total loss. However, the taper length cannot be increased indefinitely, so some compromise will have to be found. Therefore, a first step in the analysis consists in bringing out a precise adiabaticity criterion.

The commonly used adiabaticity condition is derived from the physical argument that the local taper length-scale must be much larger than the coupling length between the fundamental mode and the dominant coupling mode for power loss to be small [81]. The local coupling length between the two modes is taken to be the beat length $z_b = z_b(z)$ between the fundamental and second local modes. Hence, the adiabatic criterion has the form:

$$\frac{\mathrm{d}w}{\mathrm{d}z} \ll \frac{w\,(\beta_1 - \beta_2)}{2\pi} \tag{2.1}$$

where $w$ is the width of the waveguide core that is tapered and $\beta_1 = \beta_1(z)$ and $\beta_2 = \beta_2(z)$ are the propagation constants of the fundamental and the second local mode, respectively.

This classical result is derived for a bounded fiber system and cannot be rigourously applied to the open geometry of a integrated waveguide. However, the author in [82] extends this classical theory to obtain the following adiabaticity criterion:

$$\frac{\mathrm{d}w}{\mathrm{d}z} \ll \frac{(\beta_0 - kn_{clad})}{\langle|\partial\hat{\psi}_0/\partial w|^2\rangle^{1/2}} \tag{2.2}$$

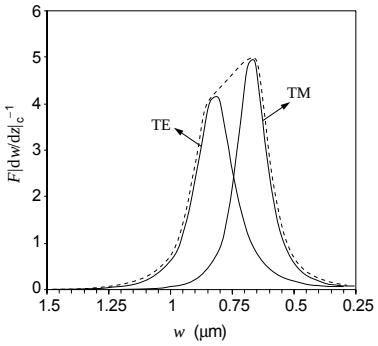


Figure 2.5: Example of the inverse of the critical taper slope for a double-core lateral rib SSC and for TE and TM polarizations. The polarization tolerant shape should follow the dashed line.

The new factor $\langle|\partial\hat{\psi}_0/\partial w|^2\rangle^{1/2}$ that appears in the criterion of Eq. 2.2 and that takes into account the dependence of the mode on changes in the tapered parameter $w$, introduces a more exact design. For example, considering down tapered double-core lateral tapers (Figure 2.3(c) and (d)), we see that narrowing the core width down to a minimum $w_{min}$ the shape of the mode does not change so we can rapidly finish the taper. This fact is not considered by the criterion of Eq. 2.1 which tell us that we must still smoothly taper the end tip of the taper when, in fact, this is not necessary.

Figure 2.5 shows an example where the influence of the polarization in the design of a double-core lateral rib SSC can also be observed. The inverse of the critical taper slope multiplied by the proportionality factor $F$ and calculated from Eq. 2.2 is plotted as a function of the width of the taper. The mode transformation takes place in the range $1.1 - 0.4$ $\mu$m. The TM mode spreads for lower values of the width and in a narrower range. It also requires smoother slopes since its corresponding peak in the graph is higher. Logically, a taper valid for both polarization should follow the dashed line covering both shapes.

## 2.5 Simulation Tools

In this section, we will shortly discuss the simulation tools used for the design of the spot-size converters reported in this thesis. These programs, a mode solver, a mode expansion algorithm and a beam propagation method (BPM), are the most powerful tools for the simulation of photonic devices available today [83].

**Mode Solvers:** Mode solvers are essentially used to find the propagation constant of guided modes in longitudinally invariant waveguides. In the context of this work we used *Fimmwave* [84], a two-dimensional (2D) mode solver based on a transverse resonance method. This method is particularly interesting for

device geometries consisting of rectangular areas with a constant refractive index, like most of the semiconductor structures used for optical waveguiding. The method can be employed for full-vectorial, semi-vectorial or scalar calculations.

The knowledge of the propagation factor is essential to display the spatial optical field distribution, calculate the confinement factor of the field in a specific region, calculate the far-field radiation pattern of a mode, and determine the coupling efficiency between two waveguides.

**Mode Expansion Method:** A first method to simulate the propagation of an optical field through an arbitrary waveguide is the mode expansion algorithm. In this method, the waveguide is approximated by a concatenation of longitudinally invariant waveguide sections. Any field in a cross-section of an optical waveguide is written as a sum of the local modes. The propagation of each mode trough the section is trivial. At the end of a section these modes all couple to the modes of the next section. Also the power reflected back into the modes of the preceding section is taken into account, making the mode matching technique a bidirectional algorithm.

The mode expansion tool that was used in this work is *Fimmprop-3D* [84], a program that is built around the *Fimmwave* mode solver engine.

Even though mode expansion methods are particularly suited for structures that have small number of distinct cross-sections, such as multimode interference couplers (MMI) and periodic structures, *Fimmprop-3D* also effectively deals with continuously varying structures like spot-size converters. It is found that taking into account a limited number of modes (10 modes are sufficient in many cases) already yields accurate results.

**Beam Propagation Method (BPM):** Assuming a wave is propagating in the positive $z$-direction of the optical waveguide structure and assuming the field distribution is known in a plane at $z = z_k$, the task is to determine the field at $z = z_{k+1} = z_k + \Delta z$. Repeating this calculation stepwise from the input to the output, the whole component can be (approximately) analyzed. Most commercially available BPM-packages employ a finite difference-based approach for that purpose.

In the context of this work, we used *BPM_CAD*, a commercial package from *Optiwave Corporation* [85]. It is a finite-difference based package allowing the modelling of both 2D and 3D structures. The specific nature of the SSC's studied in this work, with modes expanding in both lateral and transverse dimension, necessitates the use of the 3D-BPM.

### *Fimmprop-3D* versus *BPM_CAD*

*Fimmprop-3D* is without any doubt the most versatile tool for the design of adiabatic spot-size converters. One of the main reasons why *BPM_CAD3D* is not so suitable is the required simulation time, which easily exceeds 4 hours. Knowing that the design of a spot size converter is mainly an iterative process with sometimes several parameters to be adjusted, it is soon concluded that this

is not a very productive way of working.

The settings of the simulation parameters in *Fimmprop-3D* are also more transparent. The possibility of visualizing the local modes at any position along the device has the advantage of providing physical insight in the device behavior.

Nevertheless, the hard boundary conditions used by *Fimmprop-3D* make the radiated light couple back from the hard walls to the waveguide if the length of the device is long enough. Therefore, for devices having considerable mode transformation loss unexpected results could be obtained. The finite number of modes used by *Fimmprop-3D* is also a limitation to obtain a correct idea of the exact radiated power, and therefore, of the transmitted power. This is also the case of devices having considerable power transfer to higher order or radiative modes. In these las two cases it would be better to use *BPM_CAD*, in spite of its simulation time.

# Chapter 3
# Spot-Size Converters Using Vertical ARROW Waveguides

Expanded mode laser arrays operating in the 1.55 $\mu$m wavelength regime are particularly appealing for WDM system configurations. Nevertheless, achieving mode-matched lasers at 1.55 $\mu$m is more challenging than at shorter wavelengths due to the much larger size of the fiber mode ($\approx 10\mu$m) at this wavelength. The attractive feature of the device presented here is that it uses a single standard epitaxial growth step and conventional processing techniques. The absence of the regrowth of epitaxial layers simplifies the device fabrication significantly. In addition, no direct electron-beam (e-beam) write capability (to realize sharp tapers) or additional process developments are necessary in this approach. Moreover, the method outlined here can be used in other different integrated optical components, as well as with lasers.

In this chapter, we discuss the design and experimental results of 1.55 $\mu$m semiconductor laser arrays with integrated adiabatic mode expanders. These devices have been realized by using an Antiresonant Reflecting Optical Waveguide (ARROW) as fiber-matched waveguide. We first discuss the basics of ARROW waveguides, then the design of the proposed mode-expanded lasers, and finally the experimental procedure and results.

## 3.1 Double-Core Lateral Rib SSC

A schematic diagram of the adiabatic mode expander concept is shown in Figure 3.1. In this device a small rib waveguide is located on top of a thick lower cladding which is partially etched to form a mesa structure. When the width of the upper rib is sufficiently large, the optical mode is supported primarily in the active region and the device picks up optical gain. At the other extreme of the point, when the rib width is small, the fundamental mode expands to fill the underlying waveguide. Therefore, by tapering the active waveguide over a long length, it is possible to transform the mode from the slightly confined active region to the larger coupling waveguide in an adiabatic fashion [86]. The main advantage of this structure is that only one growing step an just two standard processing steps are required. It is also possible to design the gain region and the coupling waveguide separately, and finally consider the optimization of the mode transformation region.

In the InGaAsP–InP material system, InP is the cladding material as well as the substrate. In order to define the thick fiber-matched underlying core it is necessary to grow a material with a refractive index slightly higher to that of the InP. In that way the output mode will be broad enough and there will not be

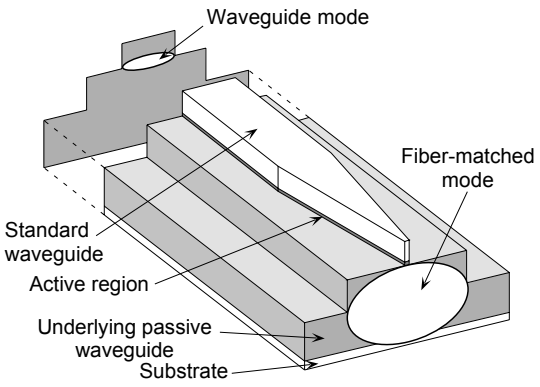


Figure 3.1: Schematic picture of the adiabatic mode expander concept showing the tapered active region and the underlying fiber-matched waveguide.

influence in the optical behavior of the active layer. Such small increase in the refractive index is achieved by means of lattice matched quaternary materials $In_{1-x}Ga_xAs_yP_{1-y}$ having low concentrations of Ga and As, which are rather difficult to achieve during the growing. One simple solution to this technological problem is the growth of alternate layers of InP and higher Ga– and As–fraction quaternary materials that generate an equivalent layer presenting the desired refractive index [87]. In an alternate solution we use an InP layer as the core of a fiber-matched ARROW waveguide. Therefore, there must not take care of the possible influence of the refractive index of this layer on the active mode because it is made with the same material as the substrate. The vertical confinement of the light is achieved by a set of several cladding layers that provide the confinement of light in the InP core. The following section explains in detail such structures.

## 3.2 Antiresonant Reflecting Optical Waveguides (ARROW)

The word ARROW is the acronym of Antiresonant Reflecting Optical Waveguide and makes reference to a waveguide in which the guidance of the light is produced by means of a reflecting antiresonance in at least one direction. This means that there exist a high-index multilayer structure deposited over the substrate so that constructive interference of the reflected ray is produced for a given incidence angle (close to 90°) and wavelength (see Figure 3.2), like in a Bragg reflector optimized for an angle of incidence next to 90° instead of 0° or like in a Fabry–Pérot resonator generated by the interfaces of the multilayer structure. In such conditions, the reflection coefficient of these layers reaches a value close to 100 % for the wavelength that verifies the quarter wave condition, and the light

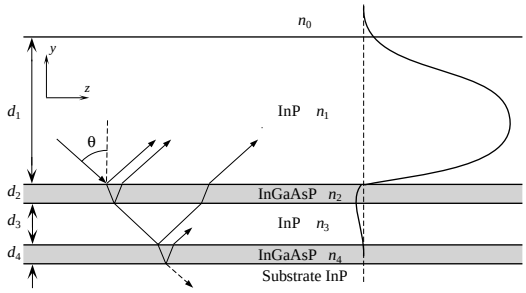


Figure 3.2: Waveguide structure using antiresonant reflection on InP wafer.

can be considered practically *guided*. Consequently, the maximum reflectance conditions and, thus, the *quasi-guided* conditions will be determined just by the multilayer structure considered as planar structure. Under a theoretical modal analysis, this structure supports a certain number of bound modes in the high index layers and several radiation modes with very low losses, which are in fact *leaky modes*.

The typical ARROW structure was first proposed by Duguay *et al.* in 1986 [88]. They implemented the ARROW waveguide in $SiO_2$–Si technology in order to reduce the radiative loss into the high index Si substrate. The light coupled into the core undergoes total internal reflection at the upper surface and very high reflections from the antiresonant claddings. The upper medium is generally air and the ARROW confinement structure usually consists of two layers, the first of them with higher refractive index than the core, and the second with a refractive index similar to that of the core.
Let us suppose a generalized calculation model of ARROW as shown in Figure 3.2 [89, 90]. The phase condition of $\nu$th order mode is expressed by

$$2k_0 n_1 d_1 \sin\theta_\nu + \phi_1 + \phi_2 = 2\pi\nu \tag{3.1}$$

where $\phi_1$ and $\phi_2$ are the phase shifts at the interfaces between upper medium and core and between core and interference first cladding layer, respectively, $\theta_\nu$ is the propagation angle of light, $k_0$ is the wavenumber in vacuum, and $n_1$ and $d_1$ are the refractive index and the thickness of core, respectively. Here we define an equivalent thickness of core $d_{ce}$ involving the penetration of the field into the layers outside the core as follows:

$$d_{ce} = d_1 + \frac{2\pi + \phi_1 + \phi_2}{2k_0 n_1 \sin\theta_\nu} \simeq d_1 + \zeta \frac{\lambda}{2\pi\sqrt{n_1^2 - n_0^2}}, \tag{3.2}$$

$$\zeta = \begin{cases} 1, & \text{for TE modes;} \\ (n_0/n_1)^2 & \text{for TM modes.} \end{cases} \tag{3.3}$$

where $n_0$ is the refractive index of the layer upon the core. In Eq. 3.2 we neglected the penetration of the field into the interference first cladding from

the core because it is very small when the high reflectance condition is satisfied.

We consider now the fundamental mode ($\nu = 0$). The low loss condition of the ARROW waveguide is that the light reflected at individual boundaries of the cladding layers must intensify each other in the direction of the core. This is identical to the condition that the phase shift inside each cladding layer in the direction perpendicular to the surface of the substrate is $\pi/2$. The optimum thicknesses of two layers of the interference cladding, which provide minimum loss, are given by

$$d_2 = \frac{\lambda}{4n_2}\left(1 - \left(\frac{n_1}{n_2}\right)^2 + \left(\frac{\lambda}{2n_2 d_{ce}}\right)^2\right)^{-1/2} \cdot (2M+1) \tag{3.4}$$

$$d_3 = \frac{d_{ce}}{2}(2N+1) \qquad (M, N = 0, 1, 2, \ldots) \tag{3.5}$$

With respect to the fabrication technology of ARROW waveguides, we observe in literature that most works are based on Si substrates, and a small part of them use III–V semiconductors. The first time the InGaAsP–InP system was used for the implementation of an ARROW waveguide was in [91] in 1987. As the InP substrate has the lowest refractive index in this material system, a third high index cladding layer has to be added to the reflector ARROW layers (see Figure 3.2). Due to the higher refractive index of the GaAs substrates, the ARROW structure in this technology is identical to the one for $SiO_2$–Si technology [92].

The ARROW principle has a number of interesting features for many applications. Contrary to conventional guides, light is confined in the region with the lowest index of refraction, thus adding a new optical design freedom. This structure also gives very large loss discrimination against high order modes because, as explained above, the antiresonant layers are optimized for the fundamental mode, and therefore higher order modes do not reach the antiresonance condition having very high leaky losses: around 100 dB/cm for the second order mode and 25 dB/cm for the third order mode [88]. They can be considered *quasi-monomode*.

Another important feature of the ARROW structure is the loss dependence with the wavelength. Changing the wavelength, the antiresonance layers do not behave as quarter-wave layers and the reflected rays do not interfere constructively any more. Then, the leakage towards the substrate and the mode loss increase. Nevertheless, the typical Airy-like function of a Fabry–Pérot resonator has sharp peaks in transmission but a quite flat response over a broad wavelength range in the antiresonant regime that makes the structure considerably tolerant.

We also remark the polarization dependence of ARROW structures. The TE loss is always lower than TM loss since TM reflections are always lower by the same phenomenon which gives rise to the Brewster angle. The degree to which the TM loss is higher depends in detail on the proximity of the propagation angle in the core relative to the Brewster angle. In this way, the factor $\alpha_{TM}/\alpha_{TE}$ is $> 100$ in $SiO_2$–Si ARROW's and around 3 in the InGaAsP–InP material system

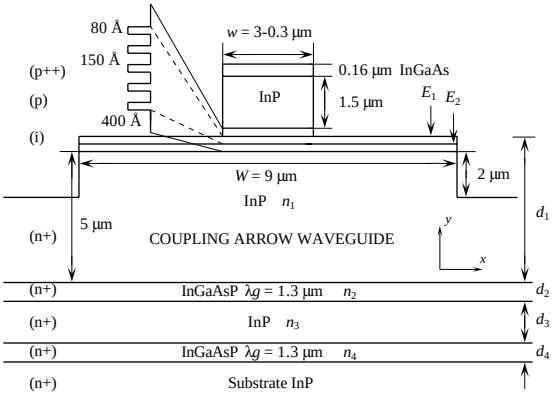


Figure 3.3: Cross section of the mode expanded laser using a passive fiber-matched ARROW waveguide.

because the propagation angle in the former is much closer to the brewster angle of the lower interface of the core layer.

Due to all these characteristics, the ARROW waveguides have been utilized in numerous device applications, such as directional couplers [93], star couplers [94], filters [95], add-drop filters [96], photo-detectors [97], polarizers [98], polarization splitters [99], wavelength de/multiplexers [100], optical interconnects [101], sensors [102] and lasers [103].

## 3.3 Design

A detailed schematic drawing of the proposed mode expanded laser is shown in Figure. 3.3. The active upper rib waveguide and the underlying ARROW waveguide can be observed. The width of 3 $\mu$m of the laser is reduced till a minimum of 0.3 $\mu$m during the tapering. The detailed design process of the active waveguide, the ARROW waveguide and the geometry of the taper are described in detail in the following subsections.

### 3.3.1 Gain Section

An optimized active layer composition of $In_{0.78}Ga_{0.22}As_{0.79}P_{0.21}$ for the wells and $In_{0.75}Ga_{0.25}As_{0.54}P_{0.46}$ for the barriers were designed for maximum optical gain at 1.55 $\mu$m. The 5 active layers are 1 % compressively strained and 80 Å thick, while the barriers are lattice matched and 150 Å thick. The barrier energy gap corresponds to a photon wavelength of 1.25 $\mu$m. The shoulders or separate confinement heterostructures regions are composed of the same material as the barriers and are 400 Å thick. All this layers form the active core of the device and are not electrically doped. The upper cladding consists of 1.5 $\mu$m of $p$-doped InP (see Table 3.1). The lower InP cladding serves as the coupling ARROW

| Description | Composition | Thickness | Doping |
|---|---|---|---|
| Cap layer | InP | 30 nm | $p{+}{+}$ $(2 \cdot 10^{19})$ |
| Contact layer | $In_{0.53}Ga_{0.47}As$ | 160 nm | $p{+}{+}$ $(2 \cdot 10^{19})$ |
| Up-cladding | InP | 1350 nm | $p{+}$ $(5 \cdot 10^{17})$ |
| Up-cladding | InP | 150 nm | $p{+}$ $(2 \cdot 10^{17})$ |
| SCH region | $In_{0.75}Ga_{0.25}As_{0.54}P_{0.46}$ | 400 Å | $i$ |
| QW ($\times$ 5) | $In_{0.78}Ga_{0.22}As_{0.79}P_{0.21}$ | 80 Å | $i$ |
| Barrier ($\times$ 4) | $In_{0.75}Ga_{0.25}As_{0.54}P_{0.46}$ | 150 Å | $i$ |
| SCH region | $In_{0.75}Ga_{0.25}As_{0.54}P_{0.46}$ | 400 Å | $i$ |
| ARROW core | InP | 5000 nm | $n{+}$ $(1 \cdot 10^{18})$ |
| ARROW cladding 1 | $In_{0.71}Ga_{0.29}As_{0.61}P_{0.39}$ | 320 nm | $n{+}$ $(1 \cdot 10^{18})$ |
| ARROW cladding 2 | InP | 2600 nm | $n{+}$ $(1 \cdot 10^{18})$ |
| ARROW cladding 3 | $In_{0.71}Ga_{0.29}As_{0.61}P_{0.39}$ | 320 nm | $n{+}$ $(1 \cdot 10^{18})$ |
| Substrate | InP | – | $n$ |

Table 3.1: Epitaxial layer structure of the mode expander using a underlying fiber-matched ARROW waveguide.

waveguide and its optimization is discussed in the next section.

Two different devices, with a different etch depth for the laser rib, have been calculated and fabricated. The two etch-stop points are indicated as $E_1$, $E_2$ in Figure 3.3. The shallow etching $E_1$ stops just above the layer containing the first quantum well, while the deep etch $E_2$ goes through the QW's. It is expected that the former option will provide a better performance of the laser because it presents lower surface recombination. On the other hand, when the mode is expanded in the taper, it will be slightly confined in unpumped active quaternary layers. This fact will introduce some absorption losses in the shallowly etched devices that are not present in the deeply etched ones.

### 3.3.2 Coupling ARROW Waveguide

By increasing the thickness and the width of the underlying ARROW waveguide, the mode size of the laser output can be increased leading to smaller coupling loss with a fiber. However, a larger underlying waveguide results in an increased mode transformation loss as the centroid of the mode shifts by a larger distance and the spreading of the light field is larger. Therefore, a compromise has to be found between the coupling loss and the length of the SSC.

In our case, a technological limitation must be taken into account: the maximum growth thickness for our MOVPE reactors is around 11 $\mu$m. And taking into account the InP core and the three ARROW cladding layers needed for the confinement this limit requires a core $d_1$ of 5 $\mu$m, which is a good compromise value considering the length and the coupling loss. For the high index ARROW cladding layers $d_2$, $d_4$ we choose a lattice matched quaternary material with a bandgap wavelength $\lambda_g = 1.3$ $\mu$m in order to use non-absorbing materials. The

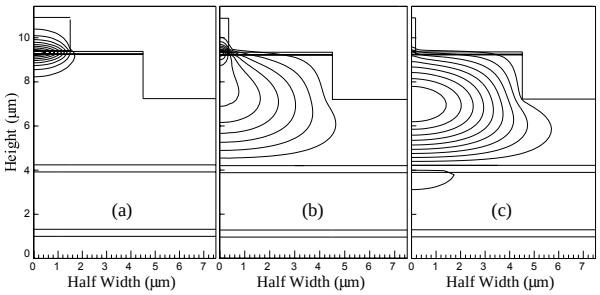


Figure 3.4: The fundamental TE mode evolution for (a) $w = 3$ $\mu$m, (b) $w = 0.9$ $\mu$m, and (c) $w = 0.5$ $\mu$m.

exact composition of this Q(1.3) material is $In_{0.71}Ga_{0.29}As_{0.61}P_{0.39}$ and its refractive index is 3.39. Taking into account these considerations, Eq. 3.4 and Eq. 3.5 provide $d_{2(4)} = 0.32$ $\mu$m and $d_3 = 2.6$ $\mu$m for the optimum ARROW cladding design.

The width and etch depth of the ARROW rib mode have been designed as a compromise between the fiber coupling efficiency and the mode transformation rate of the SSC. A width of 9 $\mu$m and a etch depth of 2 $\mu$m have been chosen for the fiber-matched waveguide (see Figure 3.3).

A $n$-type electrical doping was provided for the ARROW core and cladding layers. The fiber-matched mode will propagate in such a doped material, but the $n$-type doping does not induce considerable propagation losses to the mode. Table 3.1 shows the layer structure of the device used to demonstrate adiabatic mode expansion.
Therefore, all the loss mechanisms involved in the SSC are: the mode transformation loss inherent to the SSC, the leakage in the ARROW confinement layers, the absorption in the unpumped QW's (above all for the shallow etching option), and the absorption due to the doping in the InP ARROW core. Only the first one is high enough to take into account in the design.

### 3.3.3 Taper Geometry

Figure 3.4 shows the evolution of the fundamental mode of the mode expander for three different active rib widths and for the shallowly etched device. We observe that when the small rib is sufficiently wide (3 $\mu$m) the fundamental mode is tightly confined in the small rib (see Figure 3.4(a)) and the device functions as an efficient laser with a high confinement of light within the active layer. On the other hand, when the small rib is sufficiently narrow, the fundamental mode expands to fill the larger ARROW waveguide (see Figure 3.4(c)).

The critical taper slope provided by the adiabaticity criterion represented by Eq. 2.2 in Chapter 2 has been numerically calculated using *Fimmprop-3D* for the two designs considered in this work and depending on the etching depth. Figure 3.5 shows the inverse of the critical slope as a function of the width of

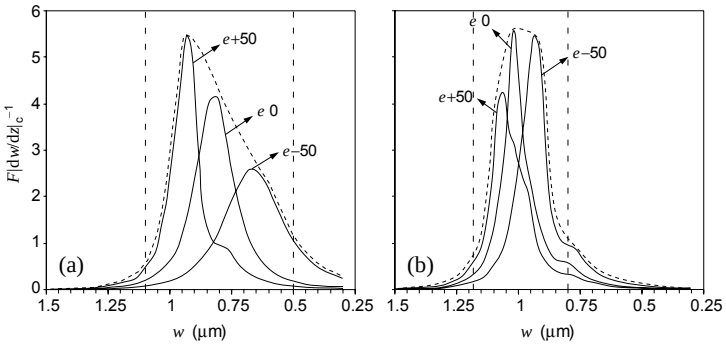


Figure 3.5: Inverse of the critical taper slope for the (a) shallowly and (b) deeply etched tapered lasers.

the upper active rib multiplied by the proportionality factor $F$. We observe that the mode transformation takes place for values of the width lower than 1.25 $\mu$m and that for narrow widths, when the mode is already expanded in the ARROW waveguide, no smooth slopes are needed either. A technological limit of 0.3 $\mu$m for the final taper tip has been considered.

The critic slope of possible variations of $\pm 50$ nm in the etch depths that can be produced during the fabrication are also shown for both cases. The three designs are called $e-50$, $e$ 0 and $e+50$. The tapering also depends on the refractive index difference $\Delta n$ between the effective index of the active core and the InP of the core of the ARROW waveguide. Variations of $\pm 2$ % in $\Delta n$ have been considered but their influence in the critic slope is low compared with the variations induced by the etch tolerance. This is why only the designs corresponding to etch depth variations are shown. A tolerant design should follow the slope provided by the envelop function covering all the three designs. However, we have approximated the optimum adiabatic shape by a piecewise linear device consisting of three linear sections (see Figure 3.6). The dashed vertical lines of Figure 3.5 indicate the selected values $w_2$ and $w_3$ in a tolerant design that takes into account possible influences of variations of the etch depth during the processing. Table 3.2 shows the values of the designed parameters.

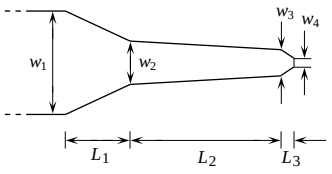


Figure 3.6: The optimum taper shape is approximated by a piecewise linear device consisting of three linear sections.

| | $w_1$ | $w_2$ | $w_3$ | $w_4$ | $L_1$ | $L_2$ | $L_3$ |
|---|---|---|---|---|---|---|---|
| $E_1$ | 3 | 1.1 | 0.5 | 0.3 | 100 | 350, 450, 540 | 20 |
| $E_2$ | 3 | 1.18 | 0.8 | 0.5 | 100 | 250, 300, 342 | 20 |

Table 3.2: Widths and lengths of the designed piecewise adiabatic tapers. All the values are in $\mu$m. $E_1$ and $E_2$ correspond to the shallow and deep etch options, respectively.

For the choice of the length of the critical central section $L_2$ we have simulated the transformation efficiency, that is, the power carried by the fundamental mode along the taper, as a function of $L_2$. Figure 3.7 shows these results for the exact structures and for structures with variations of $\pm 50$ nm in the etching depth and variations of $\pm 2$ % in the refractive index difference $\Delta n$. We have selected three different lengths for the mask design that are indicated by means of the dashed thin lines in the graphs and which are shown in Table 3.2. A misalignment of $\pm 1$ $\mu$m in the definition of the ARROW rib reduces the efficiency by less than 0.2 dB. So this is a problem that should not be taking into account.

The designed mask contains two big groups containing the designs corresponding to both etching depths and a third group with untapered reference lasers. In the design of the tapered structures a taper is placed at each end of a 2100 $\mu$m straight laser. The laser is chosen that long so that two cleaves are possible. The laser is 3 $\mu$m wide and is followed by the taper ending by a 50 $\mu$m long straight waveguide to have an easy cleaving.

Each group consists of 5 subgroups with 5 identical structures each. These subgroups are meant to cope with the fabrication tolerances to the definition of the required widths (we observed after the fabrication that a systematic narrowing of around 0.3 $\mu$m is produced during the processing of the ribs). Therefore, we implemented the structures as designed and structures with variations of $-0.1$, 0.15, 0.3, and 0.45 $\mu$m in their widths.

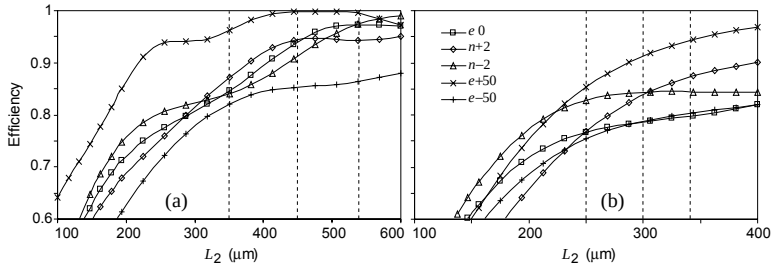


Figure 3.7: Mode transformation efficiency of the piecewise taper as a function of the length of the central section $L_2$. (a) Shallowly etched devices, and (b) deeply etched devices.

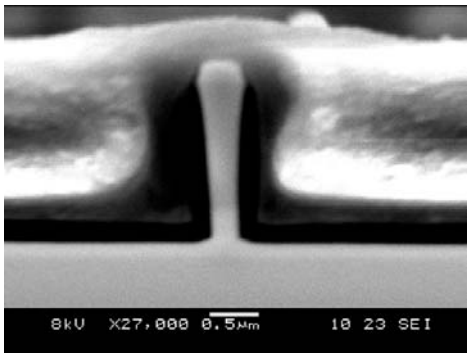


Figure 3.8: SEM picture after the ridge etch, showing the sharp taper tip obtained.

## 3.4 Fabrication

The epitaxial layers were grown by metal organic chemical vapor deposition (MOCVD). By plasma etching we defined the $SiO_x$ pattern with conventional photoresist as a mask. The tapered active rib was etched by RIE to a depth 100 nm above the active layer. Next, a selective wet etch of the remaining InP was carried out. This etch was done using H3PO4:HCl (7:3). Finally, an extra 40 nm (shallow etch) or 140 nm (deep etch) RIE etch into the active layer was performed. This process involves an underetching of the rib so that the mask has to be defined around 0.3 $\mu$m wider than the desired width. Scanning electron microscope (SEM) pictures of the taper ends revealed that taper dimensions of 0.3 $\mu$m were obtained reproducibly (see Figure 3.8). Subsequently, a 9 $\mu$m wide and 2 $\mu$m high mesa was dry etched to provide lateral index guiding for the expanded mode. Thereafter, polyimide was spin-coated on the sample to form an insulation layer. The thickness of the polyimide is less on top of the ridges compared to the rest of the sample. Therefore, by an adequate window opening and a controlled plasma etch, the dielectric was removed on the ridge while dielectric coverage remained elsewhere resulting in good electric isolation. This process eliminates the necessity of critically aligning dielectric window-opening mask exactly on top of a 2.5 $\mu$m ridge and allows the contacting of the thin ridges of the lateral taper.

Next, using a negative photoresist and a metal liftoff process, the metallization pattern was defined. Finally, the thinning of the substrate was done and the back contact was deposited. Arrays of devices, each with 520 $\mu$m long straight active sections, were mounted on electrically cooled copper heatsinks with silver epoxy and were tested without any coatings. The entire device is electrically pumped because the metallization also covers the entire length of the spot size converters. This can have a negative impact on the threshold current and efficiency, but on the other hand it avoids the risk of high absorption losses in the passive section of the taper. Untapered lasers 750 $\mu$m long and 3 $\mu$m wide and

| Laser | $I_{th}$ (mA) | $\eta_d$ (W/A) | $L$ ($\mu$m) | $T_0$ ($^\circ$K) | $FC$ (dB) | $FF$ (Deg.) | Tol. ($\mu$m) |
|---|---|---|---|---|---|---|---|
| Ref., $E_1$ | 31 | 0.09 | 750 | 65 | $-8.2$ | 30.5 × 43 | $\pm 1.9 \times \pm 2.1$ |
| Ref., $E_2$ | 30 | 0.13 | 750 | 81 | $-8$ | 30.1 × 40.1 | $\pm 1.5 \times \pm 2$ |
| Tap., $E_1$ | 45 | 0.1 | 990 | 71 | $-2.9$ | 10.4 × 22 | $\pm 2 \times \pm 2.2$ |
| Tap., $E_2$ | 50 | 0.15 | 890 | 65 | $-2.6$ | 10 × 27 | $\pm 2.2 \times \pm 2.3$ |

Table 3.3: Measurement results on the integrated mode expanded lasers using ARROW waveguides. Devices having two different etch depths (shallow $E_1$ and deep $E_2$) have been processed. $I_{th}$ = threshold current; $\eta_d$ = external efficiency; $L$ = total laser length; $T_0$ = characteristic temperature; $FC$ = fiber-coupling efficiency; $FF$ = far-field divergence angles; $Tol.$ = 1-dB alignment tolerance.

fabricated from the same wafer as the tapered lasers were also prepared as a reference. Both reference and tapered lasers have similar total active area.

## 3.5 Experimental Results

All the measured parameters are shown in Table 3.3. The devices were operated in continuous wave (CW) operation. The deeply etched reference devices, with a threshold current of 30 mA and an external efficiency of 0.13 W/A, present a slightly better laser performance than the shallowly etched ones, which have a similar threshold current but a lower external efficiency (0.09 W/A). Regarding the mode-expanded lasers, an increase of about 20 mA in the threshold current with respect to the reference lasers is found. This is a common behavior due to the mode transformation loss within the taper, to the losses in the $n$-doped thick InP ARROW core layer and to the increased length, and not to the introduction of the ARROW. The measured full width at half-maximum (FWHM) values are also shown in Table 3.3. An important lateral divergence improvement is achieved for both groups of lasers, reaching a minimum of 10° for the deeply etched lasers. This value should be compared with the 30° divergence of the reference devices. The achieved vertical field divergences are higher (22° and 27° for both sets of lasers respectively, see Table 3.3), but are still substantially lower than the 40° of the reference devices. A coupling efficiency measurement was performed between the expanded mode laser and a standard cleaved single mode fiber with a spot size of 10 $\mu$m at 1.55 $\mu$m. Fiber coupling efficiencies better than $-3$ dB are obtained for both etch depths, including the Fresnel losses occurring at the air-glass interface. And finally, A maximum $-1$ dB alignment tolerance of $\pm 2.2 \times \pm 2.3$ $\mu$m (lat. × vert.) is obtained for the deeply etched devices.

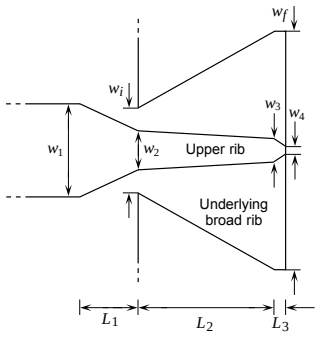


Figure 3.9: A relaxed adiabatic mode transformation can be achieved by tapering simultaneously the upper and the underlying fiber-matched ribs.

## 3.6 Double Tapering

The mode expander proposed in this section tapers laterally, not only the active upper rib, but also the underlying broad rib, which is progressively widened towards the output facet. Figure 3.9 shows the shape of the proposed taper. There is no change in the shape of the active taper (Table 3.2), and the underlying rib is linearly tapered from a initial width $w_i = 2$ $\mu$m to a final width $w_f = 9$ $\mu$m. The broad tapering is defined in the critical central section $L_2$ because it is there where the mode transformation takes place.

The concept is based on the fact that the propagation constant of the mode in the underlying fiber-matched rib waveguide decreases with its width. Therefore, the propagation constant difference increases leading to higher tapering angles and shorter taper lengths (see Section 2.4).

Both shallowly and deeply etched lasers have been simulated using *Fimmprop-3D*. Figure 3.10 shows the resulting efficiency as a function of the length of the

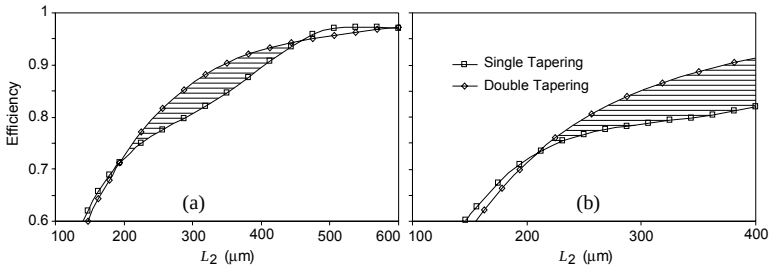


Figure 3.10: Mode transformation efficiency of the original and double taper as a function of the central section $L_2$. (a) Shallowly etched devices, and (b) deeply etched devices.

critical second section $L_2$. The efficiency corresponding to the previous mode expander is also shown for comparison (from Figure 3.7). No longer lengths have been simulated because of the fabrication limitation on the minimum tapering slope of 100 nm/90 $\mu$m. The improvement achieved by the new concept has been shaded in the figure. We observe that the taper length required to reach an efficiency of 90 % is around a 20 % shorter using the double tapering.

## PUBLICATIONS: [A], [B], [C]

Preliminary simulation results on SSC's using ARROW waveguides are presented in [A] (Sections A.2 and A.3). In [B] the first experimental results are published. The final and more complete set of experimental results are presented in [C] (Section C.2).

# Chapter 4
# New ARROW Structures for Mode-Expanded Lasers

In the previous chapter, we have demonstrated the potential of ARROW waveguides for fiber-coupling functions in InP technology. The main objective was to simplify the fabrication process of mode-expanded lasers, above all, the inconvenient growing of thick quaternary materials. Using ARROW waveguides, the thick fiber-matched core consists of InP, which is always less problematic to grow. In this chapter, we keep the objective and go further in the simplification of the only growth step by reducing the thickness of the overall layer stack without altering the good performance showed by the first devices.

## 4.1 Introduction

The optimum three ARROW cladding layers are designed to generate an antiresonance condition and provide minimum leakage loss towards the substrate. They are calculated by means of analytical expressions calculated using the ray tracing method and Snell's law [88]. The total thickness of this optimum cladding is always higher than half the InP ARROW core thickness, which can be considered rather thick. Since the expanded ARROW-confined output mode is only guided over a short distance within the taper, it is not really necessary to reduce the ARROW losses to an absolute minimum. In other words, it is allowed to move away from the antiresonance condition, thus increasing the radiation but also reducing the thickness of the cladding layers, and consequently simplifying the growth.

During the last three decades, numerous efforts have been made to solve the wave equation for the propagating modes in a general, lossless or lossy multilayer waveguide, in such a way as to facilitate the design and optimization of ARROW waveguides [104]–[109]. Nevertheless, the thin-film transfer-matrix method (TMM) [110] has established itself as one of the primary tools for multilayer waveguide analysis. The thin-film TMM can easily form the dispersion equation of a multilayer waveguide consisting of any combination of lossless and lossy (dielectric, semiconductor, metallic) layers. The guided-mode propagation constants of the structure correspond to the zeros of this equation. From this information the electric and magnetic fields can be found for any interior or exterior point. Many zero-search numerical algorithms have been developed to solve the dispersion equation [107, 111]. Since we focus on the fundamental mode of an ARROW waveguide (higher order modes are out of practical interest in our adiabatic taper application), a useful initial approximation close to the exact zero can easily be predicted, and therefore, a simple scan around it is enough to

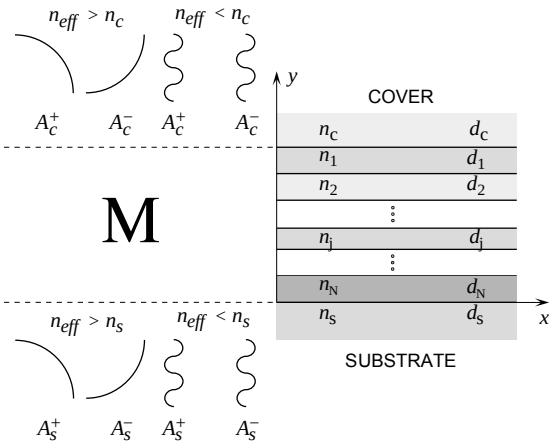


Figure 4.1: Functional form of the exponential functions corresponding to each field coefficient in the two outer mediums of a multilayer structure consisting of $N$ planar films between infinite cover and substrate media.

find the point. In the following section, we describe the TMM in detail and use it to calculate the radiated leaky losses of the ARROW waveguide used in the structure of the SSC. Then, a thinner ARROW cladding structure is designed, much more attractive from a growth point of view, and a complete tolerance analysis is carried out. And finally, the fabrication and performance of the new devices are shown and discussed.

## 4.2 Transfer-Matrix Method

The matrix formalism is an extremely useful form of the steady-state solution to Maxwell's equations subject to the boundary conditions imposed by a multilayer stack, as the one schematized in Figure 4.1. The detailed analysis is developed in [112] where the field coefficients in the substrate $s$ and the cover $c$ are related by

$$\begin{bmatrix} A_s^+ \\ A_s^- \end{bmatrix} = M \cdot \begin{bmatrix} A_c^+ \\ A_c^- \end{bmatrix} = \begin{bmatrix} m_{11} & m_{12} \\ m_{21} & m_{22} \end{bmatrix} \cdot \begin{bmatrix} A_c^+ \\ A_c^- \end{bmatrix} \tag{4.1}$$

being $M$ the *transfer matrix* of the multilayer structure.

### 4.2.1 Modal Solutions in a Multilayer Structure

The functional forms of the exponential functions corresponding to each field coefficient $A_j^+$ and $A_j^-$ are schematically shown in Figure 4.1. The periodic, increasing and decreasing nature are emphasized as a function of the effective index of the propagating mode. We now investigate the shape of the fields supported by the structure.

**Guided modes** The *guided modes* are confined in the $y$ direction and propagate the energy in the $z$ direction. Theses modes decline when $y$ tends to $\pm\infty$, which means that the field coefficients $A_c^+$ and $A_s^-$ have to be zero. The propagation matrix equation is

$$\begin{bmatrix} A_s^+ \\ 0 \end{bmatrix} = M \cdot \begin{bmatrix} 0 \\ A_c^- \end{bmatrix} \tag{4.2}$$

In order to accomplish Eq. 4.2, the element $m_{22}$ of matrix $M$ must be 0. This equality determines de propagation constant of the guided modes and the field coefficients. There only exist a finite number of discrete values of real effective indexes that fulfill the condition $m_{22} = 0$, and that can be considered guided modes. If the multilayer structure does not have absorbing layers, the effective index of the guided modes satisfies the condition:

$$n_{core} > N_{eff} > \max(n_s, n_c) \tag{4.3}$$

where $n_{core}$ makes reference to the higher refractive index in the structure that corresponds to the guiding layer or core.

**Radiation modes** There is a continuous group of radiation modes, having also real effective propagation indexes. Two subgroups can be distinguished here. When the effective index of the mode solution is lower than the substrate and higher than the cover layer ($n_c < n_{eff} < n_s$), and when the effective index is just lower than the cover index ($n_{eff} < n_c$). The former represent radiation modes in the substrate where they exhibit a periodic behavior from $y_N$ till infinity. The field coefficients in the outward mediums are then related by

$$\begin{bmatrix} A_s^+ \\ 0 \end{bmatrix} = M \cdot \begin{bmatrix} A_c^+ \\ A_c^- \end{bmatrix} \tag{4.4}$$

forming a continuous set of infinite solutions as we already mentioned.

On the other hand, if $0 < n_{eff} < n_c$ we obtain general continuous radiation modes that oscillate along all the axis $y$ tending to $\pm\infty$. The field coefficients are related in this case by the general equation

$$\begin{bmatrix} A_s^+ \\ A_s^- \end{bmatrix} = M \cdot \begin{bmatrix} A_c^+ \\ A_c^- \end{bmatrix} \tag{4.5}$$

There exist two independent coefficients that determine two linearly independent solutions for each refractive index value. Consequently, the radiation modes are obtained as a combination of such solutions, and verifying the orthogonality condition.

The radiation modes described so far can be considered as *propagating* radiation modes, since they all have a component $e^{ikn_{eff}z}$ that implies propagation in the $z$ direction. Nevertheless, there is another group of radiation modes called *evanescent*, that do not transport any energy in the propagation direction $z$. These radiation modes have an imaginary effective propagation index, which is the cause of the attenuation or evanescence of light when propagating along the $z$ axis.

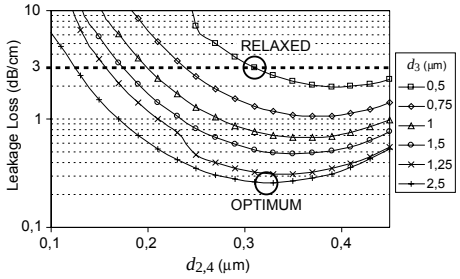


Figure 4.2: Attenuation or leakage losses of the fundamental TE ARROW mode as a function of the thickness of the three cladding layers $d_2$, $d_3$, and $d_4$ for a core thickness $d_1 = 5$ $\mu$m.

**Leaky modes** There is another set of discrete solutions to the Maxwell equations that do not have physical existence but that are very interesting from an optical point of view. They provide information about the leakage loss of a guiding structure. These *leaky modes* are usually associated with solutions of the structure just below cutoff, and that propagate light next to the core but without being totally confined. They have significant meaning in the analysis of transient situations, but are rather difficult to treat. The propagation constant of each leaky mode is complex:

$$\beta = \beta^r + i\beta^i = k_0 n_{eff} + i\frac{\alpha}{2} \tag{4.6}$$

The imaginary part determines the attenuation or leaky losses of the mode, and losses are given by the commonly used attenuation coefficient $4.343\alpha$ (decibels per unit length).

The leaky modes solution of the multilayer structure can radiate in the substrate, in the cover layer, or in both. In the first case the field coefficients of the general solution in the substrate layer $A_s^+$ and $A_s^-$ must be 0. Therefore, the complex propagation constants can be calculated from $m_{12} = 0$. When the leaky modes radiates in the cover layer, the coefficients $A_c^+$ and $A_c^-$ must be 0. In this case, the equation to solve is $m_{21} = 0$. If the leakage is produced in both mediums, then we should solve $m_{11} = 0$ because $A_c^-$ and $A_s^+$ have to be null.

In our particular case, the ARROW waveguide supports leaky modes in the substrate, because of the antiresonant cladding structure over the substrate used to confine the mode. Therefore, equation $m_{12}$ has to be solved to determine the exact complex propagation constant of the *quasi-guided* fundamental ARROW mode.

## 4.3 New ARROW Structures

Using the TMM, we have calculated the leakage losses of the 5-$\mu$m-thick ARROW waveguide used in Chapter 3 as a function of the thicknesses of the three

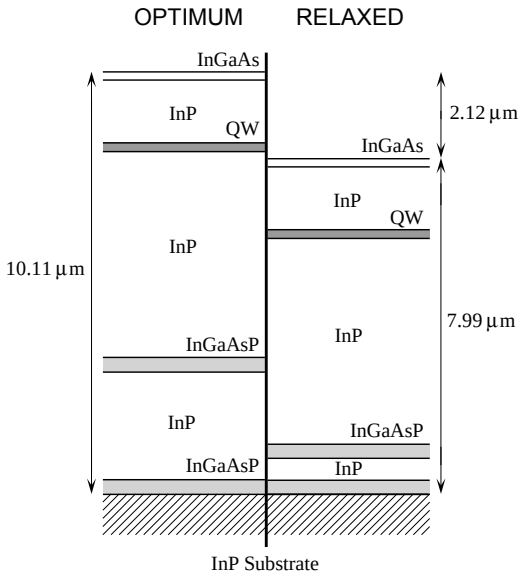


Figure 4.3: Schematic drawing to scale of the optimum and proposed new relaxed layer structures for the mode-expanded lasers.

cladding layers $d_2 = d_4$, and $d_3$. Results are shown in Figure 4.2. The leakage loss for the optimum design calculated with Eq. 3.4 and 3.5 is 0.25 dB/cm, which causes negligible loss compared with the mode transformation of the taper. If a maximum propagation length of 300 $\mu$m is considered for the ARROW mode in the taper and a reasonable total leakage loss of 0.1 dB is allowed, the new cladding layers may exhibit a leakage loss as high as 3 dB/cm. The line that keeps this reasonable criterion is highlighted by the thick dashed line in Figure 4.2. The relaxed structure with a leakage loss of 3 dB/cm is $d_{2,4} = 0.31$ $\mu$m and $d_3 = 0.5$ $\mu$m, reducing the total cladding thickness to 1.12 $\mu$m, which is 2.12 $\mu$m less than the optimum structure. Figure 4.3 shows a schematic drawing to scale of the optimum and relaxed layer stacks, in order to better appreciate the overall thickness reduction.

So far, we have not considered the influence of the lateral confinement provided by a rib structure on the guiding conditions in the ARROW. The authors in [113, 114] demonstrated a negative impact of the rib definition on the leakage loss but that was anyway negligible for wide enough waveguides, which is our case. Therefore, power leakage properties of the rib-ARROW waveguide are essentially determined by the planar ARROW structure, investigated in detail in this section. In order to check this feature for the relaxed structure, a BPM semi-vectorial propagation of a 9 $\mu$m wide ARROW waveguide with the new relaxed cladding layers has been carried out. The guide is excited with a Gaussian field and for a propagation distance of 500 $\mu$m the power is stable and only

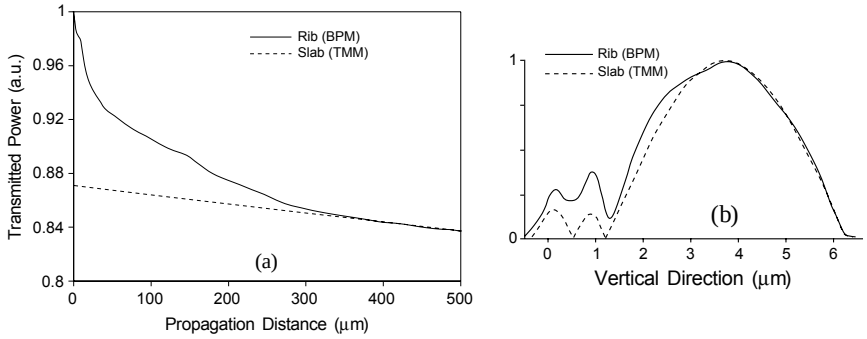


Figure 4.4: (a) Transmitted relative power when coupling a Gaussian field to a 9 $\mu$m wide rib ARROW waveguide plotted together with the a decreasing exponential corresponding to the theoretical loss calculated by TMM for TE polarization, and (b) electric field distribution of the fundamental TE ARROW mode calculated using TMM and from a vertical cut in the simulated rib ARROW waveguide.

the leakage of the leaky fundamental ARROW mode goes out of the simulation window. Figure 4.4(a) shows the relative transmitted power along the straight waveguide. A exponential function corresponding to the calculated leaky loss (3 dB/cm) is also plotted for comparison. We observe that, after power stabilization, the leaky loss of the rib waveguide exactly fits the loss corresponding to the slab structure. In Figure 4.4(b), the field distribution of the fundamental ARROW mode in the new relaxed slab waveguide and in a central vertical cut in the end of the propagated waveguide are shown. Some more light remains in the confinement cladding layers for the rib waveguide can be observed.

### 4.3.1 Tolerance analysis

As we have moved away from the optimum antiresonance condition, it is mandatory to check if the new structure keeps the robustness the standard ARROW's shows and if it is tolerant enough to parameter variations during the fabrication process or to alterations in the operation point $\lambda$. The dependence on variations of the cladding layer thickness produced during the growing can be checked from the previously-shown Figure 4.2. Taking into account the high accuracy of planar growth technology (a few nanometers), this is a parameter that is not critical at all.

In Figure 4.5(a), the variation of the leakage losses of the fundamental ARROW mode as a function of deviations in the refractive index of the high index cladding layers $n_{2,4}$ is shown. A variation of $\pm 2$ % has been considered. Figure 4.5(b) shows what happens when the wavelength changes around 1.55 $\mu$m. We conclude that there is not critical parameter to take into account during the design or the fabrication if the 3 dB/cm loss criterion is used.

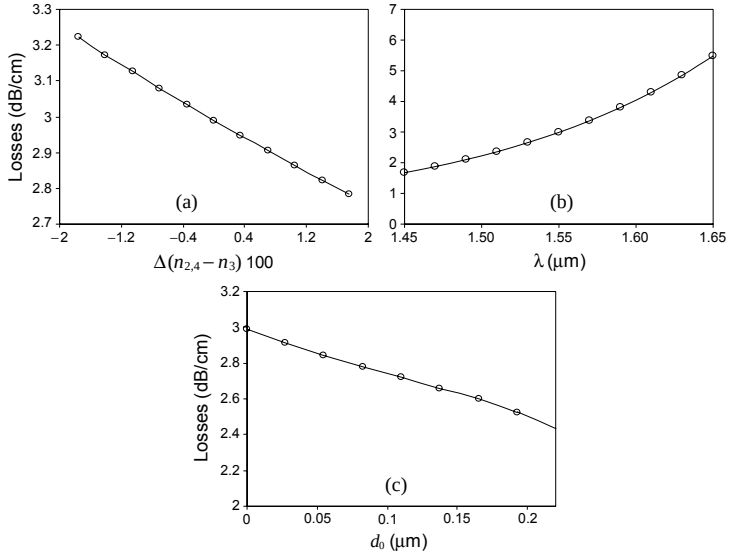


Figure 4.5: Tolerance analysis of the relaxed ARROW structures for vertical confinement of tapers as a function of (a) the refractive index difference between the substrate and the high index cladding layers, (b) the working wavelength, and (c) the thickness of the non-etched upper active core.

Since the ARROW waveguides considered in this work are designed as a component of a taper (see Figure 3.3), a smaller rib waveguide is built on top of it. The layer comprising the core of this smaller guide may generate a new layer to be considered in the design of the broad ARROW output waveguide if it is not totally etched. From [115], we know that this additional layer will not have negative influence on the leakage losses, but positive, because the loss reduces for thicker ARROW cores. The reason are the fewer reflections the fundamental mode experiences over the cladding layers for thicker cores. We have anyway investigated the influence of an additional layer on top of the relaxed ARROW core. The results are shown in Figure 4.5(c). An equivalent refractive index of 3.4242 and a thickness range of 0–0.22 $\mu$m have been considered. Layers thicker than this maximum are not in cutoff and induce guided modes that would degrade the shape of the output fiber-matched ARROW mode. As expected, the upper core induces a decrease of the leakage loss.

## 4.4 Fabrication and Experimental Results

Identical fabrication process as the one outlined in Section 3.4 was used to implement lasers integrated with SSC's using the new relaxed ARROW structures. The measured parameters are summarized in Table 4.1. The deeply etched untapered lasers present the best performance. They show a threshold current

| Laser | $I_{th}$ (mA) | $\eta_d$ (W/A) | $L$ ($\mu$m) | $T_0$ ($^\circ$K) | $FC$ (dB) | $FF$ (Deg.) | Tol. ($\mu$m) |
|---|---|---|---|---|---|---|---|
| Ref., $E_1$ | 35 | 0.13 | 750 | 78 | $-8$ | 30.3 $\times$ 39 | $\pm 1.8 \times \pm 2.1$ |
| Ref., $E_2$ | 22 | 0.13 | 750 | 68 | $-8.2$ | 30.9 $\times$ 40.7 | $\pm 2 \times \pm 2.3$ |
| Tap., $E_1$ | 60 | 0.11 | 990 | 70 | $-2.7$ | 11 $\times$ 19 | $\pm 2.3 \times \pm 2.4$ |
| Tap., $E_2$ | 32 | 0.1 | 890 | 79 | $-2.9$ | 9.6 $\times$ 25 | $\pm 2.4 \times \pm 2.5$ |

Table 4.1: Measurement results on the integrated mode expanded lasers using the relaxed ARROW configuration. Devices having two different etch depths (shallow $E_1$ and deep $E_2$) have been processed.

around 22 mA, while the shallowly etched lasers exhibit a threshold of 35 mA. Regarding the mode-expanded lasers, an increase of only 10 mA in the threshold current with respect to the reference is found for the deeply etched devices. In the case of the shallowly etched devices this increase in the threshold is of 25 mA. Some regular kinks are observed in the deeply etched $E_2$ tapered lasers due to some multimode behavior.

The coupling efficiency to a standard single mode fiber does not change and also the lateral FWHM divergence angles remain the same compared to the SSC's using the optimum ARROW structure. The vertical divergence angles, however, are reduced by a few degrees. The reason of this slight improvement is the reduction of the light in the new relaxed $d_2$, $d_3$ and $d_4$ cladding layers. The sign of the optical field in these layers (see Figure 3.4(c)) is opposed to the sign of the field in the InP core and reduces the fiber coupling efficiency and the far-field divergence angles. A maximum $-1$ dB alignment tolerance of around $\pm 2.4 \times \pm 2.5$ $\mu$m (lat. $\times$ vert.) is obtained for both sets of devices.

## PUBLICATIONS: [A], [C]

Preliminary simulation results about lasers integrated with SSC's using relaxed vertical ARROW structures are presented in [A] (Section A.3.1). The experimental results are published in [C] (Section C.3).

# Chapter 5
# Spot-Size Converters Using Lateral ARROW Waveguides

In this chapter we propose and demonstrate a new concept for SSC's that makes use of antiresonance effects not only for the confinement of the fiber-matched mode in the vertical direction, as it has been demonstrated in previous chapters, but also for the lateral confinement. The main advantage of this new structure is that it does not require either extra growth or extra processing to fabricate the taper, i.e., the SSC can be integrated just using the same fabrication steps employed to define the device. This is the simplest double-core SSC demonstrated so far. Only the single-core lateral SSC's has a fabrication scheme as simple as the one required for this taper, but as we already mentioned in Chapter 2 it is not so efficient and requires longer designs that are less tolerant to fabrication deviations.

The idea comes from the application of the ARROW effect to the lateral confinement of the fiber-matched waveguide. Nevertheless, there appear guided modes in the confinement structures that make its analysis considerable different to the standard ARROW theory. In the first part of this chapter the theoretical background to understand the guiding effect used in the concept is explained. Next, the design, fabrication and measurement results of lasers integrated with SSC's are discussed, demonstrating the good behavior of the presented concept. In the final section of the chapter two interesting variants are analyzed by simulation, which are expected to show better performance.

## 5.1 Two-Dimensional Coupled-Mode Theory

The theoretical analysis developed in this section has been used for the construction and analysis of *index-antiguided arrays* that have been applied in the fabrication of high power and diffraction limited phased-locked buried lasers [116]. An array of leaky modes is used in these structures to provide mode stability to high-output power, as well as strong discrimination against higher order lateral modes [117, 118]. In [103, 119] not an array but just an anti-guide is used to stabilize the high-power laser. We use similar structures in the design of the SSC proposed in this work.

Consider the two one-dimensional waveguides defined in terms of their effective-index profiles in Figure 5.1. These guides will in general support single-guide modes $\psi_1(x)$ and $\psi_2(x)$ characterized by propagation constants $\beta_1$ and $\beta_2$ and coupling coefficient $k$. If the coupling coefficient $k$ is weak, the modes of the coupled waveguides are the in-phase (anti-phase) combination of $\psi_1$ and $\psi_2$ in Figure 5.1(b) (Figure 5.1(c)) whose propagation constant $\beta$ will be above

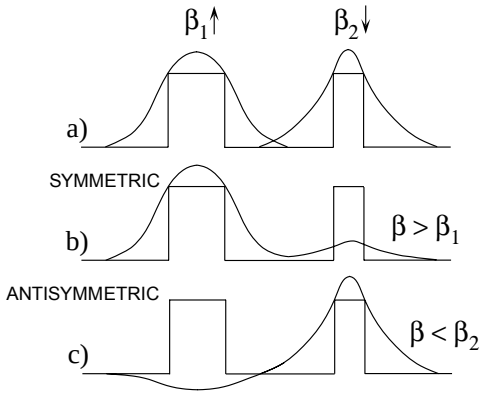


Figure 5.1: (a) Effective-index profiles for two coupled one dimensional waveguides whose lowest-order modes (amplitudes shown) have different propagation constants. Also shown are (b) the in-phase and (c) the anti-phase combinations that form the modes of the coupled system.

(below) the larger (smaller) of the values $\beta_1$ and $\beta_2$ and whose power will be concentrated primarily under the guide whose mode has the largest (smallest) propagation constant. In the case $\beta_1 = \beta_2$, the power is approximately equally divided between each guide for both the in-phase and anti-phase superpositions. In the more general case, where each guide can support a number of modes, the coupled modes may be more complicated linear combinations of these guide modes [120].

Let's consider next a more real but still simplified structure formed by two independent couples of buried waveguides and an infinite slab waveguide as shown in Figure 5.2(a) and (b), respectively. This idealized geometry represents a good approximation of device structures for the new SSC using lateral ARROW's. The individual fundamental modes of the two couples of buried waveguides and the slab waveguide are shown. We do not consider the second order antisymmetric mode of the buried couples of waveguides in this study because it is not relevant. We now form the modes of the overall device as linear combinations of the individual waveguide modes in a manner that is exactly analogous to the one-dimensional case discussed above. The resulting three supermodes are shown in Figure 5.2(c). The power of the two in-phase modes is concentrated on the buried waveguides and they do not present significant changes compared to the individual modes, just a small spreading of the field in the slab core. The field of the anti-phase mode, however, is concentrated in the waveguide with the lowest propagation constant, which is the slab waveguide. We can observe that the mode is confined totally in the lateral direction. A small and negative power distribution can be observed in the buried waveguides but it is small compared to the remaining field in the slab waveguide, therefore the mode is suitable for fiber or silica-waveguide coupling purposes.

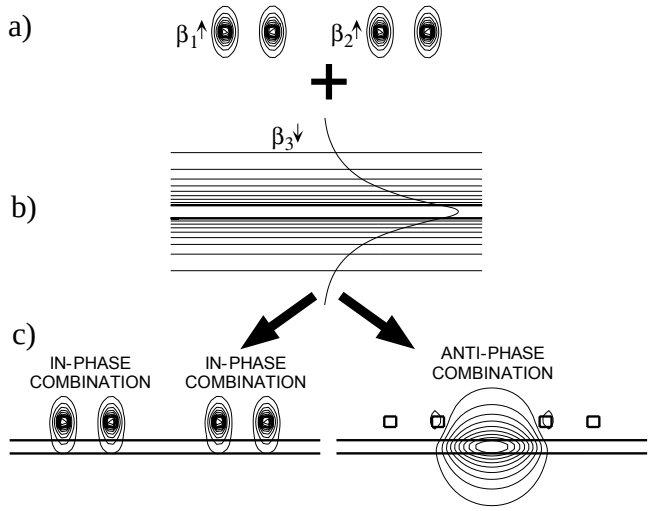


Figure 5.2: Field contours of the fundamental modes of (a) two coupled buried waveguides, (b)a slab waveguide, and (c) the two in-phase and one anti-phase coupled modes of the structure that results placing the three sets of waveguides close enough.

## 5.2 Design

A detailed schematic drawing of the proposed mode-expanded laser is shown in Figure 5.3. The active structure is identical to the one used in previous chap-

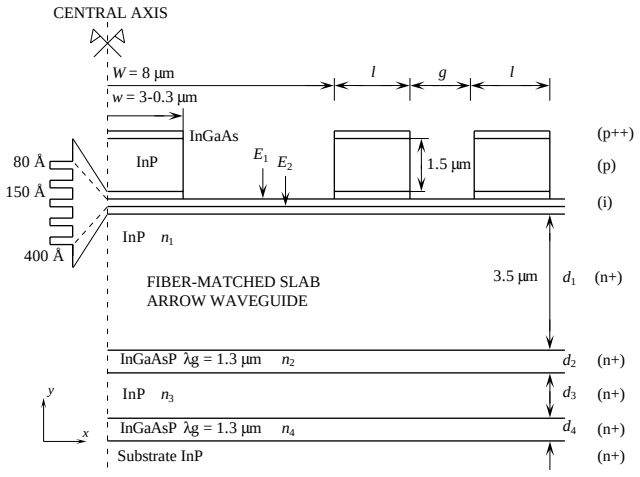


Figure 5.3: Schematic drawing of the adiabatic mode-expanded laser showing the tapered upper active rib, the underlying fiber-matched ARROW slab waveguide and the lateral confinement rib waveguides.

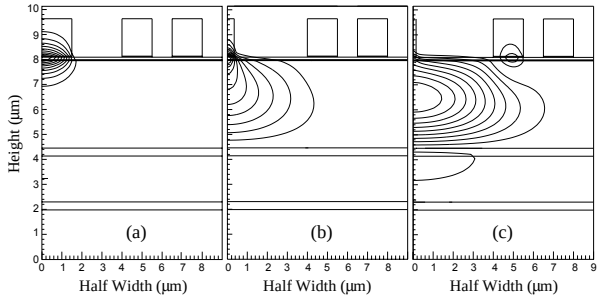


Figure 5.4: Fundamental TE mode evolution along the taper structure of Figure 5.3 for (a) $w = 3$ $\mu$m, (b) $w = 0.9$ $\mu$m and (c) $w = 0.3$ $\mu$m. A shallow etch is simulated.

ters, including the two etching depths $E_1$ and $E_2$ (see Table 3.1). The lower InP core thickness is 3.5 $\mu$m because the lateral ribs lose their influence on the optical confinement when thicker layers are used. From Eq. 3.4–3.3 and using the same materials (quaternary compound with $\lambda_g = 1.3$ $\mu$m) for the ARROW cladding layers, we find $d_{2(4)} = 0.32$ $\mu$m and $d_3 = 1.86$ $\mu$m. The mode expansion is produced in an identical way as it was explained in Section 3.1. The lateral tapering of the central rib spreads light from the active layers into the passive fiber-matched ARROW waveguide, as it is shown in Figure 5.4.

The lateral ribs are defined in the same processing step as the central one, therefore, their etching depth is fixed and only their width $l$ and the gap $g$ between them have to be designed (see Figure 5.3). From the theoretical analysis of Section 5.1 we know that the higher the propagation constant of the fundamental mode of the lateral ribs, the higher the confinement of the anti-phase mode in the lower ARROW waveguide. This can be accomplished widening the lateral width of the lateral ribs, provoking an increase in the propagation constant of the mode of the lateral ribs . Nevertheless, the guidance of higher order modes that combine with the slab underlying mode introduces a limitation to this widening. Figure 5.5 shows the confinement of the output leaky mode in the QW's of the lateral ribs for shallow etching as a function of the lateral rib widths $l$ while keeping the gap $g$ constant and equal to 1 $\mu$m. This confinement should be minimized in order to keep the distribution of the field in the passive broad mode and reduce absorption in the unpumped lateral ribs. The typical periodic response is obtained. The confinement of waveguides having variations in the refractive index contrast ($\Delta n = \pm 2$ %) and etching depth ($\Delta e = \pm 50$ nm) are also shown in Figure 5.5. The minimum does not shift, demonstrating the strength of the concept. The optimum widths $l$ for both etching depths are found to be 1.5 $\mu$m (shallow etch) and 1.6 $\mu$m (deep etch).

Concerning the taper geometry, Figure 5.6 shows the inverse of the critical slope of both structures depending on the etching depth. They are similar to the slopes calculated in Figure 3.5 for the SSC using only the vertical ARROW,

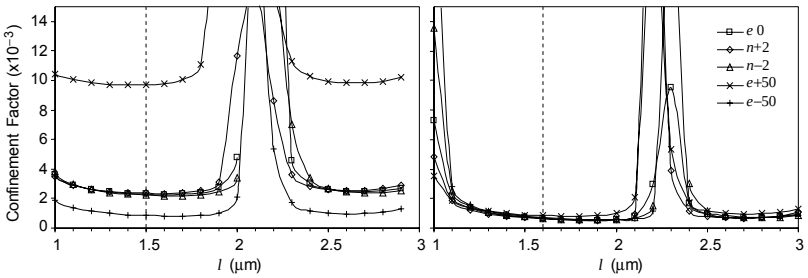


Figure 5.5: Confinement of the output mode in the QW's of the active layer as a function of the widths of the lateral ribs $l$ and variations of the etching depth and refractive index difference for tolerance analysis. (a) Shallowly etched devices, and (b) deeply etched devices. The dashed line shows the selected widths for the lateral ridges.

but the peaks are somewhat lower and the width of the graphs spreads slightly. Therefore, lower slopes can be used but due to this wider range, the needed lengths are bigger. Another interesting remark is that the variations in the etching depth produce a bigger shift (and even a spreading) of the critical range for the shallow etch option of Figure 5.6(a) when compared to the critic slope corresponding to the deep etch option of Figure 5.6(b). Naturally, this fact implies the need of longer tapers for the former. Once again we have approximated the optimum adiabatic shape by a piecewise linear device consisting of three linear sections (see Figure 3.6).

For the design of $L_2$ we have simulated the efficiency of the taper as a function of it, and three different lengths have been chosen for the definition of the

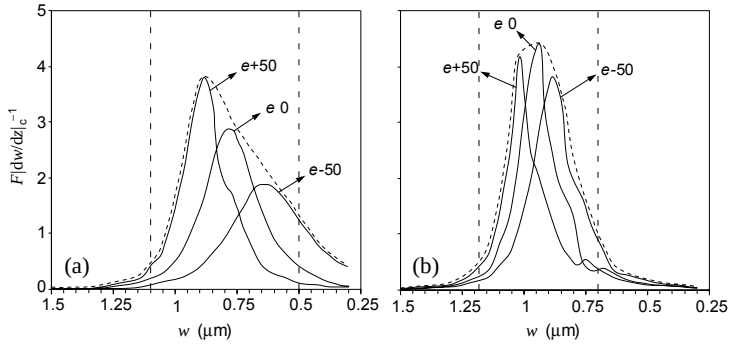


Figure 5.6: Inverse of the critical taper slope for the (a) shallowly and (b) deeply etched tapered lasers. Critical slopes are shown for structures presenting variations of $\pm 50$ nm in the etching depth in order to design a tolerant taper.

| | $w_1$ | $w_2$ | $w_3$ | $w_4$ | $L_1$ | $L_2$ | $L_3$ |
|---|---|---|---|---|---|---|---|
| $E_1$ | 3 | 1.1 | 0.5 | 0.3 | 100 | 200, 300, 400 | 20 |
| $E_2$ | 3 | 1.18 | 0.7 | 0.4 | 100 | 300, 370, 432 | 20 |

Table 5.1: Widths and lengths of the designed piecewise adiabatic tapers. All the values are in $\mu$m. $E_1$ and $E_2$ correspond to the shallow and deep etch options, respectively.

mask. Table 5.1 shows all the designed parameters.

## 5.3 Fabrication and Experimental Results

A wafer with the new layer structure was grown by MOCVD and the devices were implemented using the same processing steps as detailed in Section 3.4 (except, of course, the dry etching of the broad rib). Once again, arrays of devices, each with 520 $\mu$m long straight active sections, were mounted on electrically cooled copper heatsinks with silver epoxy and were tested without any coatings. Untapered lasers (750 $\mu$m $\times$ 3 $\mu$m) fabricated from the same wafer as the tapered lasers, were also prepared as a reference.

All the measured parameters are shown in Table 5.2. The deeply etched reference devices, with a threshold current of 28 mA, present a better laser performance than the shallowly etched ones (35 mA). Regarding the mode-expanded lasers, an increase of about 20 mA in the threshold current with respect to the reference lasers is found. The higher absorption loss in the unpumped QW's of the lateral ARROW rib waveguides for the shallowly etched devices (see Figure 5.4(c)) causes a decrease of the external efficiency of the laser from 0.12 W/A to 0.1 W/A. This fact is not observed in the deeply etched devices that maintain the same external efficiency as the reference lasers.

The measured full width at half-maximum (FWHM) values are also shown in Table 5.2. A considerable improvement is achieved in the lateral direction for both groups of lasers, reaching a minimum of 13° for the deeply etched lasers.

| Laser | $I_{th}$ (mA) | $\eta_d$ (W/A) | $L$ ($\mu$m) | $T_0$ (°K) | $FC$ (dB) | $FF$ (Deg.) | Tol. ($\mu$m) |
|---|---|---|---|---|---|---|---|
| Ref., $E_1$ | 35 | 0.12 | 750 | 88 | $-8$ | 31.5 $\times$ 42.8 | $\pm$1.6 $\times$ $\pm$2 |
| Ref., $E_2$ | 28 | 0.12 | 750 | 65 | $-8.3$ | 30.7 $\times$ 40.6 | $\pm$1.5 $\times$ $\pm$2 |
| Tap., $E_1$ | 55 | 0.1 | 1040 | 42 | $-4$ | 13.8 $\times$ 30.8 | $\pm$2.3 $\times$ $\pm$2.4 |
| Tap., $E_2$ | 48 | 0.12 | 1010 | 61 | $-4.3$ | 13 $\times$ 32.7 | $\pm$2.2 $\times$ $\pm$2.3 |

Table 5.2: Measurement results on the integrated mode expanded lasers using lateral ARROW's. Devices having two different etch depths (shallow $E_1$ and deep $E_2$) have been processed.

On the other hand, due to the thinner ARROW slab core (3.5 $\mu$m), the achieved vertical field divergence is still slightly higher than 30°, improving it by 10° with respect to the reference laser. A further improvement in the vertical far-field pattern could be obtained by thickening the ARROW core layer and defining more than two ribs on each side of the output ARROW waveguide in order to provide a good lateral confinement for thick cores.

Maximum fiber coupling efficiencies of around $-4$ dB are obtained for both etching depths, including the Fresnel losses occurring at the air-glass interface. The improvement in the fiber coupling with respect to the untapered devices amounts up to 4 dB. A maximum $-1$ dB alignment tolerance of around $\pm 2.3 \times \pm 2.4$ $\mu$m is obtained for both sets of lasers.

## 5.4 New Vertical ARROW Structures

Following an analogous treatment to the described in Chapter 4 a new relaxed vertical ARROW cladding structure has been designed for the SSC based on the lateral ARROW waveguide, and analyzed by simulation. In order to obtain a larger thickness reduction, a new quaternary compound with $\lambda_g = 1.45$ $\mu$m and a refractive index of 3.46 has been used instead of the quaternary having a refractive index of 3.39. A new structure with $d_{2,4} = 0.22$ $\mu$m and $d_3 = 1$ $\mu$m, provides a vertical ARROW cladding of only 1.44 $\mu$m instead of the 2.5 $\mu$m of the minimum loss configuration. Moreover, the performance of the taper (see Table 5.2) is not only maintained, but slightly improved. We refer to [A], Section A.4.1 for details on the simulation results.

## 5.5 5-$\mu$m Thick Fiber-Matched Core

In the previous section, we have mentioned that the increase of the thickness of the fiber-matched slab InP core would improve the vertical far-field distribution, and that then it would be necessary the use of more than two ribs on each side of the output ARROW waveguide in order to provide a better lateral confinement. Once this concept has been demonstrated in the first part of this chapter, and taking into account that we defined 5 rib waveguides on each side of the laterally tapered laser, we have used the mask with the designs corresponding to the tapers based on the 3.5-$\mu$m thick ARROW'S, and we have processed lasers on the wafer having the 5-$\mu$m thick core. Figure 5.7(a) shows the distribution of the fundamental mode in the slab core of 5 $\mu$m and confined by five shallowly etched rib waveguides defined on top of it. The field spreads several micrometers in the slab core but it is still suited for fiber coupling. Theoretical calculations predict a coupling efficiency to a cleaved single mode fiber of 52 % ($-2.8$ dB). Nevertheless, the shape of the active rib taper is optimized for a fiber-matched waveguide of only 3.5 $\mu$m and the mode transformation efficiency when considering such a thick core decreases till 70 % for the largest length in the mask. Anyway, these values are still good for a laser and therefore, the performance of the integrated SSC can be measured.

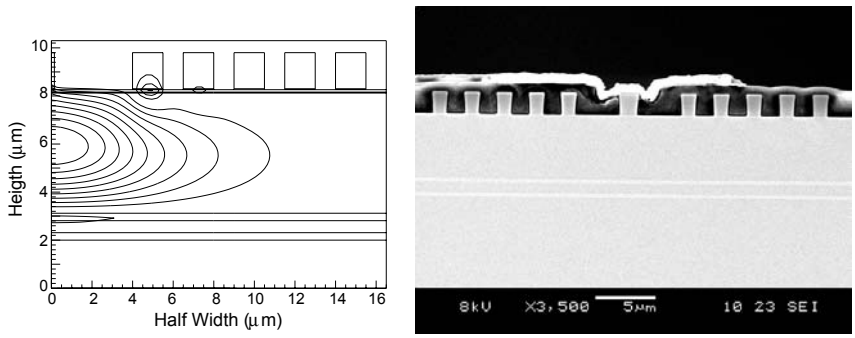


(a) (b)

Figure 5.7: (a) Field distribution of the fundamental mode of a SSC using five confinement lateral ARROW ribs on each side of the active waveguide and for a fiber-matched core of 5 $\mu$m. (b) SEM photograph of the fabricated device.

The SEM photograph in Figure 5.7(b) shows the laser cross section. As it can be seen, the wafer with the relaxed vertical ARROW cladding layers have been utilized. A perfect definition of the ten lateral ribs and a perfect metal contact have been achieved. Nevertheless, in spite of the nice processing the performance of the batch of lasers has not been good. Only a few lasers emitted more than 4 mW power and even less presented well shaped output field distributions. Tapered lasers showed threshold currents of around 60 mA, while the reference control samples showed threshold currents around 35 mA. A more considerable difference is observed if we compare the external efficiencies: 0.1 W/A for the reference lasers and only 0.075 W/A for the expanded lasers. A saturation power lower than 5 mW is also measured. This bad performance can be attributed to the high radiation power loss in the non-optimized beam transformation region.

The measured FWHM divergence angles are $7.8° \times 24.6°$ for the expanded-mode device, compared to $31.5° \times 42.8°$ for the reference lasers. Nevertheless, despite of these promising far-field divergence angles, the measured coupling efficiency to a cleaved single mode fiber only reached $-4.4$ dB, compared to the $-2.8$ dB of the theoretical prediction. This fact can be attributed again to the low efficient mode transformation that excites radiation modes that alter the shape of the fundamental leaky fiber-matched mode of Figure 5.7(a).

As conclusion of this short section we remark that we have not demonstrated the good performance of the SSC using lateral ARROW's as thick as 5 $\mu$m but the measured far-field and alignment tolerance ($\pm 2.5 \times \pm 2.8$ $\mu$m) results show a promising behavior if the optimum shape of the tapering is designed.

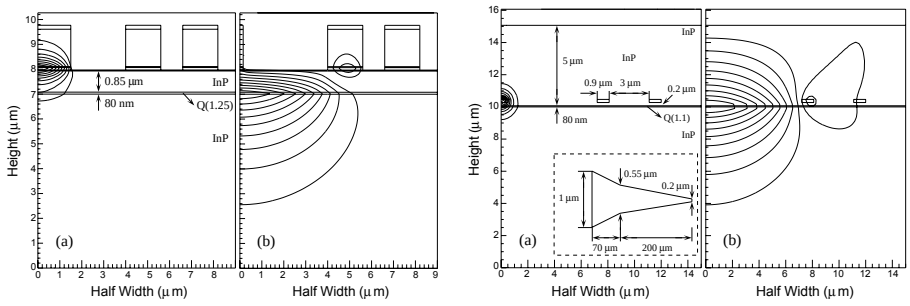


(a) (b)

Figure 5.8: (a) Schematic structure of the SSC using a weakly guiding underlying slab waveguide. (b) Schematic structure of a buried variant of the proposed SSC concept. Higher and more efficient mode transformation efficiencies can be achieved in buried structures.

## 5.6 Variants

### 5.6.1 Weakly Guiding Fiber-Adapted Waveguide

The waveguide structure of Figure 5.3 has a limitation on the vertical direction because the lateral ribs lose their confinement effect when the slab core becomes too thick ($> 5$ $\mu$m). The structure of Figure 5.8(a) makes use of a thin weakly-guiding core of only 80 nm and buried in InP beneath the active layer. The fact that the maximum of the modal field distribution (also shown in the figure) is closer to the upper lateral couple of ribs strengthens their influence. Simulation results on the propagation of this new structure are shown in Table 5.3. We observe that the beam divergence angles and the coupling efficiency are improved to $7.2° \times 14°$ and $-2.4$ dB, respectively.

### 5.6.2 Buried Laser

The mode transformation concept proposed in the present work can also be integrated in a second variant, being a buried laser structure as shown in Fig-

| | $FC$ (dB) | $FF$ (Deg.) | Tol. ($\mu$m) |
|---|---|---|---|
| Figure 5.8(a) | $-2.4$ | $7.2 \times 14$ | $\pm 2.3 \times \pm 1.9$ |
| Figure 5.8(b) | $-1.1$ | $7.2 \times 9$ | $\pm 2.9 \times \pm 2.3$ |

Table 5.3: Simulation results on the variants of Figures 5.8(a) and 5.8(b).

ure 5.8(b). The fact that the tapered active central core is totally embedded in InP makes the mode transformation efficiency much higher for buried than for rib structures. This is the reason why the length of the buried SSC (270 $\mu$m) is much shorter than the rib SSC (490 $\mu$m).

Simulation results on the SSC propagation are shown in Table 5.3. They show fiber butt coupling losses as low as 1.1 dB, beam divergence angles of $7.2^\circ \times 9^\circ$, and alignment tolerances of $\pm 2.9 \times \pm 2.3$ $\mu$m, compared to the 8.5 dB coupling loss and $29^\circ \times 32^\circ$ divergence angles of the untapered devices.

## PUBLICATIONS: [A], [C], [D], [E]

Preliminary simulation results on SSC's based on lateral ARROW's are presented in [A] (Section A.4). In [D], preliminary experimental results are published. The final and complete set of experimental results are presented in [C] (Section C.4) and [E].

# Chapter 6
# Compact Spot-Size Converters

In the previous chapters, expanded mode lasers at 1.55 $\mu$m based on an adiabatic mode transformation were discussed. To obtain low radiation losses ($<$ 1 dB) during the transformation, the taper lengths used to be relatively large. In this chapter, we discuss and use a technique based on modal interference between the two *supermodes* supported by the taper structure formed by the upper active waveguide and the underlying fiber-matched ARROW waveguide [87]. This means that the tapers presented in this chapter are not adiabatic tapers, but multimode interference tapers (see Figure 2.4(a)). We will check by simulation the validity of vertical and lateral ARROW waveguides to design SSC's using this new technique, that offers the possibility of short mode expander regions and relatively low losses. We first introduce the concept of compact bimodal interference tapers. Then, the design process and simulation results are discussed for both the SSC using standard fiber-matched vertical ARROW waveguides and the SSC using lateral ARROW fiber-matched waveguides.

## 6.1 Concept

Figure 6.1(a) shows a simplified two dimensional representation of the adiabatic mode transformation produced in the double core rib tapers considered in this work (the lateral tapering of the real SSC's is shown as a vertical tapering in the figure for clarity purposes). The mode generated in the upper active waveguide is in fact the even supermode $\psi_e$ of the complete structure formed by the active and the lower passive waveguides. In the adiabatic tapers designed in previous chapters this mode carries all the power while it is being transformed and expanded. The odd supermode $\psi_o$ supported by the structure is shown in Figure 6.1(b) for the same taper. This mode is not excited in the adiabatic regime and when the tapered upper rib waveguide reaches cut-off due to the tapering, this mode is not a guided mode any more and becomes a radiation mode.

The mode transformation concept based on the bimodal interference between the two guided supermodes of the taper structure is schematically shown in Figure 6.2. The taper has been drawn twice, one for each supermode, for clarity. Region $A$ represents the mode generated in the straight laser $\psi_e$. In region $B$, an abrupt tapering of the waveguide provokes the transfer of power from this fundamental even mode to the odd mode $\psi_o$ of the structure. In the straight section of region $C$ the two modes propagate without loss and interfere. At the beginning of region $C$ the field is concentrated in the upper active waveguide, but when the supermodes reach the coupling length (when their phase difference $\Delta\phi = \pi$), the field spreads considerably in the lower passive waveguide. In the last section of the taper (region $D$) two relevant phenomena occur. The

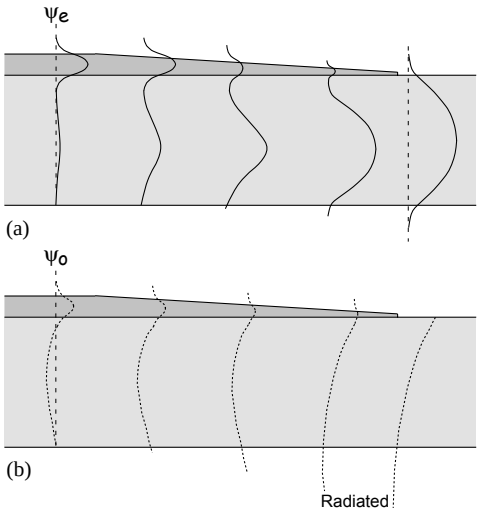


Figure 6.1: In the adiabatic mode transformation concept (a) the even supermode of the taper $\psi_e$ is smoothly transformed into the passive broad mode without loosing any power, and (b) the odd supermode $\psi_o$, which is not excited during the transformation, becomes a radiation mode.

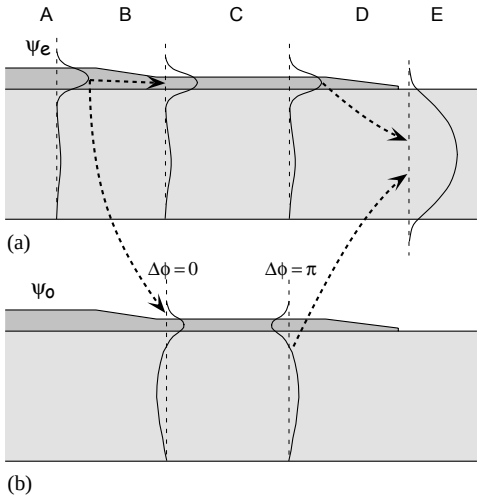


Figure 6.2: Bimodal interference taper concept. (a) The fundamental supermode $\psi_e$ transfers power to (b) the odd supermode $\psi_o$ and the interference between them spreads the field in the fiber-matched waveguide. In the final section, the power couples back to the fundamental mode of the taper.

even mode $\psi_e$ is transformed into the fundamental mode of the underlying fiber-matched waveguide (region $E$); and the power carried by $\psi_o$ is transferred to $\psi_e$ before it becomes a radiation mode.

The technique used to transfer power from the even eigenmode $\psi_e$ to the odd one $\psi_o$ can be understood by the adiabaticity criteria described in Section 2.4 that is developed to design tapered single-mode devices. In the classical equation in the coupled mode theory it is assumed that the transfer of power from the fundamental mode of a taper will be predominantly to the higher order mode with a propagation constant closest to that of the fundamental mode. In the cases we are considering this power-receiving mode is the odd supermode $\psi_o$. Therefore, using slopes that are beyond the critical slope in region $B$ and $D$ we force the power transfer between the fundamental even mode $\psi_e$ and the odd mode $\psi_o$. However, if the slope of this tapering is too sharp we will have undesired radiation to higher order radiation modes that decrease the taper efficiency; thus a compromise between intermodal power transfer and taper efficiency has to be found. Figure 6.3 shows the shape of the lateral tapering of a taper based on bimodal interference. The two abrupt tapers provide the power transfer between the supermodes and in the central straight section the modal interference is produced.

In previous theoretical works [121, 122] the authors do not consider the influence of the underlying slab waveguide in the calculation of the mode of the laser waveguide and they just use a transition of waveguides to excite the two supermodes of the taper structure that induces the power transfer form the upper to the lower waveguide. However, although they do not mention it, this approach could not be used on structures grown on the same wafer and defined using standard processing techniques because the underlying slab core is everywhere on the wafer influencing the shape of the laser mode.

In [87], [123]–[125] the authors make use of the modal interference to reduce the length of the SSC, but they do not give a theoretical explanation of the technique they use to excite the odd supermode of a rib structure similar to the structures considered in this work.

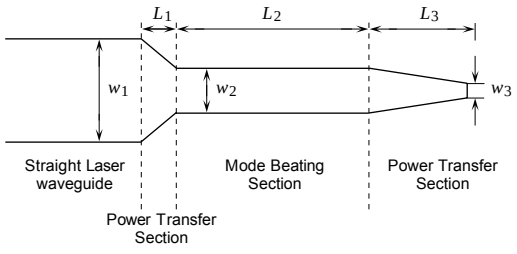


Figure 6.3: Shape of the lateral tapering in a compact taper based on modal interference.

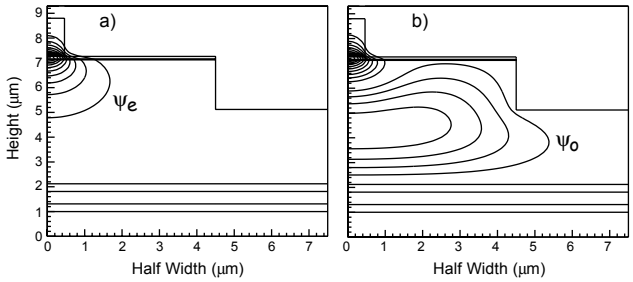


Figure 6.4: (a) Even and (b) odd supermodes supported by the taper structure.

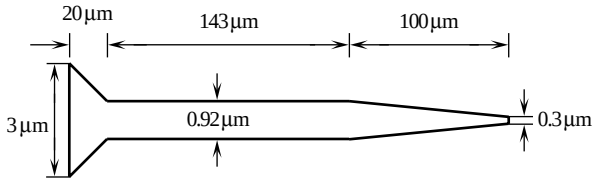


Figure 6.5: Designed shape for the compact taper based on modal interference.

## 6.2 Compact SSC's Using Vertical ARROW's

### 6.2.1 Design and Simulation Results

The taper structure of Figure 3.3 using the vertical relaxed ARROW's supports the two supermodes shown in Figure 6.4.

The commercial eigenmode expansion algorithm *Fimmprop* of Photon Design used for the design of the adiabatic tapers demonstrated not to be a good tool for the simulation of compact tapers based on the resonance coupling. We checked that it introduces considerable calculation errors in the first abrupt part $L_1$ of the taper which makes it undesirable for this task. Therefore, we made use of 3–D BPM (from Optiwave) which has been proven to be a good tool in the simulation of compact SSC's in previous works [87], [123]–[125].

The initial width $w_1$ of the taper is defined by the laser waveguide, which is 3 $\mu$m wide. Then, the first abrupt tapering and the straight section (see Figure 6.3) have been simulated for different values of $L_1$ and $w_2$. The former showed to be no relevant in the behavior of the taper and a value of 20 $\mu$m was chosen. $w_2$ showed a good performance around 0.88 and 0.94 $\mu$m, therefore a value of 0.92 $\mu$m was selected for this parameter (see Figure 6.5). The choice of the length of the straight section is obvious from a plot of the lateral intensity. Then, several simulations of the compact taper were done as a function of $L_3$ to design this parameter. For $L_3 = 100$ $\mu$m, we obtained a mode transformation loss of 1 dB, butt-coupling efficiency to a standard single mode fiber of $-2.6$ $\mu$m, and FWHM divergence angles of 10° (lat.) $\times$ 20° (vert.). A length reduction of

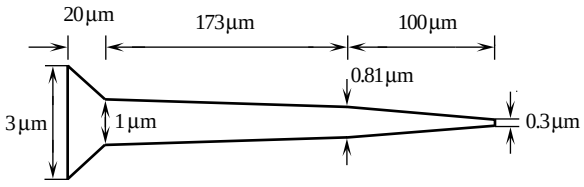


Figure 6.6: Taper shape presenting a smooth slope in the mode beating section.

207 $\mu$m has been achieved compared to the adiabatic method, which required 470 $\mu$m to reach the same mode transformation loss. However, taking the mode transformation loss as a figure of merit, the tolerance of this compact taper design to variations in the width $\Delta w$ and etching depth $\Delta e$ are $\pm 55$ nm and $\pm 30$ nm, respectively, which are rather low considering the fabrication tolerances of standard processing techniques.

### 6.2.2 Tolerant Design

We have observed that defining a smooth slope to the central section, instead of keeping it straight, the modal interference is still achieved and the tolerances to fabrication deviations are improved. The shape shown in Figure 6.6 and designed similarly to the previous straight case is only 30 $\mu$m longer and provides the same fiber-coupling efficiency and far-field divergence angles, but with better tolerances: $\Delta w > \pm 125$ nm and $\Delta e > \pm 40$ nm.

## 6.3 Compact SSC's Using Lateral ARROW's

The same design process has been carried out to design a compact SSC using the fiber-matched lateral ARROW waveguide shown in the schematics of Figure 5.3. The shape of the tapering that provides an efficiency of 90 % at the end of the taper is shown in Figure 6.7. And the intensity plot of the field in the fiber-matched waveguide side is shown in Figure 6.8. We observe that the overall length is 300 $\mu$m which is only slightly smaller than the 320 $\mu$m of the adiabatic

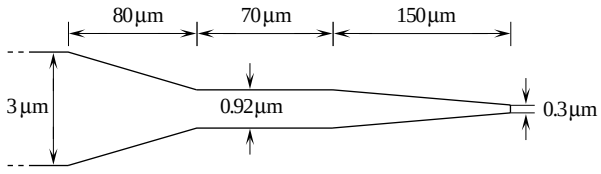


Figure 6.7: The compact shape design for the SSC structure using the fiber-matched lateral ARROW waveguide.

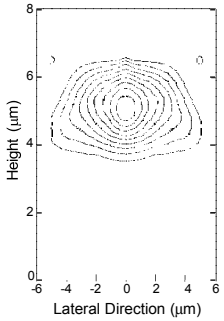


Figure 6.8: Intensity plot at the fiber-matched side of the SSC based on lateral ARROW's and resonant coupling.

mode expander that provided the same efficiency as this one. A quite long first $L_1$ and third $L_3$ sections contribute to a slight improvement. The power transfer that is obtained in the first section is inefficient and therefore, a considerable amount of light power remains in the upper waveguide which needs a long third extinction section to couple to the lower antiguide. The reason of such a bad performance is the fact that *the guidance of the second order supermode is not strong enough*, i.e., the propagation constant of the first radiation mode is too close to the propagation constant of the odd supermode, and this means that the power that should be transferred to it is also collected by radiation modes. This behavior is still more obvious when we try to design SSC's having thicker fiber-matched cores than the 3.5 $\mu$m used in the fabricated laser.

We conclude in this section that the modal interference technique for mode-expansion purposes is not appropriate and cannot be used in SSC's based on lateral ARROW's because of its weak guidance.

## PUBLICATIONS: [F]

A more detailed and complete description of the design process, tolerance analysis and simulation results are presented in [F].

# Chapter 7
# Bending Loss Reduction in Dielectric Waveguides

Curved waveguides pose the following dilemma: the radiation losses increase almost exponentially with decreasing radius of curvature. The successful fabrication of integrated optoelectronic circuits, however, requires that waveguides can change direction over a short distance and with small losses. An optoelectronic integrated circuit has a maximum size and this chip must contain at least a few components. A large radius of curvature is of the order of 1 cm and a short radius of curvature is approximately one hundred times as small and of the order of 100 $\mu$m. What is meant by *low-loss* depends on the system specification or its *power budget*. Generally speaking, we might say that a loss of 0.1 dB for a component is very good, a loss of 1 dB is reasonable but on the high side and a loss of 10 dB is unacceptable. In this chapter we make use of the antiresonance concept used in the confinement of the fiber-matched mode in the previously demonstrated spot-size converters in order to reduce the bending losses in dielectric waveguides. The concept of ARROW bend is introduced in the first section of this chapter. Then, the design formulas are developed. Next, ARROW bend structures are demonstrated by simulation for a rib waveguide configuration on InP and for a buried silica waveguide. Tolerance analysis have been also carried out for both cases.

## 7.1 Introduction

The total loss of a waveguide bend of finite length is due to radiation loss, field mismatch at the transition between the straight and curved waveguide and increased scattering caused by roughness of the outer edge. We discuss these mechanisms subsequently.

1. In straight waveguides, the tendency of light to diffract is compensated by the higher index of refraction of the waveguide core, and the guided mode has a plane wave front. In curved waveguides on the other hand, the wave front rotates around a center of rotation. Since the phase velocity of the wave fronts cannot exceed the local speed of light, there is a point beyond which the wave front curves and where radiation occurs. The radiation losses can be reduced either by increasing the radius of curvature or by introducing a large refractive contrast, the price of which is paid by increased propagation losses due to scattering by edge roughness.

2. In a curved waveguide the intensity distribution shows a shift of its maximum towards the outer edge. For small radii of curvature the mode is

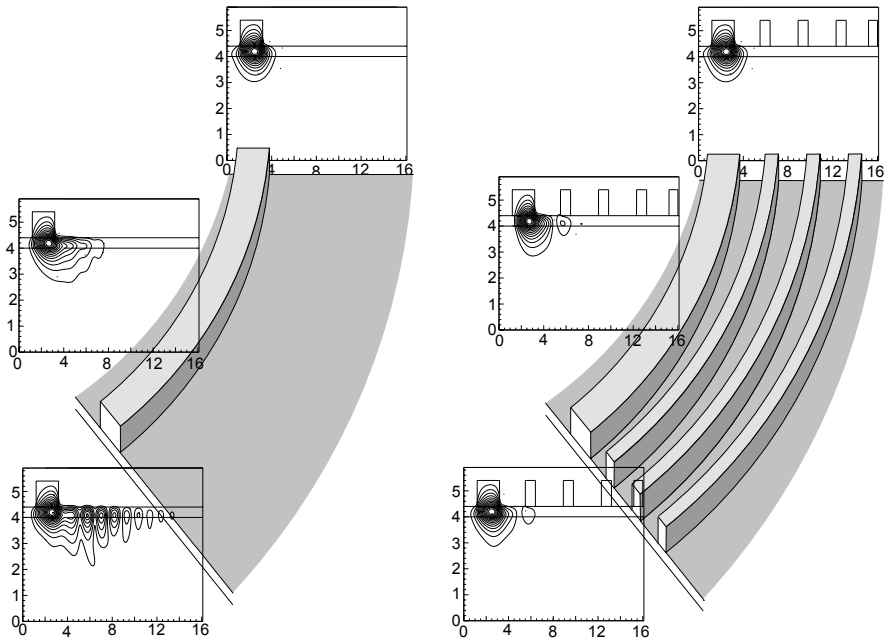

(a) (b)

Figure 7.1: Field distribution in a curved InP ridge waveguide. (a) Standard bend. (b) ARROW bend.

guided by the outer edge alone. The shape of this mode profile is, therefore, not determined by the width of the waveguide bend but mainly by the refractive-index contrast and the radius of curvature, whereas the shape of the straight-waveguide mode profile strongly depends on the width of the waveguide. At the transition between the straight and the curved waveguide, conversion losses will occur because of the mismatch between the two field distributions. These conversion losses can be minimized by introducing a lateral offset between the straight and the curved waveguide in order to align the field maxima, and by optimizing the width of the straight waveguide in order to match the widths of both field distributions.

3. The scattering losses depend on the edge roughness of the ridge waveguide. Therefore, the reduction of this kind of loss mechanism depends on the employed technology.

The radiation loss is the most important loss mechanism in curved waveguides and the one considered in this chapter. Figure 7.1(a) shows the field distribution in a curved ridge waveguide with a radius of 160 $\mu$m. The rib is shallowly

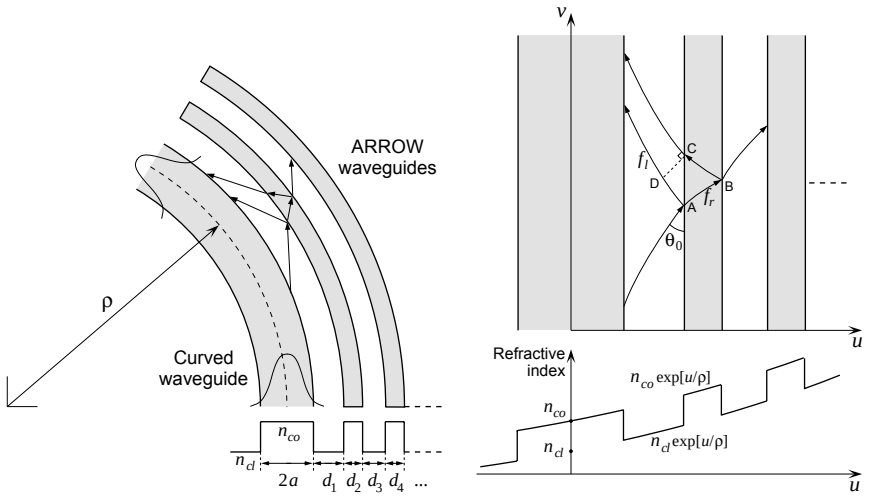


(a) (b)

Figure 7.2: (a) Schematic drawing of the proposed bend concept. (b) Equivalent straight waveguide and modified index profile.

etched and therefore, an important amount of power is axially radiated for a propagation length of only 50 $\mu$m. Placing an antiresonant reflecting structure beyond the outer edge of the bend it would be possible to couple the radiated light back to the waveguide mode [126] and reduce the losses, although the fabrication of the component would become excessively complicated. A simple solution from the fabrication point of view is the use of a set of waveguides defined in the same processing step as the central bend, and designed to provide an antiresonant effect to the radiated light. Figure 7.1(b) shows the propagation of the light field in the same bend as the one shown in Figure 7.1(a), but in this case a group of waveguides, the widths of which are designed to provide an antiresonant reflection to the radiated field, is placed beyond the outer edge of the curved waveguide. We observe that the shape of the mode remains nearly unaltered, and that the leakage due to the bending is negligible compared with the standard case.

## 7.2 Design

Figure 7.2(a) shows a schematic drawing of the concept proposed in this chapter, after application of the *effective index method* in order to reduce one dimension in the analysis. The radiated light is represented by rays that come out from the curved waveguide. Theses rays suffer multiple reflections in the interfaces

defined by the lateral waveguides so that the phase of all of them is the same when they reach again the waveguide. This scheme is similar to that of the ARROW waveguide concept shown in Figure 3.2. Such a process is not a rigorous analysis but, since a full three dimensional simulation is not obvious, we use this common approach to obtain these preliminary promising results.

By the conformal transformation $W = \rho \ln(Z/\rho)$ [127] we transform the step-wise constant refractive index profile of the two-dimensional (2-D) circular geometry $(\rho, \varphi)$ to an exponential refractive index profile in a straight geometry $(u, v)$ in order to simplify the design. Figure 7.2(b) shows the equivalent structure in the $(u, v)$ plane. We see the oblique path defined by the rays that is due to the exponentially increasing refractive index. If we consider as a starting design value the angle $\theta_0$ (see Figure 7.2(b)), defined by a radiated ray when reaching the first ARROW interface, it is straightforward to calculate the ray paths $f_l$ and $f_r$ defined in each medium using Snell's law. Then, emulating the ARROW design theory for multilayer structures of step-wise constant index, the antiresonant condition of each lateral waveguide or gap $d_j$ is numerically calculated from:

$$k_0 \left( 2 \int_{\mathrm{A}}^{\mathrm{B}} f_r(u) n(u) \mathrm{d}u - \int_{\mathrm{A}}^{\mathrm{D}} f_l(u) n(u) \mathrm{d}u \right) + \pi = 2M\pi \qquad (M = 0, 1, 2 \ldots) \tag{7.1}$$

where $k_0$ is the wavenumber in vacuum, $f_l(u)$ and $f_r(u)$ are the path described by two adjacent rays in the mediums of both sides of the interface, $n(u)$ is the exponential equivalent refractive index distribution, and A, B, C and D are the points indicated in Figure 7.2(b).

## 7.3 Simulation Tool (CAMFR)

The straight waveguide with the transformed index profile and the one with the lateral confinement waveguides can be analyzed with a number of techniques, ranging from beam propagation methods (BPM) [128] to eigenmode expansion methods [129]. As BPM is intrinsically an approximate method, eigenmode techniques seem more advantageous. However, in classical eigenmode methods, the structure needs to be enclosed between two perfectly conducting metal walls in order to discretize the mode spectrum. This causes parasitic reflections, because the radiation lost in the bend is totally reflected at the metal walls and can disturb the simulation results. In fact, these parasitic reflections make it completely impossible to determine the radiation losses of the waveguide modes, since they will all have real propagation constants because of energy conservation in lossless media enclosed by perfect reflectors.

Another approach to calculate these radiation losses is to eliminate the metal walls and estimate the losses from the leaky modes of the completely open structure. These leaky modes are complex improper solutions to the open dispersion relation because their fields profiles increase exponentially toward infinity in the cladding [130, 131]. Although this technique is suited to determine the loss of individual modes, it is well-known that leaky modes do not form a complete set

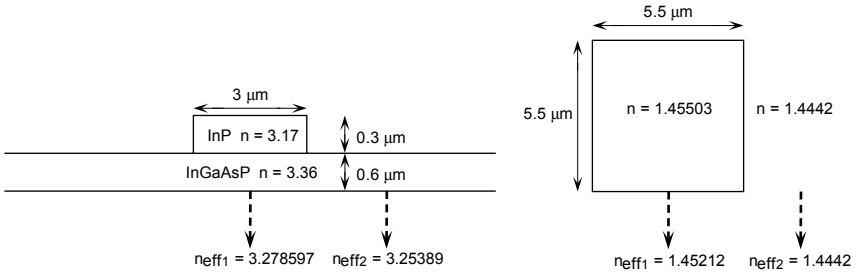


Figure 7.3: (a) In waveguide structure and (b) Buried silica waveguide. Equivalent indexes are also shown.

and can, therefore, generally not be used to describe an arbitrary field. This means that leaky mode expansion is not suited to study , e.g., the minimization of the transition loss between a straight and a curved waveguide, because the scattering at the interface between these two sections will give rise to a field that contains more components than a single leaky mode.

In the simulation of the structures proposed in this chapter we use an eigenmode approach developed in our group at the University of Ghent that avoids all these disadvantages [132, 133]. The tool named CAMFR (CAvity Modelling FRamework) keeps the structure enclosed between two metal walls, but it covers these with a perfectly matched layer (PML), which can absorb incident radiation without any additional parasitic reflections, regardless of wavelength, incidence angle, or polarization [134]. This allows us to accurately model radiation losses, while at the same time keeping a discrete set of eigenmodes.

## 7.4 InP Rib Waveguide

For a first example we assume the InP-InGaAsP rib waveguide shown in Figure 7.3(a). From the imaginary part of the effective index of the fundamental mode calculated by CAMFR, we obtain the radiation losses as a function of bending radius $\rho$ and number of lateral ribs $N$. The results are shown in Figure 7.4(a). TM polarization has been chosen because the ARROW effect is less efficient than for TE polarization and, therefore, the worst case is considered. We observe that the loss in dB is reduced by a factor of 10 using only 3 lateral ribs, and that this loss still decreases approximately another factor of 10 using 9 lateral ribs. From the integration area point of view, we observe that for a certain loss it would be possible to reduce the radius of the bend by a factor of 2, which means that the area can be reduced by a factor of 4. Naturally, the reduction ratio could still be increased defining more than 9 lateral ribs.

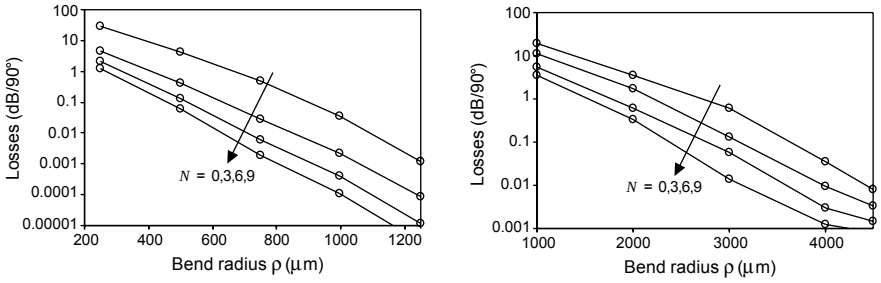


(a) (b)

Figure 7.4: Bending loss per 90° as a function of bend radius and number of lateral waveguides for the (a) InP and (b) silica structures.

A tolerance analysis of the ARROW bends to variations in the width of the lateral waveguides, the etching depth, and polarization has demonstrated that the concept is very strong to typical fabrication deviations. Detailed results are presented in [G].

## 7.5 Silica Buried Waveguide

As a second example we consider the silica-on-silicon waveguide shown in Figure 7.3(b). The required high bending radius due to a low index contrast, is the main disadvantage of silica-on-silicon technology. Figure 7.4(b) shows the calculated bending losses of this new waveguide structure as a function of bending radius $\rho$ and number of lateral ribs $N$, again for TM polarization. Due to the lower index contrast, a higher number of lateral waveguides are needed to reduce the radiation losses compared with the InP technology.

### PUBLICATIONS: [G]

The complete set of simulation results can be found in [G].

# Chapter 8
# Summary and Conclusion

In this chapter we draw conclusions about the approaches proposed and demonstrated along this dissertation. In order to make the deductions more clear, Table 8.1 shows the most significant results as well as a schematic drawing of the considered spot-size converter concept.

## SSC's using Vertical ARROW's

We have demonstrated a new laser emitting at 1.55 $\mu$m wavelength integrated with a spot size converter using an ARROW waveguide for enhanced fiber coupling. The taper transforms the small active laser mode into the fiber-adapted mode of the large underlying mesa with vertical ARROW confinement. Since the thick fiber-matched core of the ARROW waveguide consists of InP, this fact eliminates the need for thick $In_{1-x}Ga_xAs_yP_{1-y}$ layers and the associated growth problems. The growth and fabrication procedure mirrored conventional methods very closely, and these devices are thus amenable to low-cost manufacturability. The yield and uniformity were fairly high as the processing did not involve any critical feature sizes. Threshold currents of around 50 mA were measured, which have to be compared with 30 mA for untapered reference lasers. The far-field FWHM divergence angles were significantly reduced and the coupling efficiency to single mode fiber was improved by 5.4 dB, to a value below 3 dB.

We also calculated that the ARROW cladding thickness can be reduced drastically by moving away from the optimal antiresonance condition without introducing major extra losses. The new structures significantly reduce the overall layer stack thickness (by around 2.1 $\mu$m) while maintaining the far-field divergence angles and the fiber coupling efficiency of the optimum ARROW structures.

## SSC's using Lateral ARROW's

We have presented a new concept for the fabrication of highly efficient and simple-to-fabricate spot-size converters that make use of the ARROW-concept for both the lateral and vertical optical confinement. InGaAsP–InP rib lasers with monolithically integrated SSC's have been demonstrated. The taper transforms the small active laser mode into the fiber-adapted mode of the underlying slab ARROW waveguide. The lateral confinement of the slab mode is achieved by means of an antiresonant/antiguiding effect provided by two sets of lateral rib waveguides defined in the same etch process as the central active ridge. Therefore, only a single planar growth step and a single conventional etching process are required, leading to the simplest SSC concept ever reported. Threshold currents of around 50 mA were measured, which have to be compared with 30 mA for untapered lasers. The far-field FWHM divergence angles were significantly reduced and 4 dB improvement of the coupling efficiency to single mode fiber

| Taper | Laser | $I_{th}$ (mA) | $\eta_d$ (W/A) | $L$ ($\mu$m) | $T_0$ (°K) | $FC$ (dB) | $FF$ (deg.) | Tol. ($\mu$m) |
|---|---|---|---|---|---|---|---|---|
| 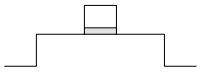 | R–$E_1$ | 31 | 0.09 | 750 | 65 | −8.2 | 30.5 × 43 | ±1.9 × ±2.1 |
| | R–$E_2$ | 30 | 0.13 | 750 | 81 | −8 | 30.1 × 40.1 | ±1.5 × ±2 |
| 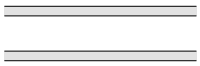 | T–$E_1$ | 45 | 0.1 | 990 | 71 | −2.9 | 10.4 × 22 | ±2 × ±2.2 |
| | T–$E_2$ | 50 | 0.15 | 890 | 65 | −2.6 | 10 × 27 | ±2.2 × ±2.3 |
| 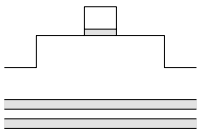 | R–$E_1$ | 35 | 0.13 | 750 | 78 | −8 | 30.3 × 39 | ±1.8 × ±2.1 |
| | R–$E_2$ | 22 | 0.13 | 750 | 68 | −8.2 | 30.9 × 40.7 | ±2 × ±2.3 |
| | T–$E_1$ | 60 | 0.11 | 990 | 70 | −2.7 | 11 × 19 | ±2.3 × ±2.4 |
| | T–$E_2$ | 32 | 0.1 | 890 | 79 | −2.9 | 9.6 × 25 | ±2.4 × ±2.5 |
| 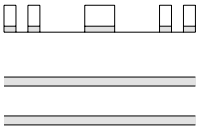 | R–$E_1$ | 35 | 0.12 | 750 | 88 | −8 | 31.5 × 42.8 | ±1.6 × ±2 |
| | R–$E_2$ | 28 | 0.12 | 750 | 65 | −8.3 | 30.7 × 40.6 | ±1.5 × ±2 |
| | T–$E_1$ | 55 | 0.1 | 1040 | 42 | −4 | 13.8 × 30.8 | ±2.3 × ±2.4 |
| | T–$E_2$ | 48 | 0.12 | 1010 | 61 | −4.3 | 13 × 32.7 | ±2.2 × ±2.3 |
| 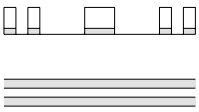 | T–$E_1$ | — | — | — | — | −3.9 | 8.9 × 28 | ±2.1 × ±2.1 |
| | T–$E_2$ | — | — | — | — | −4.1 | 8.1 × 30 | ±2.1 × ±2.2 |
|  | T–$E_2$ | — | — | — | — | −2.4 | 7.2 × 14 | ±2.3 × ±1.9 |
|  | T–Bd | — | — | — | — | −1.1 | 7.2 × 9 | ±2.9 × ±2.3 |

Table 8.1: Measurement results on the integrated mode expanded lasers considered in this thesis. $I_{th}$ = threshold current; $\eta_d$ = external efficiency; $L$ = total laser length; $T_0$ = characteristic temperature; $FC$ = fiber-coupling efficiency; $FF$ = far-field divergence angles; $Tol.$ = 1-dB alignment tolerance. $E_1$ and $E_2$ correspond to shallowly and deeply etched active ribs, respectively. The last groups, without laser characteristics, correspond to simulation results, because they have not been fabricated yet. R and T stand for reference and tapered lasers, respectively.

was observed.

We also calculated the relaxed ARROW cladding layers that would reduce the overall layer stack thickness by around 1 $\mu$m. Simulation results showed a slight improvement of the fiber-coupling efficiency and far-field divergence angles compared to the demonstrated optimum mode-expanded laser.

We have demonstrated the possibility of improving the performance of this new concept by using a higher number of ARROW lateral confining ribs for thicker fiber-matched cores. These devices did not show a good fiber-coupling efficiency because we used the mask with the taper shapes optimized for 3.5 $\mu$m-thick core layers for a 5 $\mu$m-thick ARROW waveguide.

Two variants of the demonstrated concept have also been analyzed by simulation and are expected to show a better performance. In a first variant a weakly-guiding slab waveguide substitutes the thicker core of the first structure. In a second variant the taper concept of this work is integrated in a buried laser structure. Simulation results show considerable improvements in the far-field divergence angles and fiber-coupling efficiencies.

## Compact SSC's

Compact mode converters were designed for both demonstrated taper concepts (vertical ARROW and vertical and lateral ARROW combined) based on a modal interference between the two supermodes of the structure. Efficient and low-loss mode transformation were simulated for much shorter lengths as compared to the adiabatic devices. Nevertheless, due to the weak guidance of the mode-expanders using lateral ARROW's no robust and tolerant compact tapers can be designed for them.

## ARROW Bends

We have analyzed the application of the ARROW effect in the reduction of bending loss in dielectric waveguides. A set of properly designed waveguides defined in the same processing step as the central one and not requiring special techniques provides significant bending loss reduction. We see that for a certain loss it would be possible to reduce the radius of the bend by a factor of 2, which means that the integration area can be reduced by a factor of 4, and, what is most important, without changing a bit the required fabrication process of the curved waveguide. Applicability on InP and Si technologies have been analyzed with promising results.

## Future Work

The logical extension of the present work is the integration of the proposed mode expanders with other optoelectronic components as well as with Fabry-Pérot lasers, such as SOA's (semiconductor optical amplifiers), optical regenerators, switches, delay lines, wavelength de/multiplexers, modulators,...

Naturally, the proposed SSC's that have only been analyzed by simulation can be fabricated and measured. This is the case of the compact design and the two proposed variants of the SSC using the lateral ARROW's.

A mask incorporating ARROW bends has already been designed in order to

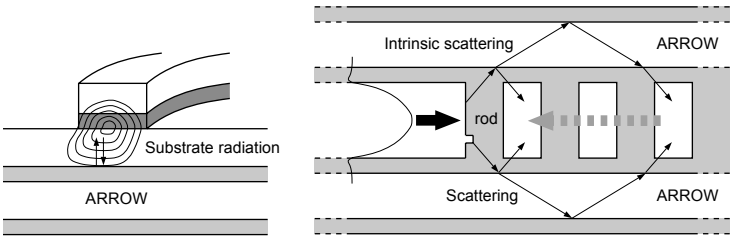


(a) (b)

Figure 8.1: Applicability of ARROW effect in the reduction of radiation in (a) strongly confined bend waveguides and (b) photonic crystals.

investigate them in a passive InP wafer.

The ARROW concept could be investigated in other applications such as the reduction of radiation towards the substrate in strongly confined bend waveguides (see Figure 8.1(a)), and in the reduction of scattering losses in 2D photonic crystals (Figure 8.1(b)).

# Bibliography


[1] L. Eldada, "Advances in telecom and datacom optical components", *Opt. Eng.*, vol. 40, no. 7, pp. 1165–1178, Jul. 2001.

[2] T. Van Caenegem, PhD Thesis, "Development of monolithic integration techniques by means of selective area growth and MOVPE for the realisation of photonic integrated circuits for telecom applications", *University of Ghent*, 2001.

[3] W. Hunziker, "Low-cost packaging of semiconductor laser arrays", *Circuits & Devices*, vol. 1, pp. 19–25, Jan. 1997.

[4] D. Van Thourhout, PhD Thesis, "Multiwavelength lasers for WDM-networks. Theory, design and realisation by hybrid integration", *University of Gent*, May 2000.

[5] P. Karioja, and D. Howe, "Diode-laser-to-waveguide butt couping", *Appl. Optics*, vol. 35, no. 3, pp. 4004–416, Jan. 1996.

[6] I. Moerman, P. Van Daele, and P. M. Demeester, "A review on fabrication technologies for the monolithic integration of tapers with III–V semiconductor devices", *IEEE J. Sel. Top. Quantum Electron.*, vol. 3, no. 6, pp. 1308–1320, Dec. 1997.

[7] B. Mersali, A. Ramdane, and A. Carenco, "Optical-mode transformer: A III–V circuit integration enabler", *IEEE J. Sel. Top. Quantum Electron.*, vol. 3, no. 6, pp. 1321–1331, Dec. 1997.

[8] A. Lestra, and J.-Y. Emery, "Monolithic integration of spot-size converters with 1.3-$\mu$m lasers and 1.55-$\mu$m polarization insensitive semiconductor optical amplifiers", *IEEE J. Sel. Top. Quantum Electron.*, vol. 3, no. 6, pp. 1429–1440, Dec. 1997.

[9] K. De Mesel, I. Moerman, R. Baets, B. Dhoedt, P. Van Daele, and J. Stulemeijer, "Spot size converters for low-cost PICs", in *Proc. 9th Eur. Conf. on Integr. Opt. (ECIO '99)*, Torino, Italy, pp. 253–258.

[10] E. S. Kintzer, J. N. Walpone, S. R. Chinn, C. A. Wang, and L. J. Missagia, "High-power, strained amplifiers and lasers with tapered gain regions", *IEEE Photon. Technol. Lett.*, vol. 5, no. 6, pp. 605–608, Jun. 1993.

[11] H. Sato, M. Aoki, M. Takahashi, M. Komori, K. Uomi, and S. Tsuji, "1.3 $\mu$m beam-expander integrated laser grown by single-step MOVPE", *Electron. Lett.*, vol. 31, no. 15, pp. 1241–1242, Jul. 1995.

[12] K. Shinoda, K. Hiramoto, M. Sagawa, T. Toyonaka, and K. Uomi, "Circular beam, high power operation of 0.98 $\mu$m InGaAs/InGaAsP lasers with a tapered waveguide spot-size expander", *Electron. Lett.*, vol. 32, no. 12, pp. 1101–1102, Jun. 1996.

[13] R. N. Thurston, E. Kapon, and A. Shahar, "Two-dimensional control of mode size in optical channel waveguides by lateral channel tapering", *Opt. Lett.*, vol. 16, no. 5, pp. 306–308, Mar. 1991.

[14] P. Doussiere, P. Garabedian, C. Graver, E. Derouin, E. Gaumont-Goarin, G. Michaud, and R. Meilleur, "Tapered active stripe for 1.5-$\mu$m InGaAsP/InP strained multiple quantum well lasers with reduced beam divergence", *Appl. Phys. Lett.*, vol. 64, no. 5, pp. 539–541, Jan. 1994.

[15] Y. Inaba, M. Kito, T. Nishikawa, M. Ishino, and Y. Matsui, "High-temperature operation of 1.3-$\mu$m tapered-active-stripe laser for direct coupling to single-mode fiber", *IEEE J. Sel. Top. Quantum Electron.*, vol. 3, no. 6, pp. 1399–1404, Dec. 1997.

[16] S, H. Groves, J. P. Donnelly, J. N. Walpone, J. D. Woodhouse, L. J. Missagia, R. J. Bailey, and A. Napoleone, "Strained-layer InGaAsP diode lasers with tapered gain region for operation at $\lambda = 1.3$ $\mu$m", *IEEE Photon. Technol. Lett.*, vol. 6, no. 11, pp. 1286–1288, Nov. 1994.

[17] M. Sagawa, K. Hiramoto, N. Toyonaka, T. Kikawa, and K. Uomi, "High-power and highly-reliable operation of 0.98 $\mu$m lasers with an exponential-shape flared stripe", in *Proc. 9th Annu. Meet. IEEE Lasers and Electro-Optics Soc.*, pp. 42–43, paper ME2, 1996.

[18] H. S. Cho, K. H. Park, J. K. Lee, D. H. Jang, J. S. Kim, K. S. Park, C.-S. Park, and K.-E. Pyum, "Unbalanced facet output power and large spot size in 1.3 $\mu$m tapered active stripe lasers", *Electron. Lett.*, vol. 33, no. 9, pp. 781–782, Apr. 1997.

[19] K. Kasaya, Y. Kondo, M. Okamoto, O. Mitomi, and M. Naganuma, "Monolithically integrated DBR lasers with simple tapered waveguide for low-loss fiber coupling", *Electron. Lett.*, vol. 29, no. 33, pp. 2067–2068, Nov. 1993.

[20] P. Doussiere, P. Garabedian, C. Graver, D, Bonnevie, T. Fillion, E. Derouin, M. Monnot, J. G. Provost, D. Leclerc, and M. Klenk, "1.55 $\mu$m polarisation independent semiconductor optical amplifier with 25 dB fiber to fiber gain", *IEEE Photon. Technol. Lett.*, vol. 6, no. 2, pp. 170–172, Feb. 1994.

[21] D. Tishinin, K. Uppal, I. Kim, and P. D. Dapkus, "1.3-$\mu$m polarization insensitive amplifiers with integrated-mode transformes", *IEEE Photon. Technol. Lett.*, vol. 9, no. 10, pp. 1337–1339, Oct. 1997.

[22] R. Zengerle, O. Leminger, W. Weiershausen, K. Faltin, and B. Hübner, "Laterally tapered InP–InGaAsP waveguides for low-loss chip-to-fiber butt coupling: a comparison of different configurations", *IEEE Photon. Technol. Lett.*, vol. 7, no. 5, pp. 532–534, May 1995.

[23] O. Mitomi, K. Kasaya, and H. Miyazawa, "Design of a single-mode tapered waveguide for low-loss chip-to-fiber coupling", *IEEE J. Quantum Electron.*, vol. 30, no. 8, pp. 1787–1793, Aug. 1994.

[24] H. Bissessur, C. Graver, O. Le Gouezigou, G. Michaud, and F. Gaborit, "Ridge laser with spot-size converter in a single epitaxial step for high coupling efficiency to single-mode fibers", *IEEE Photon. Technol. Lett.*, vol. 10, no. 9, pp. 1235–1237, Sep. 1998.

[25] K. De Mesel, R. Baets, C. Sys, S. Verstuyft, I. Moerman, and P. Van Daele, "First demonstration of 980 nm oxide confined laser with integrated spot size converter", *Electron. Lett.*, vol. 36, no. 12, pp. 1028–1029, Jun. 2000.

[26] S. S. Saini, F. G. Johnson, D. R. Stone, H. Shen, W. Zhou, and M. Dagenais, "Passive active resonant coupler (PARC) platform with mode expander", *IEEE Photon. Technol. Lett*, vol. 12, no. 8, pp. 1025–1027, Aug. 2000.

[27] G. A. Vawter, C. T. Sullivan, J. R. Wendt, R. E. Smith, H. Q. Hou, and J. F. Klem, "Tapered rib adiabatic following fiber couplers in etched GaAs materials for monolithic spot-size transformation", *IEEE J. Sel. Top. Quantum Electron.*, vol. 3, no. 6, pp. 1361–1371, Dec. 1997.

[28] P. V. Studenkov, F. Xia, M. R. Gokhale, and S. R. Forrest, "Asymmetric twin-waveguide 1.55-$\mu$m wavelength laser with a distributed bragg reflector", *IEEE Photon. Technol. Lett.*, vol. 12, no. 5, pp. 468–470, May 2000.

[29] J. G. Bauer, M. Schier, and G. Ebbinghaus, "High responsivity integrated tapered waveguide PIN photodiode", in *Proc. 19th Eur. Conf. Optical Communication (ECOC '93)*, Montreux, Switzerland, pp. 277–280.

[30] C. F. Janz, A. M. Gulisano, and R. G. Walker, "Improved fiber coupling to GaAs/AlGaAs rib waveguides using a regrowth-free mode 'drive-down' technique", *Electron. Lett.*, vol. 32, no. 11, pp. 1002–1003, May 1996.

[31] R. Ben-Michael, U. Koren, B. I. Miller, M. G. Young, M. Chien, and G. Raybon, "InP-based multiple quantum well lasers with an integrated tapered beam expander waveguide", *IEEE Photon. Technol. Lett.*, vol. 6, no. 12, pp. 1412–1414, Dec. 1994.

[32] J. V. Collins, I. F. Lealman, A. Kelly, and C. W. Ford, "Pasive alignment of second generation optoelectronics devices", *IEEE J. Sel. Top. Quantum Electron.*, vol. 3, no. 6, pp. 1441–1444, Dec. 1997.

[33] R. Y. Fang, D. Bertone, M. Meliga, G. Magnetti, G. Morello, S. Murgia, G. Oliveti, R. Paoletti, and G. Rossi, "1.55-$\mu$m InGaAsP–InP spot-size-converter (SSC) laser with simple technological process", *IEEE Photon. Technol. Lett*, vol. 10, no. 6, pp. 775–777, Jun. 1998.

[34] B. Hübner, G. Vollrath, R. Ries, C. Gréus, H. Janning, E. Rönneberg, E. Kuphal, B. Kempf, R. Göbel, F. Fiedler, R. Zengerle, and H. Burkhard, "Laser diodes with integrated spot-size transformer as low-cost optical transmitter elements for telecommunications", *IEEE J. Sel. Top. Quantum Electron.*, vol. 3, no. 6, pp. 1372–1383, Dec. 1997.

[35] A. Kasukawa, N. Iwai, N. Yamanaka, and N. Yokouchi, "Output beam characteristics of 1.3 $\mu$m GaInAsP/InP SL-QW lasers with narrow and circular output beam", *Electron. Lett.*, vol. 31, no. 7, pp. 559–560, Mar. 1995.

[36] K. Kawano, M. Hiroshi, H. Okamoto, Y. Itaya, and M. Naganuma, "Coupling and conversion characteristics of spot-size-converter integrated laser diodes", *IEEE J. Sel. Top. Quantum Electron.*, vol. 3, no. 6, pp. 1351–1360, Dec. 1997.

[37] B. Thédrez, J. M. Rainsant, V. Voiriot, J. L. Lafragette, L. Roux, A. Pinquier, and B. Fernier, "1.55 $\mu$m DFB lasers with intergrated spot size converters operating at 2.5 Gbit/s with modulated power over 20 mW for 180 km transmission", in *Proc. OFC '99*, pp. 140–142.

[38] W. Rehm, K. Adam, A. Göth, W. Jörg, J. Laucjner, J. Scherb, P. Aribaudm C. Artigue, C. Duchemin, B. Fernier, E. Grard, D. Keller, S. Kerboeuf, S. Rabaron, J. M. Rainsant, D. Tregoat, J. L. Nicque, A. Tournereau, P. J. Laroulandie, and P. Berthier, "Low-cost modules for SMT", *Electron. Comp. Technol. Conf. (ECTC'00)*.

[39] M. Bachmann, P. Doussière, J. Y. Emery, R. N'Go, F. Pommereau, L. Goldstein, G. Soulage, and A. Jourdan, "Polarisation-insensitive clamped-gain SOA with integrated spot-size converter and DBR gratings for WDM applications at 1.55 $\mu$m wavelength", *Electron. Lett.*, vol. 32, no. 22, pp. 2076–2078, Oct. 1996.

[40] B. Mersali, H. J. Brücker, M. Feuillade, S. Sainson, A. Ougazzaden, and A. Carenco, "Theoretical and experimental studies of a spot-size transformer with integrated waveguide for polarization insensitive optical amplifiers", *J. Lightwave Technol.*, vol. 13, no. 9, pp. 1865–1872, Sep. 1995.

[41] Th. Schwander, S. Fischer, A. Krämer, M. Laich, K. Luksic, G. Spatschek, and M. Warth, "Simple and low-loss fibre-to-chip coupling by integrated field-matching waveguide in InP", *Electron. Lett.*, vol. 29, no. 4, pp. 326–328, Feb. 1993.

[42] R. S. Fan, and R. B. Hooker, "Tapered polymer single-mode waveguide for mode transformation", *J. Lightwave Technol.*, vol. 17, no. 3, pp. 466–474, Mar. 1999.

[43] K. Kawano, M. Kohtoku, N. Yoshimoto, S. Sekine, and Y. Noguchi, "2 $\times$ 2 InGaAlAs/InAlAs multiquantum well (MQW) directional-coupler waveguide-switch modules integrated with spot-size converters", *Electron. Lett.*, vol. 30, no. 4, pp. 353–354, 1994.

[44] I. Moerman, M. D'Hondt, W. Vanderbauwhede, J. Haes, L. Van Wassenhove, P. De Dobbelaere, R. Baets, P. Van Daele, P. Demeester, W. Hünziker, and C. Holtmann, "Vertically tapered InGaAsP/InP waveguides and lasers resulting in low-loss fiber-chip coupling", in *Proc. 20th. Eur. Conf. Optical Communication (ECOC '94)*, Firenze, Italy, pp. 1027–1030.

[45] R. J. Deri, C. Caneau, E. Colas, L. M. Schiavone, N. C. Andreadakis, G. H. Song, and E. C. M. Pennings, "Integrated optic mode-size tapers by selective organometallic chemical vapour deposition of InGaAsP/InP", *Appl. Phys. Lett.*, vol. 61, no. 8, pp. 952–954, Aug. 1992.

[46] D. E. Bossi, W. D. Goodhue, L. M. Johnson, and R. H. Rediker, "Reduced-confinement GaAlAs tapered waveguide antennas for enhanced far-field beam directionality", *IEEE J. Quantum Electron.*, vol. 27, no. 3, pp. 687–695, Mar. 1991.

[47] K. Kato, and Y. Tohmori, "PLC hybrid integration technology and its application to photonic components", *IEEE J. Sel. Top. Quantum Electron.*, vol. 6, no. 1, pp. 4–13, Jan./Feb. 2000.

[48] H.-S. Kim, D. K. Oh, M.-H. Park, N. Hwang, and I.-H. Choi, "1.55 $\mu$m spot-size converter integrated-laser diode fabricated by selective-area metalorganic vapor-phase epitaxy", *Microw. Opt. Technol. Lett*, vol. 25, no. 5, pp. 300–302, Jun. 2000.

[49] A. Kasukawa, K. Nishikata, N. Yamanaka, S. Arakawa, N. Iwai, T. Mukaihara, and T. Matsuda, "Structural dependence of 1.3-$\mu$m narrow-beam lasers fabricated by selective MOCVD growth", *IEEE J. Sel. Top. Quantum Electron.*, vol. 3, no. 6, Dec. 1997.

[50] H. Yamazaki, K. Kudo, T. Sasaki, J. Sasaki, Y. Furushima, Y. Sakata, M. Itoh, and M. Yamaguchi, "1.3-$\mu$m spot-size-converter integrated laser diodes fabricated by narrow-stripe selective MOVPE", *IEEE J. Sel. Top. Quantum Electron.*, vol. 3, no. 6, pp. 1392–1398, Dec. 1997.

[51] H. Kobayashi, T. Yamamoto, M. Ekawa, T. Watanabe, T. Idhikawa, T. Fujii, H. Soda, S. Ogita, and M. Kobayashi, "Narrow-beam divergence 1.3-$\mu$m multiple-quantum-well laser diodes with monolithically integrated tapered thickness waveguide", *IEEE J. Sel. Top. Quantum Electron.*, vol. 3, no. 6, pp. 1384–1391, Dec. 1997.

[52] M. Aoki, M. Komori, M. Suzuki, H. Sato, M. Takahashi, T. Ohtsoki, K. Uomi, and S. Tsuji, "Wide-temperature-range operation of 1.3 $\mu$m beam expander-integrated laser diodes grown by in-plane thickness control MOVPE using a silicon shadow mask", *IEEE Photon. Technol. Lett.*, vol. 8, no. 4, pp. 479–481, Apr. 1996.

[53] M. Muramaki, "Mitsubishi laser diode achieves 11° spread angle", *Semiconduct. Int.*, pp. 48, Dec. 1995.

[54] I. Moerman, M. D'Hondt, W. Vanderbauwhede, G. Coudenys, J. Haes, P. De Dobbelaere, R. Baets, P. Van Daele, and P. Demeester, "Monolithic integration of a spot size transformer with a planar buried heterostructure in GaAsP/InP-laser using the shadow masked growth technique", *IEEE Photon. Technol. Lett.*, vol. 6, no. 8, pp. 888–890, Aug. 1994.

[55] Y. Suzaki, K. Magari, Y. Kondo, Y. Kawaguchi, Y. Kadota, and K. Yoshino, "High-gain array of semiconductor optical amplifier integrated with bent spot-size converter (BEND SS-SOA)", *J. Lightwave Technol.*, vol. 19, no. 11, pp. 1745–1750, Nov. 2001.

[56] D. Jang, J. Shim, J. Lee, and Y. Eo, "Asymmetric output characteristics in 1.3-$\mu$m spot-size converted laser diodes", *IEEE J. Quantum Electron.*, vol. 37, no. 12, Dec. 2001.

[57] C.-H. Chen, S. C. Shunk, U. Koren, M. Chien, B. I. Miller, K. F. Dreyer, H. M. Presby, and R. G. Ahrens, "Semiconductor optical amplifier array coupled to uncoated flat-end fibers with integrated beam expanders and $TiO_2$ antireflection coatings", *IEEE J. Sel. Top. Quantum Electron.*, vol. 3, no. 6, pp. 1421–1428, Dec. 1997.

[58] G. Müller, B. Stegmüller, H. Westermeier, and G. Wenger, "Tapered InP/InGaAsP waveguide structure for efficient fiber-chip coupling", *Electron. Lett.*, vol. 27, no. 20, pp. 1836–1838, Feb. 1994.

[59] T. Brenner, R. Hess, and H. Melchior, "Compact InGaAsP/InP laser diodes with integrated mode expander for efficient coupling to flat-ended singlemode fibers", *Electron. Lett.*, vol. 31, no. 17, pp. 1443–1445, Aug. 1995.

[60] G. Vermeire, F. Vermaerke, I. Moerman, J. Haes, R. Baets, P. Van Daele, and P. Demeester, "Monolithic integration of a SQW laser diode and a mode-size converter using masked MOVPE growth", *J. Cryst. Growth*, vol. 145, no. 1–4, pp. 875–880, Dec. 1994.

[61] J. Stulemeijer, PhD Thesis, "Integrated optics for microwave phased-array antenans", *Delft University*, 2002.

[62] L. Mörl, C. M. Weinert, F. Reier, L. Stoll, and H.-P. Nolting, "Uncladded InGaAsP/InP rib waveguides with integrated thicknesss tapers for efficient fiber-chip butt coupling", *Electron. Lett*, vol. 32, no. 1, pp. 36–38, Jan. 1996.

[63] G. Wenger, L. Stoll, B. Weiss, M. Schienle, R. Müller-Nawrath, S. Eichinger, J. Müller, B. Acklin, and G. Müller, "Design and fabrication of monolithic optical spot size transformers (MOST's) for highly efficient fiber-chip coupling", *J. Lightwave Technol.*, vol. 12, no. 10, pp. 1782–1790, Oct. 1994.

[64] G. Müller, L. Stoll, G. Wenger, and M. Schienle, "First low loss InP/InGaAsP optical switch with integrated mode transformers", in *Proc. Eur. Conf. Optical Communication (ECOC)*, Florence, Italy, pp. 37–40, 1993.

[65] M. Aoki, M. Komori, H. Sato, T. Tsuchiya, A. Taike, M. Takahshi, K. Uomi, and S. Tsuji, "Reliable wide-temperature-range operation of 1.3-$\mu$m beam-expander integrated laser diode for passively aligned optical modules", *IEEE J. Sel. Top. Quantum Electron.*, vol. 3, no. 6, pp. 1405–1412, Dec. 1997.

[66] L. J. P. Ketelsen, J. A. Grenko, S. K. Sputz, M. W. Focht, J. M. Vandenberg, J. E. Johnson, C. L. Reynolds, J. M. Geary, J. Levkoff, K. G. Glogovsky, D. V. Stampone, S. N. G. Chu, T. Siegrist, T. L. Pernell, F. S. Walters, J. Sheridan-Eng, J. L. Lentz, M. A. Alam, R. People, M. S. Hybersten, E. D. Isaacs, K. Evans-Lutterodt, R. E. Leibenguth, G. J. Pryzbilek, L. Zhang, K. Feder, S. Shunk, D. M. Tennant, L. J. Peticolas, D.M. Romero, J. M. Freund, B. S. Falk, N. N. Tzafaras, L. E. Smith, L. C. Luther, M. Geva, W. A. Gault, and J. L. Zilko, "Multiwavelength DFB laser array with integrated spot size converters", *IEEE J. Quantum Electron.*, vol. 36, no. 6, pp. 641–647, Jun. 2000.

[67] N. Yoshimoto, K. Kawano, H. Takeuchi, S. Kondo, and Y. Noguchi, "Highly efficient coupling semiconductor spot-size converter with an InP/InAlAs multiple-quantum-well core", *Appl. Optics*, vol. 34, no. 6, pp. 1007–1014, Feb. 1995.

[68] H. Jeon, J.-M. Verdeil, M. Ziari, and A. Mathur, "High-power low-divergence semiconductor lasers for GaAs-based 980-nm and InP-based 1550-nm applications", *IEEE J. Sel. Top. Quantum Electron.*, vol. 3, no. 6, pp. 1344–1350, Dec. 1997.

[69] J. E. Johnson, L. J. P. Ketelsen, J. A. Grenko, S. K. Sputz, J. Vandenberg, M. W. Focht, D. V. Stampone, L. J. Peticolas, L. E. Smith, K. G. Glogovsky, G. J. Przybylek, S. N. G. Chu, J. L. Lentz, N. N. Tzafaras, L. C. Luther, T. L. Pernell, F. S. Walters, D. M. Romero, J. M. Freund, C. L. Reynolds, L. A. Gruezke, R. People, and M. A. Alam, "Monolithically integrated semiconductor optical amplifier and electroabsorption modulator with dual-waveguide spot-size converter input", *IEEE J. Sel. Top. Quantum Electron.*, vol. 6, no. 1, pp. 19–25, Jan./Feb. 2000.

[70] H. Hatakeyama, T. Tamanuki, K. Mori, T. Ae, T. Sasaki, and M. Yamaguchi, "Uniform and high-performance eight-channel bent waveguide SOA array for hybrid PICs", *IEEE Photon. Technol. Lett.*, vol. 13, no. 5, pp. 418–420, May 2001.

[71] B. Mersali, F. Ghirardi, J. Brandon, G. Herve-Gruyer, and A. Carenco, "Low-loss fiber-matched diluted multiple quantum well waveguides", *Proc. Inst. Elect. Eng.-Optoelectronics*, vol. 141, no. 5, pp. 296-298, Oct. 1994.

[72] B. Jacobs, R. Zengerle, K. Faltin, and W. Weiershausen, "Vertically tapered spot size transformers fabricated by a simple masking technique", *Electron. Lett.*, vol. 31, no. 10, pp. 794–796, May 1995.

[73] T. Brenner, W. Hunziker, M. Smit, M. Bachmann, G. Guekos, and H. Melchior, "Vertical InP/InGaAsP tapers for low-loss optical fiber waveguide coupling", *Electron. Lett*, vol. 28, no. 22, pp. 2040–2041, Oct. 1992.

[74] N. Yoshimoto, K. Kawano, H. Takeuchi, S. Kondo, and Y. Noguchi, "Spot size converters using InP/InAlAs multi quantum well waveguides for low-loss singlemode fiber coupling", *Electron. Lett.*, vol. 28, no. 17, pp. 1610–1611, Aug. 1992.

[75] G. Müller, B. Stegmüller, H. Westermeier, and G. Wenger, "Tapered In/InGaAsP waveguide structure for efficient fiber-chip coupling", *Electron. Lett.*, vol. 27, no. 20, pp. 1836–1838, Sep. 1991.

[76] T. Nakamura, and N. Suzuki, "Spot-size converted laser diodes based on mode interference", *IEEE Photon. Technol. Lett.*, vol. 12, no. 2, pp. 143–145, Feb. 2000.

[77] J. Buus, W. J. Stewart, J. Haes, J. Willens, and R. G. Baets, "Spot size expansion for laser-to-fiber coupling using an integrated multimode coupler", *J. Lightwave Technol.*, vol. 11, no. 4, pp. 582–588, Apr. 1993.

[78] M. M. Spühler, B. J. Offrein, G.-L Bona, R. Germann, I. Massarek, and D. Erni, "A very short planar silica spot-size converter using a nonperiodic segmented waveguide", *J. Lightwave Technol.*, vol. 16, no. 9, Sep. 1998.

[79] M. H. Chou, M. A. Arbore, and M. M. Fejer, "Adiabatically tapered periodic segmentation of channel waveguides for mode-size transformation and fundamental mode excitation", *Opt. Lett.*, vol. 21, no. 11, pp. 794–796, Jun. 1996.

[80] H. Kosaka, T. Kawashima, A. Tomita, T. Sato, and S. Kawakami, "Photonic-crystal spot-size converter", *Appl. Phys. Lett.*, vol. 76, no. 3, pp. 268–270, Jan. 2000.

[81] J. D. Love, W. M. Henry, W. J. Stewart, R. J. Black, S. Lacroix, and F. Gonthier, "Tapered single-mode fibers and devices. Part 1: Adiabaticity criteria", *IEE Proc.-J*, vol. 138, no. 5, pp. 343–354, Oct. 1991.

[82] C. Vassallo, *Optical waveguide concepts*, Elsevier, Amsterdam, 1991.

[83] K. De Mesel, PhD Thesis, "Spot-size converters for photonic integrated circuits", *University of Ghent*, 2002.

[84] Photon Design, "http://www.photond.com".

[85] Optiwave Corporation, "http://www.optiwave.com".

[86] P. Sewell, T. M. Benson, and P. C. Kendall, "Rib waveguide spot-size transformers: Modal properties", *J. Lightwave Technol.*, vol. 17, no. 5, pp. 848–856, May 1999.

[87] V. Vusirikala, S. S. Saini, R. E. Bartolo, S. Agarwala, R. D. Whaley, F. G. Johnson, D. R. Stone, and M. Dagenais, "1.55-$\mu$m InGaAsP–InP laser arrays with integrated-mode expanders fabricated using a single epitaxial growth", *IEEE J. Select. Top. Quantum Electron.*, vol. 3, no. 6, pp. 1332–1343, Dec. 1997.

[88] M. A. Duguay, Y. Kokubun, T. L. Koch, and L. Pfeiffer, "Antiresonant reflecting optical waveguides in $SiO_2$-Si multilayer structures", *Appl. Phys. Lett.*, vol. 49, no. 1, pp. 13–15, Jul. 1986.

[89] Y. Kokubun, T. Baba, and T. Sakaki, "Low-loss antiresonant reflecting optical waveguide on Si substrate in visible-wavelength region", *Electron. Lett.*, vol. 22, no. 17, pp. 892–893, Aug. 1986.

[90] T. Baba, T. Sakaki, and K. Iga, "Loss reduction of an ARROW waveguide in shorter wavelength and its stack configuration", *J. Lightwave Technol.*, vol. 6, no. 9, pp. 1440–1445, Sep. 1988.

[91] T. L. Koch, U. Koren, G. D. Boyd, P. J. Corvini, and M. A. Duguay, "Antiresonant reflecting optical waveguides for III–V integrated optics", *Electron. Lett.*, vol. 23, no. 5, pp. 244–245, Feb. 1987.

[92] J. M. Kubica, A. Malag, J. Gazecki, M. W. Austin, and G. K. Reeves, "AlGaAs/GaAs ARROW waveguides", *Electron. Lett.*, vol. 29, no. 12, pp. 1058–1060, Jun. 1993.

[93] M. Mann, U. Trutschel, C. Wächter, L. Leine, and F. Lederer, "Directional coupler based on an antiresonant reflecting optical waveguide", *Opt. Lett.*, vol. 16, no. 11, pp. 805–807, Jun. 1991.

[94] K. .K. H. Lee, and W. Steenaart, "Analysis of $N \times N$ passive optical star coupler based on the normal modes of $N$ input waveguides", *J. Lightwave Technol.*, vol. 10, no. 12, pp. 1800–1805, Dec. 1992.

[95] S. T. Chu, W. Pan, S. Sato, B. E. Little, T. Kanelo, and Y. Kokubun, "ARROW-type vertical coupler filter: Design and fabrication", *J. Lightwave Technol.*, vol. 17, no. 4, pp. 652–658, Apr. 1999.

[96] V. Delisle, U. Trustschel, M. A. Duguay, F. Lederer, and L. Leine, "Antiresonant waveguide add/drop filter using Fabry-Perot interference at 1.5 $\mu$m", *Proc. SPIE*, vol. 2402, pp. 2–8, 1995.

[97] M. Moreno, and J. Calderer, "Lateral photodetectors on ARROW structures for optical interconnections", *Opt. Commun.*, vol. 140, pp. 27–31, Jul. 1997.

[98] S. Asakawa, and Y. Kokubun, "ARROW-B type polarizer utilizing birefringence in multilayer stripe lateral confinement", *IEEE Photon. Technol. Lett.*, vol. 7, no. 1, pp. 39–40, Jan. 1995.

[99] T. Hayakawa, S. Asakawa, and Y. Kokubun, "ARROW-B type polarization splitter with asymmetric Y-branch fabricated by a self-alignment process", *J. Lightwave Technol.*, vol. 15, no. 7, pp. 1165–1170, Jul. 1997.

[100] J. Jehler, A. Bräuer, and W. Karthe, "Remote coupling over 93 $\mu$m using ARROW waveguides in strip configuration", *Electron. Lett.*, vol. 30, no. 3, pp. 218–220, Feb. 1994.

[101] T. Sekimoto, S. Ikuta, W. Pan, S. T. Chu, and Y. Kokubun, "Vertical antiresonant reflecting optical waveguide coupler for three-dimensional optical interconnects: optimum design for large tolerance, high coupling efficiency, and short coupling length", *Appl. Optics*, vol. 39, no. 3, pp. 426–430, Jan. 2000.

[102] K. A. Remley, and A. Weisshaar, "Design and analysis of a silicon-based antiresonant reflecting optical waveguide chemical sensor", *Opt. Lett.*, vol. 21, no. 16, pp. 1241–1243, Aug. 1996.

[103] H. Yang, M. Nesnidal, A. Al-Muhanna, L. J. Mawst, D. Botez, T. A. Vang, F. D. Alvarez, and R. Johnson, "High-power single-mode simplified antiresonant reflecting optical waveguide (S-ARROW) distributed feedback semiconductor lasers", *IEEE Photon. Technol. Lett.*, vol. 10, no. 8, pp. 1079–1081, Aug. 1998.

[104] W. Stutius, and W. Streifer, "Silicon-nitride films on silicon for optical waveguides", *Appl. Opt.*, vol. 16, no. 12, pp. 3218–3222, Dec. 1977.

[105] I. P. Kaminow, W. L. Mammel, and H. P. Weber, "Metal-clad optical waveguides: Analytical and experimental study", *Appl. Opt.*, vol. 11, no. 2, pp. 396–405, Feb. 1974.

[106] T. Miyamoto, and M. Momoda, "Propagation characteristics of a multilayered thin-film optical waveguide with a buffer layer", *J. Opt. Soc. Amer. A*, vol. 72, no. 9, pp. 1163–1166, Sep. 1982.

[107] E. Anemogiannis, E. N. Glytsis, and T. K. Gaylord, "Determination of guided and leaky modes in lossless and lossy planar multilayer optical waveguides: Reflection pole method and wavevector density method", *J. Lightwave Technol.*, vol. 17, no. 5, pp. 929–941, May 1999.

[108] J.-L. Archambault, R. J. Black, S. Lacroix, andJ. Bures, "Loss calculations for antiresonant waveguides", *J. Lightwave Technol.*, vol. 11, no. 3, pp. 416–423, Mar. 1993.

[109] H. J. Fink, "Propagation of waves in optical waveguides with various dielectric and metallic claddings", *IEEE J. Quantum Electron.*, vol. QE-12, no. 6, pp. 365–367, Jun. 1976.

[110] J. Chilwell, and I. Hodgkinson, "Thin-film field-transfer matrix theory of planar multilayer waveguides and reflection from prism-loaded waveguides", *J. Opt. Soc. Amer. A*, vol. 1, no. 7, pp. 742–753, Jul. 1984.

[111] X. Li, and R. T. Deck, "Light polarizar based on a antiresonant reflecting layers in a directional coupler", *Appl. Phys. Lett.*, vol. 66, no. 2, pp. 130–132, Jan. 1995.

[112] J. I. Garcés, PhD Thesis, "Estudio teórico y desarrollo experimental de guías de onda ópticas en tecnología de silicio: Aplicación al diseño de sensores optoquímicos", *Universidad de Zaragoza.*

[113] I. Garcés, F. Villuendas, J. A. Vallés, C. Domínguez, and M. Moreno, "Analysis of leakage properties and guiding conditions of rib antiresonant reflecting optical waveguides", *J. Lightwave Technol.*, vol. 14, no. 5, pp. 798–805, May 1996.

[114] I. Garcés, J. Subías, and R. Alonso, "Analysis of the modal solutions of rib antiresonant reflecting optical waveguides", *J. Lightwave Technol.*, vol. 17, no. 9, pp. 1566–1574, Sep. 1999.

[115] J. M. Kubica, "Numerical analysis of InP/InGaAsP ARROW waveguides using transfer matrix approach", *J. Lightwave Technol.*, vol. 10, no. 6, pp. 767–771, Jun. 1992.

[116] A. Bhattacharya, L. J. Mawst, M. P. Nesnidal, J. Lopez, and D. Botez, "High power narrow beam singlemode ARROW-type InGaAs/InGaAsP/InGaP diode lasers", *Electron. Lett.*, vol. 31, no. 21, pp. 1837–1838, Oct. 1995.

[117] G. R. Hadley, "Two-dimensional waveguide modeling of leaky-mode arrays", *Opt. Lett.*, vol. 14, no. 16, pp. 859–861, Aug. 1989.

[118] G. R. Hadley, "Index-guided arrays with a large index step", *Opt. Lett.*, vol. 14, no. 6, pp. 308–310, Mar. 1989.

[119] L. J. Mawst, D. Botez, C. Zmudzinski, and C. Tu, "0.3 W CW single-spatial-mode operation from large-core ARROW-type diode lasers", *Electron. Lett.*, vol. 28, no. 19, pp. 1793–1795, Sep. 1992.

[120] G. R. Hadley, "Two-dimensional coupled-mode theory for modeling leaky-mode arrays", *Opt. Lett.*, vol. 15, no. 1, pp. 27–29, Jan. 1990.

[121] B. M. A. Rahman, M. Rajarajan, T. Wongcharoen, and K. T. V. Grattan, "Improved laser-fiber coupling by using spot-size transformer", *IEEE Photon. Technol. Lett.*, vol. 8, no. 4, pp. 557–559, Apr. 1996.

[122] T. Wongcharoen, B. M. A. Rajarajan, and K. T. V. Grattan, "Spot-size conversion using uniform waveguide sections for efficient laser-fiber coupling", *J. Lightwave Technol.*, vol. 19, no. 5, pp. 708–716, May 2001.

[123] V. Vusirikala, S. S. Saini, R. E. Bartolo, M. Dagenais, and D. R. Stone, "Compact mode expanders using resonant coupling between a tapered active region and an underlying coupling waveguide", *IEEE Photon. Technol. Lett.*, vol. 19, no. 2, pp. 203–205, Feb. 1998.

[124] S. S. Saini, V. Vusirikala, R. Whaley, F. G. Johnson, D. Stone, and M. Dagenais, "Compact mode expanded lasers using resonant coupling between a 1.55-$\mu$m InGaAsP tapered active region and an underlying coupling waveguide", *IEEE Photon. Technol. Lett.*, vol. 10, no. 9, pp. 1232–1234, Sep. 1998.

[125] V. Vusirikala, PhD Thesis, "Semiconductor lasers for low loss alignment tolerant coupling to single mode optical fibers", *University of Maryland*, 1998.

[126] J.-J. Deng, and Y.-T. Huang, "Loss reduction of abrupt waveguide bends using Fabry-Perot cavity for optical interconnects", *Proc. SPIE*, vol. 3008, pp. 160–170, Apr. 1997.

[127] M. Heiblum, and J. H. Harris, "Analysis of curved optical waveguides by conformal transformation", *IEEE J. Quantum Electron.*, vol. QE-11, no. 2, pp. 75–83, Feb. 1975.

[128] R. Scarmozzino, A. Gopinath, R. Pregla, and S. Helfert, "Numerical techniques for modeling guided-wave photonic devices", *IEEE J. Select. Topics Quantum Electron.*, vol. 6, pp. 150–162, Jan./Feb. 2000.

[129] G. Sztefka, and H. P. Nolting, "Bidirectional eigenmode propagation for large refractive index steps", *IEEE Photon. Technol. Lett.*, vol. 5, pp. 554–557, May 1993.

[130] A. W. Snyder, and J. D. Love, *Optical Waveguide Theory. London*, U.K.: Chapman and Hall, 1983.

[131] S.-L. Lee, Y. Chung, L. A. Coldren, and N. Dagli, "On leaky mode approximations for modal expansion in multilayer open waveguides", *J. Quantum Electron.*, vol. 31, no. 10, pp. 1790–1802, Oct. 1995.

[132] P. Bienstman, PhD Thesis, "Rigorous and efficient modelling of wavelength scale photonic components", *University of Gent*, 2001.

[133] P. Bienstman, and R. Baets, "Advanced boundary conditions for eigenmode expansion models", *Opt. Quantum Electron.*, accepted for publication.

[134] J.-P. Bérenger, "A perfectly matched layer for the absorption of electromagnetic waves", *J. Comput. Phys.*, vol. 114, no. 1, pp. 185–200, 1994.

# Publications

## Publication A

# Modeling of InGaAsP-InP 1.55 $\mu$m Lasers with Integrated Mode Expanders Using Fiber-Matched Leaky Waveguides

M. Galarza, K. De Mesel, D. Fuentes, R. Baets, and M. López-Amo

*Applied Physics B–Lasers and Optics*, vol. 73, no. 5–6, pp. 585–588, Oct. 2002.

***Abstract***—A new concept for InGaAsP-InP 1.55 $\mu$m lasers integrated with spot size converters using leaky waveguides is presented. The large fundamental mode size and the high discrimination of the higher order modes make ARROW's (Antiresonant Reflecting Optical Waveguide) and antiguided waveguides useful for fiber coupling functions. Three-dimensional (3-D) beam propagation method (BPM) results show that the devices have transformation losses lower than 0.22 dB. Fiber-coupling efficiencies of 60 % are possible to standard cleaved single-mode fibers (SMF). The horizontal and vertical FWHM can be efficiently reduced to 9.7° (horizontal) and 17.8° (vertical). The fabrication of such devices avoids the growth of thick layers of quaternary material with a low Ga and As fraction and simplifies the fabrication to one planar epitaxial growth step and one non-critical conventional etch.

## A.1 Introduction

The packaging of optoelectronic integrated semiconductor circuits amounts up to about 80 % of the cost of the final module. This fact is one of the largest barriers to future mass production needs. Highly-efficient chip-to-fiber coupling with large alignment tolerances is a critical requirement to obtain low-cost optoelectronic devices. The problem arises because of the mode mismatch between the semiconductor waveguide and the optical fiber. The former has typically a 1-2 $\mu$m elliptical modal spot, which is neither well-sized nor shaped to match the standard 8-9 $\mu$m circular modal spot of conventional single-mode optical fibers. Directly butt-coupled devices present 7-10 dB insertion loss and submicron alignment tolerances. Nonintegrated solutions improve this coupling but not the alignment requirements. To achieve both low coupling loss and large alignment tolerances it is necessary to transform the mode on-chip to better match the fiber.

Over the past years, various integrated mode transformers have been proposed [1]. Most of these approaches involve complex growth and/or processing steps, requiring extensive process development. Nevertheless, there is an at-

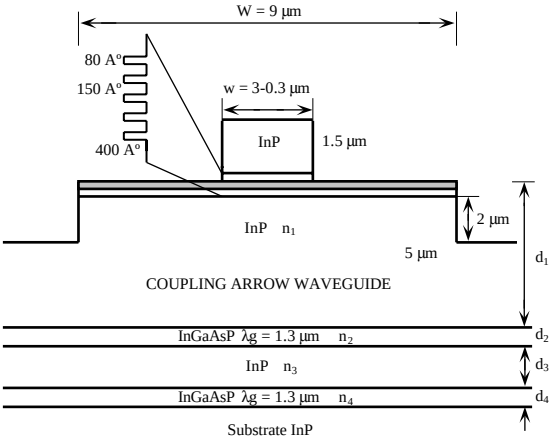


Figure A.1: Schematic drawing of the adiabatic mode expanded laser showing the tapered upper active rib and the underlying fiber-matched ARROW waveguide.

tractive group of devices that uses a single standard planar epitaxial growth step and conventional processing techniques [2, 3]. These devices need a large rib waveguide that operates close to cut-off. In InP technology this involves the growth of quaternary materials exhibiting a slightly higher refractive index than the substrate of InP. These low refractive indexes are achieved by means of low Ga and As fraction quaternary materials, which are difficult to achieve and grow. This problem was solved in [2], by introducing a diluted structure. In the present work, we propose a 1.55 $\mu$m laser integrated with a spot size converter based on lateral tapering of the laser rib waveguide to adiabatically transform its mode to the fundamental mode of an underlying fiber-matched vertical-ARROW [4] rib waveguide. The quasiguided ARROW-modes exhibit very attractive features for a fiber coupling function [4]: large mode sizes, low losses for the fundamental mode, high discrimination of the higher order modes, and ease of fabrication owing to its high tolerances and to the fact that the thick core consists of InP. Moreover, the wavelength and polarization dependence of such waveguides is negligible. In the final section of this paper, the use of the ARROW effect for both vertical and lateral confinement of the output mode is described in the design of a second device. This simplifies the processing of the device drastically.

## A.2 Waveguide Design

The transverse structure of the proposed laser is shown in Fig. A.1. It consists of an active waveguide and an underlying passive rib ARROW waveguide optimized for coupling to an optical fiber. As the active waveguide is tapered by reducing the ridge width, the mode couples adiabatically from the upper guide (Fig. A.2a)

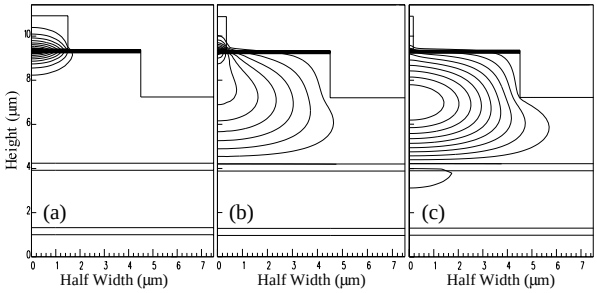


Figure A.2: Fundamental TE mode for (a) $w = 3$ $\mu$m, (b) $w = 0.7$ $\mu$m and (c) $w = 0.3$ $\mu$m.

to the underlying passive ARROW waveguide (Fig. A.2c). The active layer consists of five 1 % compressively strained 80 Å-thick $In_{0.78}Ga_{0.22}As_{0.79}P_{0.21}$ quantum wells for emission at 1.55 $\mu$m, and four lattice-matched 150 Å-thick $In_{0.75}Ga_{0.25}As_{0.54}P_{0.46}$ barriers, surrounded by 400 Å-thick SCH regions. For this active region, an equivalent index of 3.42 was computed. The vertical confinement in the lower large guide is provided by an ARROW-structure for which the optimum thickness of its three cladding layers ($d_2$, $d_3$, $d_4$) is given by the following approximate antiresonance conditions [4]:

$$d_{2,4} = \frac{\lambda}{4n_{2,4}} \left( 1 - \left( \frac{n_1}{n_{2,4}} \right)^2 + \left( \frac{\lambda}{2n_{2,4} d_{ce}} \right)^2 \right)^{-1/2} \cdot (2M + 1) \qquad \text{(A.1)}$$

$$d_3 = \frac{d_{ce}}{2}(2N + 1) \qquad (M, N = 0, 1, 2, \ldots)$$

where $\lambda$ is the vacuum wavelength; $n_1$, $n_2$, $n_4$ the refractive index of the ARROW InP core, the first cladding layer and the third, respectively; $d_{ce}$ is the equivalent core thickness, which involves the Goos-Hänchen shift at the top of the ARROW core and is defined as:

$$d_{ce} = d_1 + \zeta \frac{\lambda}{2\pi\sqrt{n_1^2 - n_0^2}}, \qquad \text{(A.2)}$$

where

$$\zeta = \begin{cases} 1, & \text{for TE modes;} \\ (n_0/n_1)^2 & \text{for TM modes.} \end{cases} \qquad \text{(A.3)}$$

In the above expressions $n_{co}$ denotes the refractive index of the active core and $n_0$ the refractive index of the polyimide that covers the device. We choose a quaternary compound with $\lambda_g = 1.3$ $\mu$m for the two high refractive index ARROW layers. The calculated values of the cladding layer thickness for TE polarization are: $d_{2,4} = 0.32$ $\mu$m and $d_3 = 2.6$ $\mu$m.

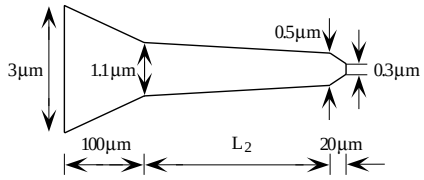


Figure A.3: The optimum taper shape is approximated by a piecewise linear device consisting of three linear sections. The length of the central section depends on the transversal structure.

## A.3 Device Design and Simulation Results

A commercial 3-D eigenmode expansion algorithm (Fimmprop-3D) [5] was used to study the modal behavior of the tapered device and find the critical width where the mode transformation takes place. To get this information, an extremely short (1 $\mu$m long) and linearly tapered device from $w_i = 3$ $\mu$m to $w_f = 0.3$ $\mu$m was simulated and the evolution of the power of the fundamental mode recorded and plotted versus the width of the active waveguide. A flat response was obtained for large and narrow widths, which results from the mode shape changing only slightly in this section of the taper. The critical change of the modal shape and the whole radiation is produced in the 1.1 to 0.5 $\mu$m range, where low taper angles will be needed to obtain an adiabatic mode transformation. The optimum taper was approximated by a piecewise linear device consisting of three linear sections as shown in Fig. A.3. The central section length $L_2$ is 450 $\mu$m to ensure an adiabatic mode transformation. The overall length is 570 $\mu$m. The mode transformation is completed before the rib width reaches 0.3 $\mu$m, which can be certainly considered a minimum value for the photolithography of thin ridges.

Fimmprop-3D [5] uses hard boundary conditions and hence, leakage power cannot radiate out of the calculation window. Beam propagation method (BPM), on the other hand, allows working with transparent boundary conditions, so that light can radiate out of the simulation window. We employed a commercial 3-D BPM [6] to simulate the designed device. Mesh discretizations of 0.01 and 0.05 $\mu$m were used in the horizontal and vertical directions, respectively. A longitudinal step of 0.2 $\mu$m and semivectorial (TE) calculations were used for propagation. Input and output near field power distributions are shown in Fig. A.4. Total transformation losses of 0.18 dB were obtained. By performing a complex overlap integral with the optical mode of a standard SMF, butt-coupling efficiencies of 58 % are estimated. The improvement in the coupling introduced by the taper reaches 5.9 dB. FWHM divergence angles of 9.8° (horizontal) × 23.1° (vertical) were found.

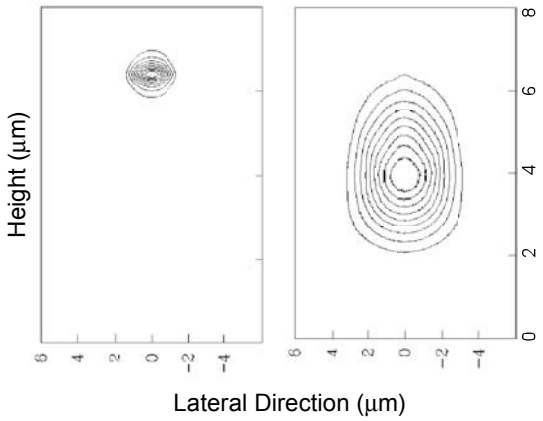


Figure A.4: Intensity plots of (a) the upper active rib mode and (b) the output expanded TE field at the end of the optimum taper.

### A.3.1 Reduction of the Thickness of the ARROW Cladding Layers

Equation (A.1) provides the thickness of the cladding layers that minimize the leaky losses of the fundamental ARROW modegiven a core thickness $d_1$ and a refractive index $n_{2,4}$ for the high index layers. In the case designed above, the total cladding thickness is 3.24 $\mu$m, which is an unattractive value from a growth point of view. The growth of such a thick set of layers beneath the broad core increases the fabrication time and can cause instabilities in the growth process. The leaky loss of the fundamental mode calculated by means of the well known transfer matrix method (TMM) for the optimum cladding, is 0.25 dB/cm. This value is negligible compared to the total transformation loss of the mode expander calculated above, because the ARROW mode of the taper propagates along lengths shorter than a few hundred of microns. A higher leakage loss, in the order of the transformation loss, would still be acceptable. This means that moving away from the anti-resonance condition and hence increasing the radiation loss offers the possibility to reduce the ARROW cladding layer thickness and lessen the above mentioned growth difficulties without changing the taper behavior.

We have considered a maximum propagation length of the ARROW mode in the taper of 300 $\mu$m and allowed a total leaky loss of 0.1 dB. This means that the new ARROW claddings can present a leaky loss as high as 3 dB/cm. Using TMM the losses of different combinations of $d_2$, $d_3$ and $d_4$ have been calculated (see Fig. A.5). The structure presenting the lower thickness for a leaky loss of 3 dB/cm is chosen: $d_{2,4} = 0.31$ $\mu$m, $d_3 = 0.5$ $\mu$m. The total cladding thickness is reduced to 1.12 $\mu$m (2.12 $\mu$m less than the previous case!).

The expanded output mode of the taper after BPM propagation using the

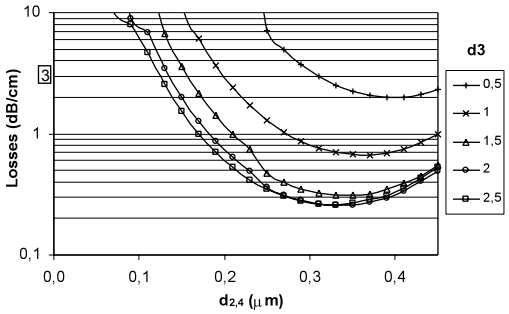


Figure A.5: Attenuation of the fundamental TE ARROW mode as a function of the thickness of the three cladding layers $d_2 = d_4$ and $d_3$.

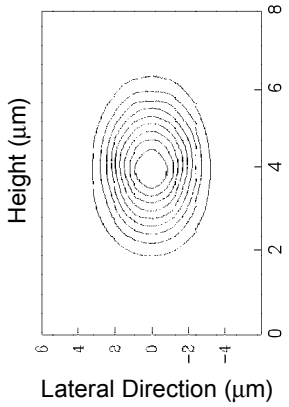


Figure A.6: Intensity plot of the mode at the output of the optimum taper that uses the relaxed vertical ARROW claddings.

relaxed new structure is shown in Fig. A.6. We observe that the field does not change and that the thinner cladding doesn't cause any significant leakage towards the substrate. The device characteristics do not change significantly compared to the unrelaxed design. The total transformation and leaky loss are 0.22 dB, slightly higher than before. The coupling efficiency to a standard SMF is 60 %. And the vertical FWHM divergence angle is somewhat improved: 9.7° (horizontal) × 17.8° (vertical).

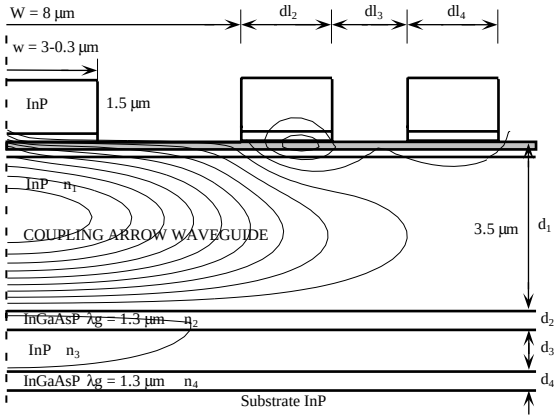


Figure A.7: Cross-section diagram of the device that uses the ARROW effect for the lateral and vertical confinement. The contour plot of the supported leaky mode is shown.

## A.4 Vertical + Lateral ARROW Confinement

The ARROW effect can be used, not only for the vertical confinement but even in the lateral confinement of the output fiber-matched mode. The objective of this new device is to drastically simplify the fabrication process eliminating the second etch step in which the rib of the broad underlying waveguide is defined. The alignment of this second mask is the most critical feature of this kind of device.

In Fig. A.7 half of the cross-section of the proposed laser is shown. The active layer and lower ARROW cladding materials are the same as in the first device. The ribs at both sides of the central guide will perform the lateral confinement in a similar way as the cladding layers of the conventional vertical ARROW guides. The lower core thickness is reduced to 3.5 $\mu$m because the lateral ARROW-ribs do not confine the modes of thicker layers efficiently. From (A.1)–(A.3), $d_{2,4} = 0.32$ $\mu$m and $d_3 = 1.86$ $\mu$m. The design of the ribs differs from that employed for the vertical ARROW due to the guided modes of every rib guide. In [7] the authors extend the use of the effective index method (EIM) to regions supporting more than one guided mode. And in [8] a quantitative design rule for antiguided arrays was presented that could be used to design the output mode: the confinement of the light in the lower waveguide will be maximum when the propagation constant of the second-order rib mode matches that of the fundamental mode of the underlying slab waveguide. In our case this second-order mode is in cut-off. Therefore, a study of the confinement of the output mode in the upper active layer in function of the width of the lateral ribs ($dl_2$, $dl_3$) was done, and the minimum was obtained for $dl_{2,4} = 1.5$ $\mu$m and $dl_3 < 1$ $\mu$m; nevertheless $dl_3$ had to be increased to 1 $\mu$m because of fabrication tolerances. We used the Fimmprop3D software to calculate the mode of the

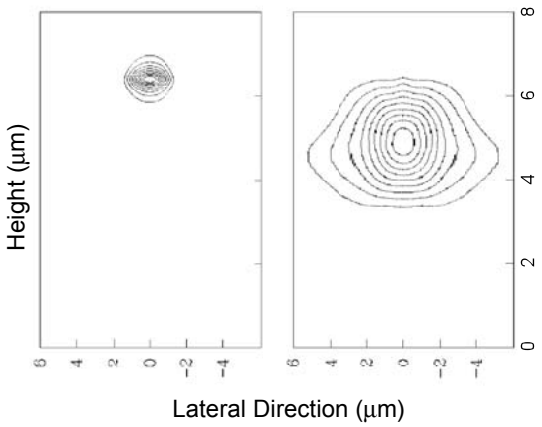


Figure A.8: Intensity plots of (a) the upper active rib mode and (b) the output expanded TE field at the end of the optimum taper that uses lateral and vertical ARROW effects for confinement.

structure. The result is shown in Fig. A.7. The design of the shape of the taper was done following the steps explained in the design of the first device. The power fraction of the fundamental mode in the 1 $\mu$m long linear taper was calculated. The critical range of the upper width is the same as in the previous taper: 1.1–0.5 $\mu$m. The length of the central section $L_2$ was selected to be 300 $\mu$m for an overall length of 420 $\mu$m. The laser was simulated with BPM to take into account the vertical and lateral leakage of the fiber-matched mode. Input and output near field intensity distributions are shown in Fig. A.8. Total transformation and leaky losses of 0.13 dB were obtained. Butt-coupling efficiencies of 43 % to a standard SMF were estimated. The improvement in the fiber-coupling reached 4.6 dB. FWHM divergence angles of 8.8° (horizontal) × 36.5° (vertical) were observed.

### A.4.1 Reduction of the vertical ARROW cladding thickness

We have followed the same vertical ARROW cladding reduction criterion as discussed in Sect. A.3 to reduce the 2.5 $\mu$m cladding thickness of this second device. The minimum leaky loss of the optimum structure is higher now than before because of the thinner core layer $d_1$ [4]. Therefore, we choose a higher refractive index for the first and the third ARROW layers to obtain a better efficiency in the thickness reduction. A quaternary compound with $\lambda_g = 1.45$ $\mu$m was selected with a refractive index of 3.46. The results provide the following new structure: $d_{2,4} = 0.22$ $\mu$m, $d_3 = 1$ $\mu$m. This means an initial growth of 1.44 $\mu$m instead of the 2.5 $\mu$m of the optimum ARROW.

The near field intensity distribution of the fiber-matched mode provided by

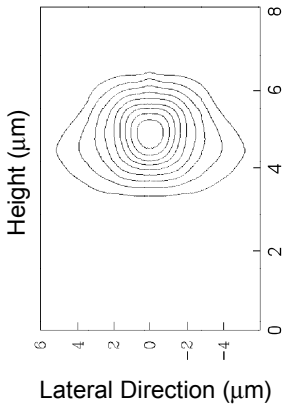


Figure A.9: Intensity plot of the mode at the output of the taper of Fig. A.7 that uses the relaxed vertical ARROW claddings.

the BPM propagation using the relaxed ARROW claddings is shown in Fig. A.9. The total transformation loss is 0.15 dB. The coupling to the standard fiber is 43 %, the same as before and the far field divergence angles are slightly improved to 7.6° (horizontal) × 35° (vertical).

## A.5 Conclusions

In this work, we have presented results on mode-expanded lasers based on the adiabatic transformation of the laser rib mode into a fiber-matched ARROW waveguide. The confinement of the expanded field in the large InP core of the ARROW guide facilitates the fabrication. The application of the ARROW effect to the lateral confinement of the output broad mode eliminates the need for the second processing, drastically simplifying the fabrication of the device. Efficient mode transformation and significant fiber coupling improvements can be achieved.

## References

[1] I. Moerman, P. P. Van Daele, P. M. Demeester: IEEE J. Select. Topics Quantum Electron. **3**, 1308 (1997)

[2] V. Vusirikala, S. S. Saini, R. E. Bartolo, S. Agarwala, R. D. Whaley, F. G. Johnson, D. R. Stone, M. Dagenais: IEEE J. Select. Topics Quantum Electron. **3**, 1332 (1997)

[3] K. De Mesel, R. Baets, C. Sys, S. Verstuyft, I. Moerman, P. Van Daele: Electron. Lett. **36**, 1028 (2000)

[4] J. M. Kubica: IEEE J. Lightwave Technol. **10**,767 (1992)

[5] Fimmprop-3D propagation tool from Photon Design; `http://www.photond.com`

[6] BPM_CAD, Optiwave corporation; `http://www.optiwave.com`

[7] P. Yeh, C. Gu, D. Botez: J. Opt. Soc. Am. B **10**, 709 (1993)

[8] G. R. Hadley: Opt. Lett. **15**, 27 (1990)

## Publication B

# 1.55-$\mu$m InP–InGaAsP Fabry-Pérot Lasers with Integrated Spot Size Converters using Antiresonant Reflecting Optical Waveguides

M. Galarza, K. De Mesel, S. Verstuyft, C. Aramburu, I. Moerman, P. Van Daele, R. Baets, and M. López-Amo

*IEEE Photonics Technology Letters*, vol. 14, no. 8, pp. 1043–1045, Aug. 2002.

***Abstract***—We demonstrate a new concept for InGaAsP–InP 1.55 $\mu$m Fabry-Pérot lasers integrated with spot size converters using type-A antiresonant reflecting optical waveguides (ARROW). The fabrication of such devices allows to avoid the growth of thick layers of quaternary material with low Ga and As fraction, which are difficult to achieve and grow. Reduced far-field divergence angles ($10^\circ \times 27^\circ$) and improved coupling to cleaved standard single-mode fibers (2.6-dB coupling loss) are achieved. The proposed device is compatible with conventional epitaxial techniques and lithographic methods.

## B.1 Introduction

The major part of the cost of an optical module comes from the packaging. This fact is one of the largest barriers to future mass production needs in optical communication systems. Highly-efficient chip-to-fiber coupling with large alignment tolerances is very important for low-loss integrated optics. The problem arises from the large mismatch between the large circular mode in the fiber and the small asymmetric mode in a III-V semiconductor waveguide component, leading to high coupling losses. Over the past years much research has focused on the integration of mode size converters with waveguide components in order to improve the coupling efficiency [1], [2]. Most of these approaches involve complex growth and/or processing steps, requiring extensive process development [3]. Nevertheless, there is a group of devices requiring only a single standard planar epitaxial growth step and conventional processing techniques that has attracted considerable attention [4]–[6]. These devices incorporate a large fiber-adapted rib waveguide that operates close to cut-off. In InP technology this involves the growth of quaternary materials exhibiting a slightly higher refractive index than the InP substrate. These low refractive indexes are achieved by means of low Ga- and As-fraction quaternary materials, which are difficult to achieve and grow. One solution is the use of diluted structures. The new taper concept presented

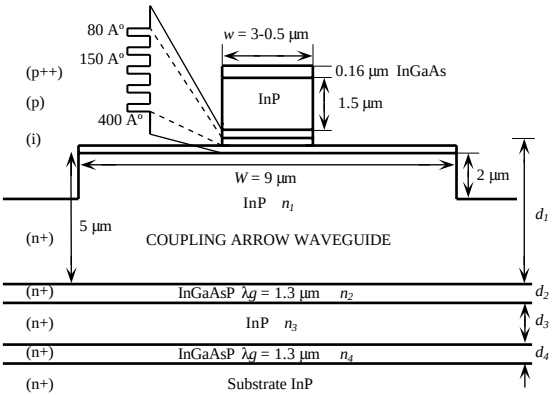


(a)

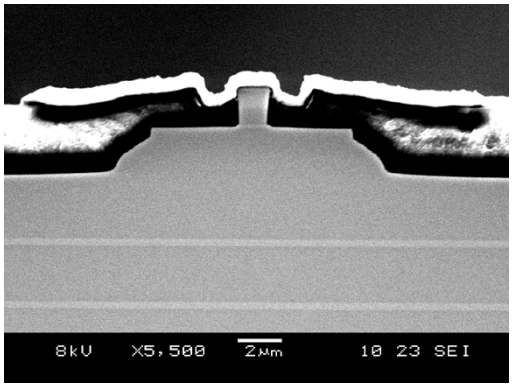


(b)

Figure B.1: Cross section of the mode expanded laser. (a) Schematic drawing, and (b) SEM photograph.

in this work is based on the use of type-A ARROW waveguides [7] and forms an alternative solution to this problem. The design, fabrication and performance of the new device are discussed.

## B.2 Device Design and Fabrication

The transverse structure of the proposed laser is shown in Fig. B.1. The device is grown by MOCVD and consists of an active waveguide, which is placed on top of a large passive ridge that is optimized for coupling to an optical fiber. The

vertical optical confinement in this passive guide is realized by a type-A ARROW structure. The quasiguided ARROW-modes exhibit very attractive features for a fiber coupling function: large mode sizes, low losses for the fundamental mode, high discrimination of the higher order modes, and ease of fabrication owing to its high tolerances and to the fact that the thick core consists of InP. Moreover, the wavelength and polarization dependence of such waveguides is negligible. The optimum thickness of the three ARROW cladding layers ($d_2$, $d_3$, $d_4$) is given by the following approximate anti-resonance conditions [8]:

$$d_{2,4} = \frac{\lambda}{4n_{2,4}} \left( 1 - \left( \frac{n_1}{n_{2,4}} \right)^2 + \left( \frac{\lambda}{2n_{2,4}d_{ce}} \right)^2 \right)^{-1/2} \cdot (2M+1) \qquad \text{(B.1)}$$

$$d_3 = \frac{d_{ce}}{2}(2N+1) \qquad (M, N = 0, 1, 2, \ldots)$$

where $\lambda$ is the vacuum wavelength; $n_1$, $n_2$, $n_4$ the refractive index of the ARROW InP core, the first cladding layer and the third, respectively; $d_{ce}$ is the equivalent core thickness, which involves the Goos-Hänchen shift at the top of the ARROW core and is defined as

$$d_{ce} = d_1 + \zeta \frac{\lambda}{2\pi\sqrt{n_1^2 - n_0^2}}, \qquad \text{(B.2)}$$

where

$$\zeta = \begin{cases} 1, & \text{for TE modes;} \\ (n_0/n_1)^2 & \text{for TM modes.} \end{cases} \qquad \text{(B.3)}$$

In the above expressions $n_{co}$ denotes the refractive index of the active core and $n_0$ the refractive index of the polyimide that covers the device. We choose a quaternary compound with $\lambda_g = 1.3$ $\mu$m for the two high refractive index ARROW layers. The calculated values of the cladding layer thickness for TE polarization are: $d_{2,4} = 0.32$ $\mu$m and $d_3 = 2.6$ $\mu$m.

The multiple quantum-well (MQW) contains five 1 % compressively strained 80 Å-thick $In_{0.78}Ga_{0.22}As_{0.79}P_{0.21}$ wells for emission at 1.55 $\mu$m, and four lattice-matched 150 Å-thick $In_{0.75}Ga_{0.25}As_{0.54}P_{0.46}$ barriers, surrounded by 400 Å-thick undoped confining layers having the same composition of the barriers. The metallization covers the spot size converters over their entire length. This can have a negative impact on the threshold current and efficiency, but on the other hand it avoids the risk of high absorption losses in the passive section of the taper.

As the active waveguide is tapered by reducing the ridge width, from 3 to 0.5 $\mu$m, the mode couples adiabatically from the upper guide to the underlying ARROW waveguide (see Fig. B.2). The design of the lateral tapering is based on the adiabaticity of the mode transformation, and has been evaluated by means of a commercial three-dimensional (3-D) eigenmode expansion algorithm based on a resonance method [9]. The critical change of the modal shape and the whole radiation is produced in the 1.18 to 0.8 $\mu$m range, where low taper angles will be needed to obtain an adiabatic mode transformation. The taper shape was approximated by a 370 $\mu$m-long-piecewise linear device consisting of three linear

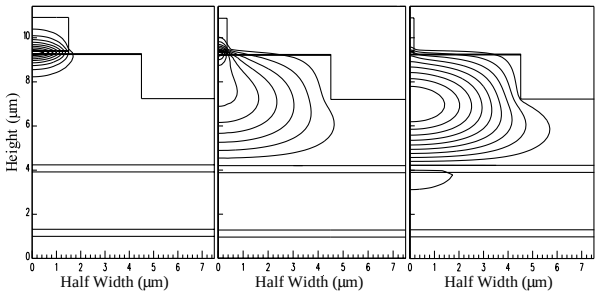


Figure B.2: The fundamental TE mode for (a) $w = 3$ $\mu$m, (b) $w = 0.9$ $\mu$m and (c) $w = 0.5$ $\mu$m.

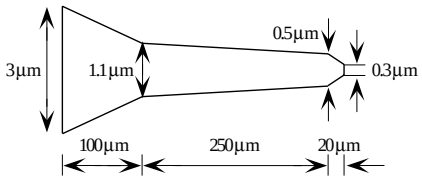


Figure B.3: The optimum taper shape is approximated by a piecewise linear device consisting of three linear sections.

sections as shown in Fig. B.3, and exhibits a calculated transformation loss of 1 dB.

## B.3 Device Results

The devices were operated in CW mode. Fig. B.4 shows the light versus current ($L$–$I$) characteristics of 4 expanded mode devices and a control sample without any tapers. Untapered 750 $\mu$m long and 3 $\mu$m wide reference lasers exhibit typical threshold currents $I_{th}$ of 30 $\mu$m and a external efficiency of 0.13 W/A, while the expanded mode devices consisting of a 500-$\mu$m long gain section and a 370-$\mu$m long taper, show a threshold current around 50 mA with an external efficiency of 0.15 W/A. The increase in the threshold current of the expanded-mode lasers, as compared to the reference samples, can be attributed to the radiated power in the beam transformation region, to the losses in the $n$-doped thick InP layer, and to the non-uniform pumping of the tapered active rib as a function of its width. The decrease of the tapered facet reflectivity makes the external efficiency to increase slightly.

The far field emission patterns for both the tapered laser and the control samples were measured by using a rotating stage and a pinhole detector (see Fig. B.5). The theoretical curves obtained from the Fourier transform of the theoretical near fields are also overlaid in Fig. B.5, for comparison. A far field

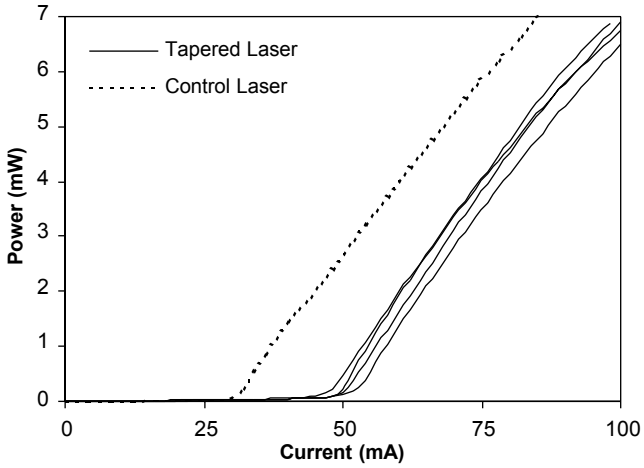


Figure B.4: $L$–$I$ characteristics of several mode expanded lasers compared to a control laser without any taper.

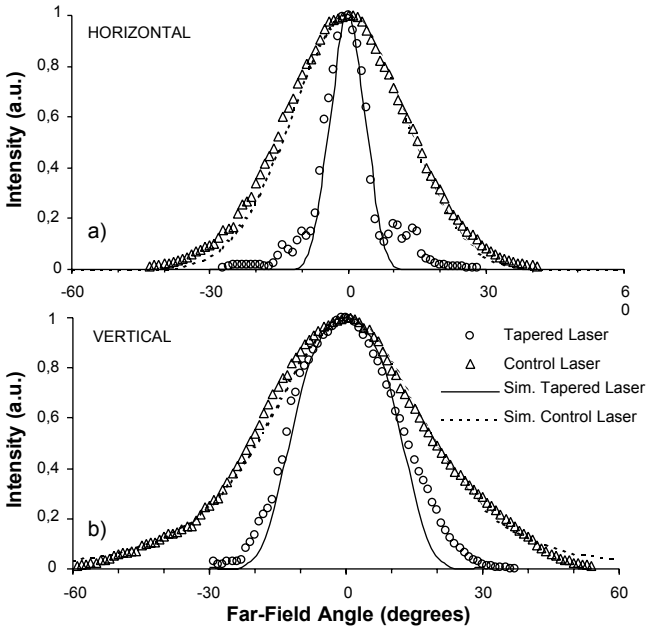


Figure B.5: Far-field emission patterns of tapered and untapered lasers: (a) Lateral direction. (b) Transverse direction.

divergence angle (FWHM) of $10° \times 27°$ was obtained in lateral and vertical directions for the mode expanded laser while the untapered devices exhibited $30.1° \times 40.1°$, in good agreement with theoretical calculations.

A coupling efficiency measurement was performed between the expanded mode laser and a standard cleaved SMF with a spot size of 10 $\mu$m at 1.55 $\mu$m. A maximum coupling efficiency of 55 % (2.6-dB loss) was obtained (this includes the Fresnel losses occurring at the air-glass interface). The improvement in the fiber coupling with respect to the untapered lasers reaches 5.8 dB. The measured 1-dB alignment tolerance range is 4.4 $\mu$m in lateral direction and 4.5 $\mu$m in transverse direction.

## B.4 Conclusion

We have realized a new laser emitting at 1.55 $\mu$m wavelength integrated with a spot size converter using a type-A ARROW waveguide for enhanced fiber coupling. The confinement of the expanded field in the large InP core of the ARROW waveguide facilitates the fabrication because it allows to avoid the growth of low Ga- and As-fraction quaternary materials. Efficient mode transformation and considerable reduction of the horizontal and vertical far-field have been achieved.

## References

[1] J. E. Johnson *et al.*, "Monolithically integrated semiconductor optical amplifier and electroabsorption modulator with dual-waveguide spot-size converter input," *IEEE J. Select. Topics Quantum Electron.*, vol. 6, pp. 19–25, Jan. 2000.

[2] J. R. Kim, J. S. Lee, S. Park, M. W. Park, J. S. Yu, S. D. Lee, A. G. Choo, T. I. Kim, and Y. H. Lee, "pot-size converter integrated polarization insensitive semiconductor optical amplifiers," *IEEE Photon. Technol. Lett.*, vol. 11, pp. 967–969, Aug. 1999.

[3] I. Moerman, P. Van Daele, and P. M. Demeester, "A review on fabrication technologies for the monolithic integration of tapers with III-V semiconductor devices," *IEEE J. Select. Topics Quantum Electron.*, vol. 3, pp. 1308–1320, Dec. 1997.

[4] S. S. Saini, F. G. Johnson, D. R. Stone, H. Shen, W. Zhou, and M. Dagenais, "Passive active resonant coupler (PARC) platform with mode expander," *IEEE Photon. Technol. Lett.*, vol. 12, pp. 1025–1027, Aug. 2000.

[5] G. A. Vawter, R. E. Smith, H. Hou, and J. R. Wendt, "Semiconductor laser with tapered-rib adiabatic-following fiber coupler for expanded output-mode diameter," *IEEE Photon. Technol. Lett.*, vol. 9, pp. 425–427, Apr. 1997.

[6] K. De Mesel, R. Baets, C. Sys, S. Verstuyft, I. Moerman, and P. Van Daele, "First demonstration of 980 nm oxide confined laser with integrated spot size converter," *Electron. Lett.*, vol. 36, pp. 1028–1029, Jun. 2000.

[7] R. A. Soref, and K. J. Ritter, "Silicon antiresonant reflecting optical waveguides," *Opt. Lett.*, vol. 15, pp. 792–794, Jul. 1990.

[8] J. M. Kubica, "Numerical analysis of InP/InGaAsP ARROW waveguides using transfer matrix approach," *IEEE J. Lightwave Technol.*, vol. 10, pp. 767–771, Jun. 1992.

[9] A. S. Sudbo, "Numerically stable formulation of the transverse resonance method for mode-field calculations in dielectric waveguides," *IEEE Photon. Technol. Lett.*, vol. 5, pp. 342–344, Mar. 1993.

## Publication C

# Mode-Expanded 1.55 $\mu$m InP–InGaAsP Fabry-Pérot Lasers Using ARROW Waveguides for Efficient Fiber Coupling

M. Galarza, K. De Mesel, S. Verstuyft, D. Fuentes, C. Aramburu, M. López-Amo, I. Moerman, P. Van Daele, and R. Baets

*IEEE Journal of Selected Topics in Quantum Electronics*, Accepted for publication, Nov./Dec. 2002.

***Abstract***—We report on a new concept for InGaAsP–InP 1.55 $\mu$m lasers with integrated spot-size converters based on antiresonant reflecting optical waveguides (ARROW's). The mode expanders consist of a tapered active region on top of a fiber-matched passive vertical ARROW waveguide. The large fundamental leaky mode with its low propagation loss makes ARROW waveguides useful for fiber coupling functions and avoids typical growth-related problems as encountered with traditional designs. The tapers exhibit a low transformation loss, narrowed far-field emission patterns ($10.4° \times 22°$) and reduce the coupling loss to standard single-mode fibers from 8 dB to 2.6 dB. We also present the design and the results obtained with a relaxed ARROW-design with thinner ARROW-layers to reduce the overall layer stack thickness considerably, without affecting the fiber-coupling performance.

The antiresonant effect has also been used for the lateral confinement of the fiber-matched mode. This feature makes the presented spot-size transformer as simple to fabricate as a standard waveguide, only requiring a planar growth step and a single conventional etch process. The fabricated tapers exhibit a low transformation loss and minimum far-field divergence angles of $13.8° \times 30.8°$, reducing the coupling loss to a standard single-mode fiber from 8 to 4 dB.

We also analyze by simulation two variants of the concept proposed in this work, including a taper structure for a buried waveguide, which are expected to show better performance. Simulation results show fiber-coupling efficiencies as low as 2.4 and 1.1 dB, and reduced far-field divergence angles as low as $7.2° \times 14°$ and $7.2° \times 9°$ for both variants.

## C.1 Introduction

There exist two rationales for the use of integrated spot-size converters (SSC) in the development of low-cost opto-electronic devices. One is the pigtailing or fiber attachment of III-V semiconductor photonic integrated circuits (PIC),

mostly active devices containing lasers or semiconductor optical amplifiers. The other is the integration of such PIC's with silica-on-silicon waveguides for the development of hybrid devices.

The typical refractive index difference $\Delta n$ in a semiconductor waveguide is generally larger than $1 \times 10^{-1}$, leading to mode sizes smaller than 2 $\mu$m. Besides, due to the planar technology used in the fabrication of semiconductor waveguides, the mode shape is highly asymmetric. The very small refractive index difference in a single mode glass fiber or silica waveguide ($\Delta n < 5 \times 10^{-3}$), on the other hand, results in a weakly guided circular mode with a typical mode size of 8–10 $\mu$m. Direct butt-coupling between an opto-electronic device and a fiber causes typically 7-10 dB loss.

The function of an integrated SSC's is to enlarge and reshape the small and asymmetric mode of the III-V semiconductor waveguide component to a large and circular mode that is better adapted to the fiber or silica waveguide [1]. In this way, it provides high coupling efficiencies and large alignment tolerances that enable the use of passive alignment schemes that drastically reduce the packaging cost. The use of microlenses or tapered/lensed fibers [2] that image one mode onto the other is an alternate solution that also improves the coupling loss, but at the expense of the alignment tolerances, which are then in the submicron range.

Over the past ten years much research has focused on the integration of mode size converters with waveguide components in order to improve the coupling efficiency [3], [4]. Most of these approaches involve complex growth and/or processing steps, requiring extensive process development. Nevertheless, there is one group of devices that is particularly interesting since it only requires a single standard planar epitaxial growth step and conventional lithography and etching processes [5]–[7]. These devices incorporate a large fiber-matched rib waveguide that operates close to cutoff. In InP technology this involves the growth of quaternary materials exhibiting a slightly higher refractive index than the InP-substrate. These low-refractive indexes are achieved by means of low Ga- and As-fraction quaternary materials, which are difficult to grow. This problem was solved in [8], by introducing a diluted structure.

We have demonstrated an alternative solution in recent work [9], where the thick quaternary layer is replaced by an easy-to-grow InP layer in an ARROW configuration [10], [11]. In the tapered 1.55 $\mu$m laser presented in [9], a laser rib is laterally tapered so that its guided mode is adiabatically transformed into the fundamental mode of the underlying fiber-matched ARROW waveguide. The quasiguided ARROW-modes exhibit very attractive features for a fiber (or silica waveguide) coupling function: large mode sizes, low losses for the fundamental mode, and low polarization and wavelength dependence. Moreover, ARROW waveguides are easy to fabricate owing to their high tolerances and to the fact that the thick core consists of InP. We have also reported work on variants of this structure both in terms of theoretical predictions [12], as well as preliminary experimental results [13].

In this paper we present a structured overview of the performance of ARROW waveguide based tapers, whereby we present new results and a better

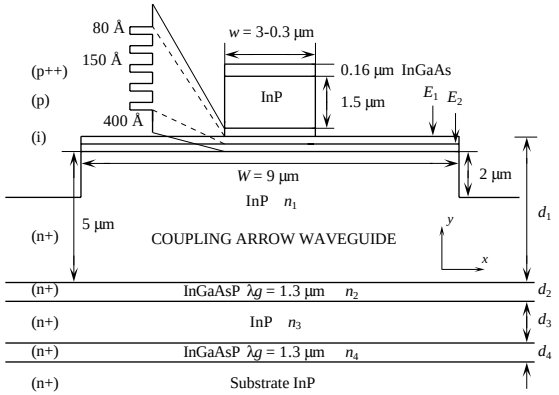


Figure C.1: Schematic drawing of the adiabatic mode-expanded laser showing the tapered upper active rib and the underlying fiber-matched ARROW waveguide.

understanding of the potential of this new technique. Section C.2 of this paper presents the theory, design and new results on mode-expanded lasers using fiber-matched vertical-ARROW waveguides. Section C.3 demonstrates new relaxed ARROW structures that reduce the overall layer stack thickness significantly without affecting the fiber coupling characteristics. In Section C.4 the ARROW effect is used for both vertical and lateral confinement of the output fiber-matched mode, leading to a fabrication scheme for the mode-expanded laser that does not require extra processing steps to integrate the taper. Also two interesting variants of this concept are proposed and analyzed by simulation. Section C.5 finally summarizes and concludes this work.

## C.2 Mode expanded Lasers Using Vertical ARROW Confinement

### C.2.1 Device Design and Theory

The transverse structure of the proposed mode-expanded laser is shown in Fig. C.1. The device consists of an active multi-quantum well rib waveguide that is laterally tapered from 3 to 0.3 $\mu$m, and that contains five 1 % compressively strained 80 Å-thick $In_{0.78}Ga_{0.22}As_{0.79}P_{0.21}$ wells for emission at 1.55 $\mu$m, and four lattice-matched 150 Å-thick $In_{0.75}Ga_{0.25}As_{0.54}P_{0.46}$ barriers, surrounded by 400 Å-thick undoped confining layers having the same composition as the barriers. The metallization covers the spot size converters over their entire length in order to avoid absorption losses in the passive section of the taper. This means that there is current injection in a region where low optical gain is provided, increasing the threshold current and reducing the efficiency of these demonstration devices. The optimum metallization stop point should be a compromise

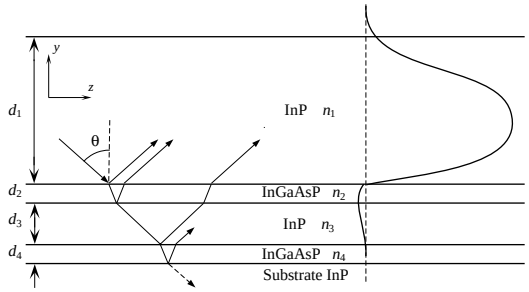


Figure C.2: Core of an ARROW waveguide, bounded at the upper surface by a low-index medium and at the substrate side by two higher-index antiresonant reflector layers.

between internal absorption loss and threshold current.

The underlying rib waveguide is optimized for coupling to an optical fiber, while keeping in mind the growth-imposed restriction of a maximum overall layer stack thickness of 11 $\mu$m. The vertical confinement of this fiber-matched mode is achieved by means of an ARROW geometry that is sketched in more detail in Fig. C.2. It consists of an InP core layer with refractive index $n_1$ and an interference cladding system, i.e., two higher index cladding layers made of quaternary material and a separating InP film, called the second cladding layer. This structure supports a certain number of bound modes in the high index claddings and several leaky waves, which are simply higher order modes beyond cutoff. Under appropriate conditions these leaky waves can be confined in the lower index core layer and propagate with relatively low losses. Considering the ray model we can treat it as a case where light coupled into the core undergoes total internal reflection at the upper surface and very high reflections from the sequence of antiresonant Fabry-Prot resonators formed by the InP-InGaAsP interfaces.

The antiresonance condition for the thickness of the respective cladding layers have been found as [14]

$$d_{2,4} = \frac{\lambda}{4n_{2,4}} \left( 1 - \left( \frac{n_1}{n_{2,4}} \right)^2 + \left( \frac{\lambda}{2n_{2,4} d_{ce}} \right)^2 \right)^{-1/2} \cdot (2M+1) \qquad \text{(C.1)}$$

$$d_3 = \frac{d_{ce}}{2}(2N+1) \qquad (M, N = 0, 1, 2, \ldots)$$

where $\lambda$ is the vacuum wavelength; $n_1$, $n_2$, $n_4$ the refractive index of the ARROW InP core, the first cladding layer and the third, respectively; $d_{ce}$ is the equivalent core thickness, which involves the Goos-Hänchen shift at the top of the ARROW core and is defined as:

$$d_{ce} = d_1 + \zeta \frac{\lambda}{2\pi\sqrt{n_1^2 - n_0^2}}, \qquad \text{(C.2)}$$

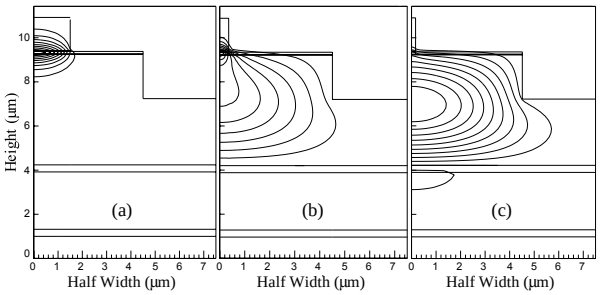


Figure C.3: Fundamental TE mode evolution along the taper structure of Fig. C.1 for (a) $w = 3$ $\mu$m, (b) $w = 0.7$ $\mu$m and (c) $w = 0.3$ $\mu$m. A shallow etch is simulated.

where

$$\zeta = \begin{cases} 1, & \text{for TE modes;} \\ (n_0/n_1)^2 & \text{for TM modes.} \end{cases} \tag{C.3}$$

In the above expressions $n_{co}$ denotes the refractive index of the active core and $n_0$ the refractive index of the polyimide that covers the device. We choose a quaternary compound with $\lambda_g = 1.3$ $\mu$m for the two high refractive index ARROW layers. The thickness of the ARROW core was limited to 5 $\mu$m to avoid problems with the growth of a thick layer stack. The calculated thickness of the corresponding cladding layers are $d_{2,4} = 0.32$ $\mu$m and $d_3 = 2.6$ $\mu$m (TE polarization).

The evolution of the optical field as a function of the upper rib is shown in Fig. C.3. As the active waveguide is tapered by reducing the ridge width from 3 to about 0.3 $\mu$m, the mode shifts adiabatically from the upper guide to the underlying ARROW waveguide (see Fig. C.3).

The design of the lateral taper is based on the adiabaticity of the mode transformation, and has been evaluated by means of a commercial 3-D eigenmode expansion algorithm based on a resonance method [15]. Small taper angles must be kept for the critical widths at which the mode transformation takes place to ensure an adiabatic mode transformation, while large taper angles are allowed for widths where the mode does not significantly change. Two designs, with a different etch depth for the laser rib, have been calculated. The two etch-stop points are indicated as $E_1$, $E_2$ in Fig. C.1. The shallow etching $E_1$ stops just above the layer containing the first quantum well (QW), while the deep etch $E_2$ goes through the QW's. It is expected that the former option will provide a better performance of the laser because it presents lower surface recombination. On the other hand, when the mode is expanded in the taper, it will be slightly confined in unpumped active quaternary layers [see Fig. C.3(c)]. This fact will introduce some absorption losses in the shallowly etched devices that are not present in the deeply etched ones. The adiabatic shape designs for both etching options have been approximated by a piecewise linear device consisting of three linear sections and are sketched in Fig. C.4. A minimum narrowing of 100 nm

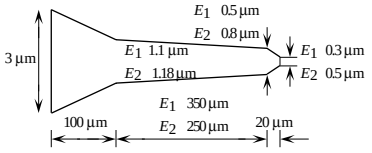


Figure C.4: The optimum taper shape is approximated by a piecewise linear device consisting of three linear sections. Tapers for both shallowly ($E_1$) and deeply ($E_2$) etched lasers are shown.

per 66 $\mu$m propagation length yields a safe design from the fabrication point of view.

### C.2.2 Device Processing

The epitaxial layers were grown by metal organic chemical vapor deposition (MOCVD). By plasma etching we defined the $SiO_x$pattern with conventional photoresist as a mask. The central and lateral ribs were etched by RIE to a depth 100 nm above the active layer. Next, a selective wet etch of the remaining InP down to the confining layer of the active layer was carried out. This etch was done using $H_3PO_4$:HCl (7:3). Finally, an extra 40 nm (shallow etch) or 140 nm (deep etch) RIE etch into the active layer was performed. Subsequently, a 9 $\mu$m wide and 2 $\mu$m high mesa was wet etched, using the above mentioned chemistry and parameters, to provide lateral index guiding for the expanded mode. Thereafter, polyimide was spin-coated on the sample to form an insulation layer. The thickness of the polyimide is less on top of the ridges compared to the rest of the sample. Therefore, by a controlled plasma etch, the dielectric was removed on the ridge while dielectric coverage remained elsewhere resulting in good electric isolation [8]. SEM pictures of the taper (Fig. C.5) reveal that the metal contact over this upper ridge is good and that the thin ribs were fabricated reproducibly. Next, using a negative photoresist and a metal liftoff process, the metallization pattern was defined. Finally, the thinning of the substrate was done and the back contact was deposited. Arrays of devices, each with 520 $\mu$m long straight active sections, were mounted on electrically cooled copper heatsinks with silver epoxy and were tested without any coatings. The entire device is electrically pumped because the metallization also covers the entire length of the spot size converters. 750 $\mu$m long and 3 $\mu$m wide untapered lasers, fabricated from the same wafer as the tapered lasers, were also prepared as a reference. Both reference and tapered lasers have the same total active area.

### C.2.3 Results and Discussion

All the measured parameters are shown in Table C.1 for comparison. The devices were operated in continuous wave (CW) operation. Some typical room temperature light intensity versus current ($L$–$I$) curves of mode-expanded and

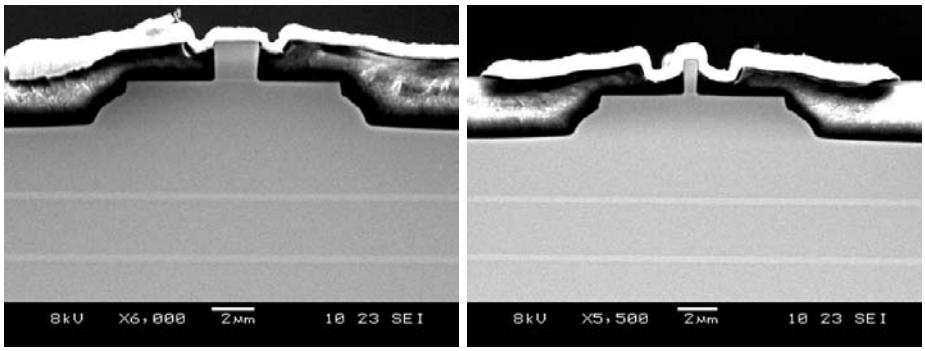


(a) (b)

Figure C.5: SEM image of the laser cross-section (a) at the beginning and (b) at the end of the tapering, showing the electric contact over the upper tapered rib and the high index ARROW cladding layers.

| Taper | Laser | Etching Depth | $I_{th}$ (mA) | $\eta_d$ (W/A) | $L$ (μm) | $FC$ (dB) | *FF* | | *Tol.* (±) | |
|---|---|---|---|---|---|---|---|---|---|---|
| | | | | | | | L (Deg.) | V (Deg.) | L (μm) | V (μm) |
| Vertical ARROW | Reference | $E_1$ | 31 | 0.09 | 0 | –8.2 | 30.5 | 43 | 1.9 | 2.1 |
| | | $E_2$ | 30 | 0.13 | 0 | –8 | 30.1 | 40.1 | 1.5 | 2 |
| | Tapered | $E_1$ | 45 | 0.1 | 470 | –2.9 | 10.4 | 22 | 2 | 2.2 |
| | | $E_2$ | 50 | 0.15 | 370 | –2.6 | 10 | 27 | 2.2 | 2.3 |
| Relaxed Vertical ARROW | Reference | $E_1$ | 35 | 0.13 | 0 | –8 | 30.3 | 39 | 1.8 | 2.1 |
| | | $E_2$ | 22 | 0.13 | 0 | –8.2 | 30.9 | 40.7 | 2 | 2.3 |
| | Tapered | $E_1$ | 60 | 0.11 | 470 | –2.7 | 11 | 19 | 2.3 | 2.4 |
| | | $E_2$ | 32 | 0.1 | 370 | –2.9 | 9.6 | 25 | 2.4 | 2.5 |
| Lateral ARROW | Reference | $E_1$ | 35 | 0.12 | 0 | –8 | 31.5 | 42.8 | 1.6 | 2 |
| | | $E_2$ | 28 | 0.12 | 0 | –8.3 | 30.7 | 40.6 | 1.5 | 2 |
| | Tapered | $E_1$ | 55 | 0.1 | 520 | –4 | 13.8 | 30.8 | 2.3 | 2.4 |
| | | $E_2$ | 48 | 0.12 | 490 | –4.3 | 13 | 32.7 | 2.2 | 2.3 |
| Variant 1, Fig. 16 | | $E_2$ | – | – | 490 | –2.4 | 7.2 | 14 | 2.3 | 1.9 |
| Variant 2, Fig. 17 | | Buried | – | – | 270 | –1.1 | 7.2 | 9 | 2.9 | 2.3 |

Table C.1: Measurement and simulation results on the integrated mode expanded lasers considered in this work: $I_{th}$ = threshold current; $\eta_d$ = external efficiency; $L$ = taper length; $FC$ = fiber-coupling efficiency; $FF$ = far-field divergence angles; $Tol.$ = −1 dB alignment tolerance. The last two rows correspond to simulation results.

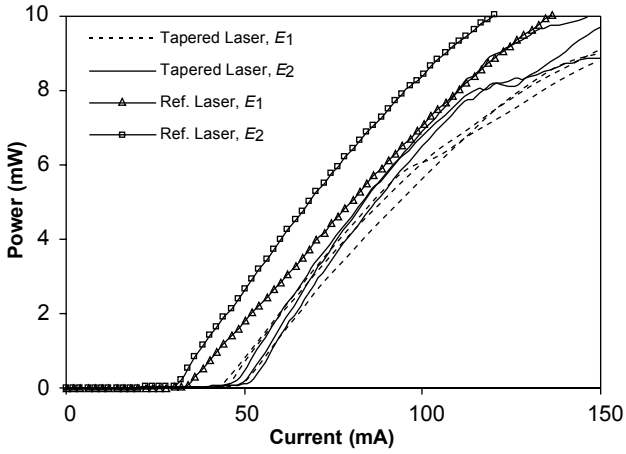


Figure C.6: Typical L-I characteristics of shallowly ($E_1$) and deeply ($E_2$) etched mode-expanded and untapered reference lasers.

untapered reference lasers are shown in Fig. C.6 for both etch depths. The deeply etched reference devices, with a threshold current of 30 mA and a external efficiency of 0.13 W/A, present a slightly better laser performance than the shallowly etched ones, which have a similar threshold current but a lower external efficiency (0.09 W/A). The deeply etched devices always show a better performance as we will see in the next sections of this paper. Fairly uniform threshold current distributions were found along the laser array.

Regarding the mode-expanded lasers, an increase of about 20 mA in the threshold current with respect to the reference lasers is found. This is a common behavior due to the mode transformation loss within the taper and to the losses in the n-doped thick InP ARROW core layer, and not to the introduction of the ARROW. A shorter current pumping length would reduce the threshold current. A higher slope efficiency is observed for the expanded mode laser. This surprising result can be attributed to a difference in reflectivity between the laser mode and the expanded mode [16], which can account for about 15 % difference in output power. For the shallowly etched devices, however, the mentioned increase is not so prominent since the efficiency is adversely influenced by the higher absorption loss in the unpumped QW's next to the central laser ridge [see Fig. C.3(c)].

Far-field emission patterns for both tapered and reference lasers were measured by using a rotating stage and a pinhole detector. The measured full width at half-maximum (FWHM) values are also shown in Table C.1, which are in good agreement with theoretical calculations obtained from the Fourier transform of the theoretical near fields. An important lateral divergence improvement is achieved for both groups of lasers, reaching a minimum of 10° for the deeply etched lasers. This value should be compared with the 30° divergence of the

reference devices. The vertical farfield is determined by the thickness of the ARROW slab core, which is limited by the maximum layer stack thickness as mentioned before. The achieved vertical field divergences are therefore higher (22° and 27° for both sets of lasers respectively, see Table C.1), but are still substantially lower than the 40° of the reference devices.

A coupling efficiency measurement was performed between the expanded mode laser and a standard cleaved single mode fiber with a spot size of 10 $\mu$m at 1.55 $\mu$m. Fiber coupling efficiencies better than $-3$ dB are obtained for both etch depths, including the Fresnel losses occurring at the air-glass interface. The improvement in the fiber coupling with respect to the untapered devices amounts up to 5.4 dB for the deeply etched lasers (see Table C.1).

Since the alignment tolerance with respect to the fiber depends on the large fiber mode, only slight improvements are observed with respect to the reference untapered lasers. A maximum $-1$ dB alignment tolerance of $\pm 2.2 \times \pm 2.3$ $\mu$m (lat. $\times$ vert.) is obtained for the deeply etched devices. The fact that the vertical alignment tolerance is higher than the lateral value is due to the fact that the fiber facet was separated from the taper output facet. These restrictions were considered to avoid contact of the fiber end with the laser output facet during the sweep of the transverse position of the fiber.

All results reported in Table C.1 are in good agreement with theoretical calculations.

## C.3 New Vertical ARROW Structures for Mode-Expanded Lasers

The three vertical ARROW-cladding layers ($d_1$, $d_2$ and $d_3$) used in the device of Section C.2 are designed to generate an antiresonance condition and provide minimum leakage loss towards the substrate for the fiber-matched output waveguide. However, from (C.1) and (C.2) it can be seen that the total thickness of this optimum cladding is higher than half the InP ARROW core thickness, which can be considered rather thick. Since the expanded ARROW-confined output mode is only guided over a short distance, it is not really necessary to reduce the ARROW-losses to an absolute minimum. In other words, it is allowed to move away from the antiresonance condition, thus increasing the radiation but also reducing the thickness of the cladding layers [12]. Fig. C.7 shows the leakage loss for the 5-$\mu$m thick ARROW waveguide used in the device of Section C.2 and calculated using the transfer matrix method (TMM) [17]. The leakage loss for the optimum design is 0.25 dB/cm. If a maximum propagation length of 300 $\mu$m is considered for the ARROW mode in the taper and a reasonable total leakage loss of 0.1 dB is allowed, the new claddings may exhibit a leakage loss as high as 3 dB/cm. The line that keeps this criterion is highlighted in Fig. C.7. The relaxed structure with a leakage loss of 3 dB/cm is $d_{2,4} = 0.31$ $\mu$m and $d_3 = 0.5$ $\mu$m, reducing the total cladding thickness to 1.12 $\mu$m, which is 2.12 $\mu$m less than the optimum structure.

Both shallowly and deeply etched devices were again implemented on a new

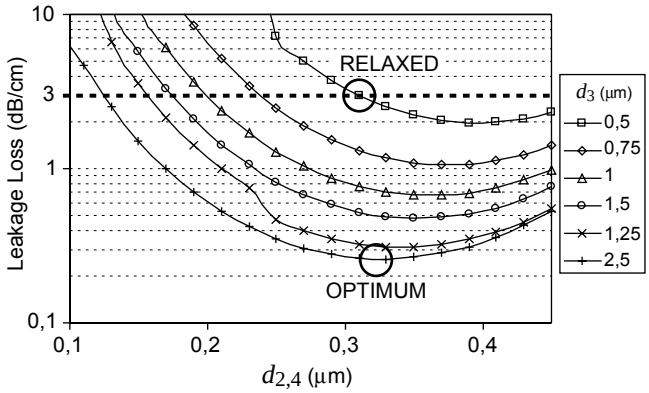


Figure C.7: Attenuation of the fundamental TE ARROW mode as a function of the thickness of the three cladding layers $d_2$, $d_3$ and $d_4$ for a core thickness $d_1 = 5$ $\mu$m.

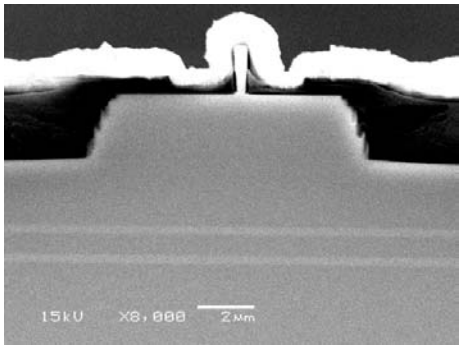


Figure C.8: SEM image of the laser cross-section using the relaxed ARROW structure.

wafer incorporating the new relaxed vertical ARROW structure and using the same processing as explained in Section C.2. Fig. C.8 shows the SEM photograph of one device. The operation of the mode expanders is not influenced by substituting the ARROW cladding structure with the relaxed design and the adiabatic taper shapes calculated in Section C.2 and shown in Fig. C.4 are still valid here. New arrays of devices, each with 520 $\mu$m long straight active sections were mounted. Untapered lasers, 750 $\mu$m long and 3 $\mu$m wide, and fabricated from the same wafer as the tapered lasers were also prepared as a reference.

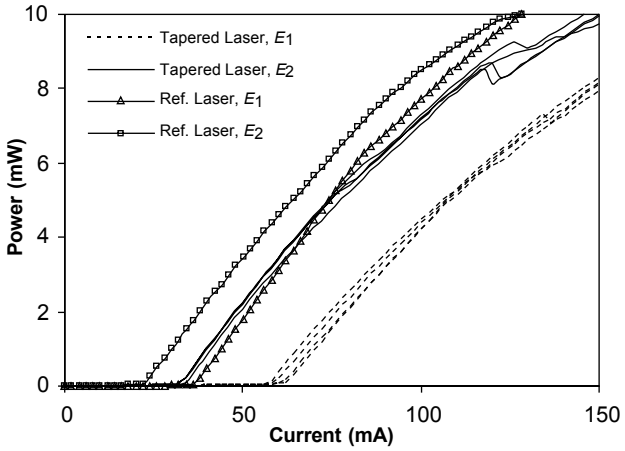


Figure C.9: Typical $L$–$I$ characteristics of shallowly ($E_1$) and deeply ($E_2$) etched untapered reference lasers and mode-expanded lasers incorporating the relaxed ARROW structure.

### C.3.1 Results

The CW room temperature $L$–$I$ curves of several mode-expanded and untapered reference lasers are shown in Fig. C.9 for both etch depths. The measured parameters are summarized in Table C.1. The deeply etched untapered lasers present the best performance. They show a threshold current around 22 mA, while the shallowly etched lasers exhibit a threshold of 35 mA.

Regarding the mode-expanded lasers, an increase of only 10 mA in the threshold current with respect to the reference is found for the deeply etched devices. In the case of the shallowly etched devices this increase in the threshold is of 25 mA.

The coupling efficiency to a standard single mode fiber does not change and also the lateral FWHM divergence angles remain the same. The vertical divergence angles, however, are reduced by a few degrees, as predicted by theoretical calculation [12]. The reason of this slight improvement is the reduction of the light in the new relaxed $d_2$, $d_3$ and $d_4$ cladding layers. The sign of the optical field in these layers [see Fig. C.3(c)] is opposed to the sign of the field in the InP core [14] and reduces the fiber coupling efficiency and the far-field divergence angles.

A maximum $-1$ dB alignment tolerance of around $\pm 2.4 \times \pm 2.5$ $\mu$m (lat. $\times$ vert.) is obtained for both sets of devices.

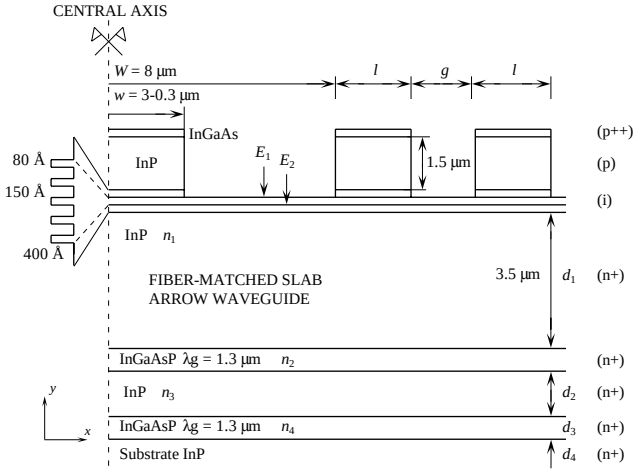


Figure C.10: Cross-section of the device that uses the antiresonant effect for both the lateral and the vertical confinement.

## C.4 Mode-Expanded Lasers Using Vertical And Lateral Arrow Confinement

### C.4.1 Device Design and Theory

The antiresonant effect can be used, not only for the vertical confinement, but also for the lateral confinement of the output fiber-matched mode [13], [18], [19]. The objective of this new device is to drastically simplify the fabrication process by eliminating the second etch step in which the broad underlying waveguide is defined. This eliminates the alignment of the second mask and reduces the fabrication complexity of the mode-expanded laser to that of a standard laser.

Fig. C.10 shows the right half of the cross-section of the proposed device. The laser structure and lower ARROW cladding materials are the same as in the previous devices. The lower InP core thickness is reduced to 3.5 $\mu$m because the lateral ribs lose their influence on the optical confinement when thicker layers are used. If thicker cores were needed, then more than two lateral ribs would have to be used. From (C.1)–(C.3), the optimum ARROW cladding is found to be $d_{2,4} = 0.32$ $\mu$m and $d_3 = 1.86$ $\mu$m. Relaxed structures to reduce the layer stack thickness could be found in a similar way as discussed in Section C.3 [12].

A couple of appropriately designed rib waveguides placed on each side of the tapered central waveguide and defined in the same etch step as the central laser ridge provide the lateral confinement of the guided mode. The behavior cannot be explained with the standard vertical ARROW formulas because of the guided modes that appear in the lateral ribs. Considering two-dimensional coupled-mode theory the new mode can be treated intuitively as an anti-symmetrical combination of the coupled modes of the upper lateral rib waveguides and the

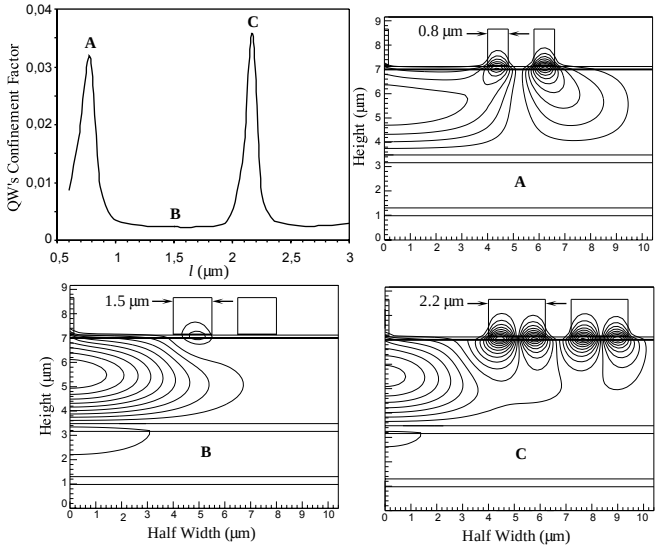


Figure C.11: Confinement of the output mode in the unpumped QW's in the lateral ARROW ribs of a shallowly etched device as a function of the width $l$ of the lateral ribs keeping the gap $g$ constant. The field distributions of the modes at the points indicated in the graph are also shown.

mode of the underlying InP slab ARROW core [20]. Thus, the shape of the output mode depends strongly on the width of the lateral ribs. Fig. C.11 shows the confinement of the fiber-matched leaky mode in the unpumped QW's of the lateral ribs as a function of the lateral rib width $l$ while keeping the gap $g$ constant and equal to 1 $\mu$m. This confinement should be minimized in order to reduce absorption loss in the unpumped lateral ribs. The field profiles for different widths $l$ are also shown for illustration. A flat and broad minimum confinement is found around $l = 1.5$ $\mu$m, where the output mode is fit for coupling to fiber. The broad minimum implies that the device is tolerant to fabrication errors. Two designs, with a different etch depth for the central laser rib, are considered once again (shown as $E_1$, and $E_2$ in Fig. C.10) and the optimum width $l$ for the deeply etched device is also calculated and found to be 1.6 $\mu$m. In both etch options the optimum gap $g$ between lateral ribs is less than 1 $\mu$m, but has to be increased to 1 $\mu$m because of fabrication limitations. Fortunately, this does not change the modal shape significantly.

The evolution of the optical field as a function of the upper central rib width is shown in Fig. C.12. As the active waveguide is tapered by reducing the ridge width from 3 to 0.3 $\mu$m, the mode shifts adiabatically from the upper guide to the underlying ARROW waveguide (Fig. C.12). The design of the lateral tapering is based on the adiabaticity of the mode transformation, and has been evaluated by means of a commercial 3-D eigenmode expansion. The adiabatic shape designs for both etching options have been approximated by a piecewise

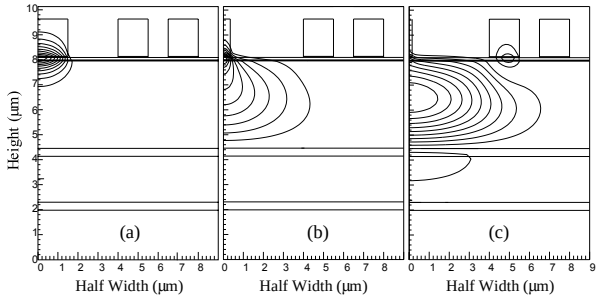


Figure C.12: Fundamental TE mode evolution along the taper structure of Fig. C.10 for (a) $w = 3$ $\mu$m, (b) $w = 0.7$ $\mu$m and (c) $w = 0.3$ $\mu$m (shallow etch).

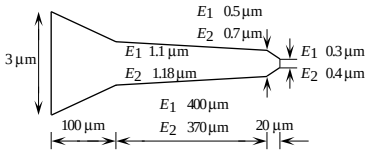


Figure C.13: Piecewise linear approximation of the ideal taper shape for the device with both vertical and lateral ARROW confinement. Tapers for both a shallowly ($E_1$) and deeply ($E_2$) etched laser are shown.

linear device consisting of three linear sections and are sketched in Fig. C.13. A minimum narrowing of 100 nm per 77 $\mu$m propagation length yields a safe design from the fabrication point of view.

The expanded mode in the shallowly etched device is slightly confined in unpumped active quaternary layers [see Fig. C.12(c)]. This will introduce some absorption losses in the shallowly etched lasers that are not present in the deeply etched designs.

### C.4.2 Device Processing

A wafer with the new layer structure was grown by MOCVD and the devices were implemented using the same processing steps as detailed in Section C.2 (except, of course, the wet etching of the broad rib). Fig. C.14 shows a SEM picture of the device, illustrating the contacting of the central ridge and the well-defined lateral ribs. Once again, arrays of devices, each with 520 $\mu$m long straight active sections, were mounted on electrically cooled copper heatsinks with silver epoxy and were tested without any coatings. Untapered lasers (750 $\mu$m $\times$ 3 $\mu$m) fabricated from the same wafer as the tapered lasers, were also prepared as a reference.

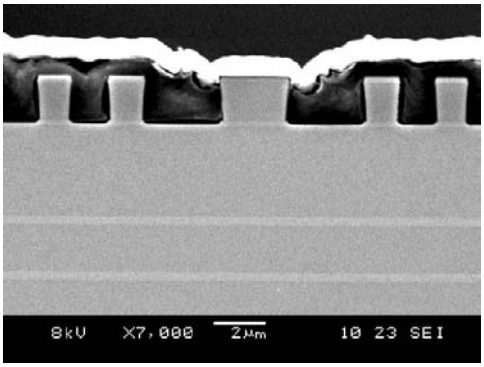


Figure C.14: SEM image of the laser cross-section, showing the electric contact over the central tapered rib, the good definition of the lateral ribs and the high index ARROW cladding layers.

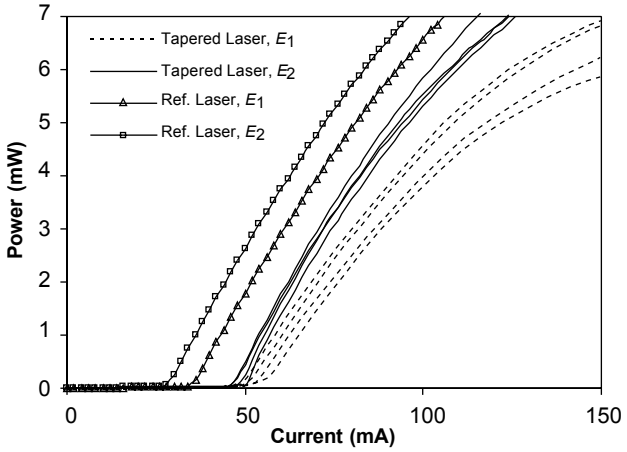


Figure C.15: Typical $L$–$I$ characteristics of shallowly ($E_1$) and deeply ($E_2$) etched untapered reference lasers and mode-expanded lasers using the vertical and lateral ARROW-confined fiber-matched waveguide.

### C.4.3 Results and Discussion

All the measured parameters are shown in Table C.1. Typical room temperature $L$–$I$ curves of mode-expanded and untapered reference lasers are shown in Fig. C.15 for both etch depths. The deeply etched reference devices, with a threshold current of 28 mA, present a better laser performance than the shallowly etched ones (35 mA). A uniform threshold current distribution was found along the laser array once again.

Regarding the mode-expanded lasers, an increase of about 20 mA in the

threshold current with respect to the reference lasers is found. The higher absorption loss in the unpumped QW's of the lateral ARROW rib waveguides for the shallowly etched devices [see Fig. C.12(c)] causes a decrease of the external efficiency of the laser from 0.12 W/A to 0.1 W/A. This fact is not observed in the deeply etched devices that maintain the same external efficiency as the reference lasers.

The measured full width at half-maximum (FWHM) values are also shown in Table C.1. A considerable improvement is achieved in the lateral direction for both groups of lasers, reaching a minimum of 13° for the deeply etched lasers. On the other hand, due to the thinner ARROW slab core (3.5 $\mu$m), the achieved vertical field divergence is still slightly higher than 30°, improving it by 10° with respect to the reference laser. A further improvement in the vertical far-field pattern could be obtained by thickening the ARROW core layer and defining more than two ribs on each side of the output ARROW waveguide in order to provide a good lateral confinement for thick cores.

Maximum fiber coupling efficiencies of around $-4$ dB are obtained for both etch depths, including the Fresnel losses occurring at the air-glass interface. The improvement in the fiber coupling with respect to the untapered devices amounts up to 4 dB (see Table C.1). A maximum $-1$ dB alignment tolerance of around $\pm 2.3 \times \pm 2.4$ $\mu$m is obtained for both sets of lasers.

Again all the results are in good agreement with theoretical calculations.

### C.4.4 Variant 1: Weakly Guiding Fiber-Adapted Waveguide

The waveguide structure of Fig. C.10 has a limitation on the vertical direction because the lateral ribs lose their optical confinement effect when the slab core becomes too thick. The structure of Fig. C.16 is similar to that of Fig. C.10 but it makes use of a thin weakly-guiding core of only 80 nm that is buried in InP beneath the active layer. The mode at the active rib and the mode at the end of the taper are also shown. The fiber-matched mode presents a quite asymmetrical field distribution in the vertical direction, but the fact that its maximum is closer to the upper lateral couple of ribs strengthens their influence. Moreover, from a coupling and far-field point of view the typical exponential decay of weakly guiding waveguides induces an improvement of the coupling efficiency and FWHM of the output beam in comparison with the untapered lasers, in spite of its asymmetrical shape.

Simulation results on the propagation of this new structure are shown in Table C.1. Only the design for the deep etching through the QW's has been considered because of its better lasing performance. The same tapering as sketched in Fig. C.13 has been simulated. It appears that the beam divergence angles and the coupling efficiency are improved to 7.2° × 14° (lat. × vert.) and $-2.4$ dB, respectively. The vertical alignment tolerance is slightly reduced to $\pm 1.9$ $\mu$m, while the lateral value remains the same as for the vertical ARROW-design.

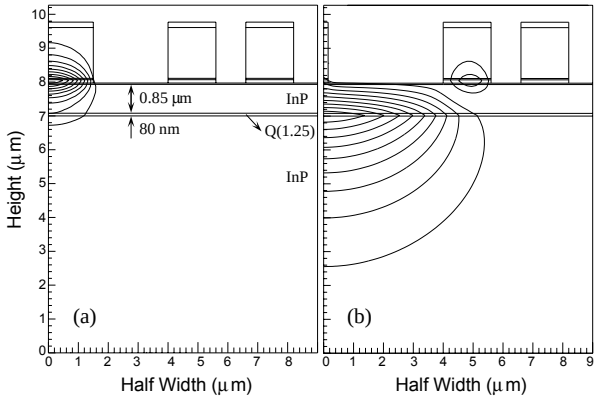


Figure C.16: Schematic structure of the taper using a weakly guiding underlying slab waveguide. The active layer and upper rib waveguides are identical to those of Fig. C.10.

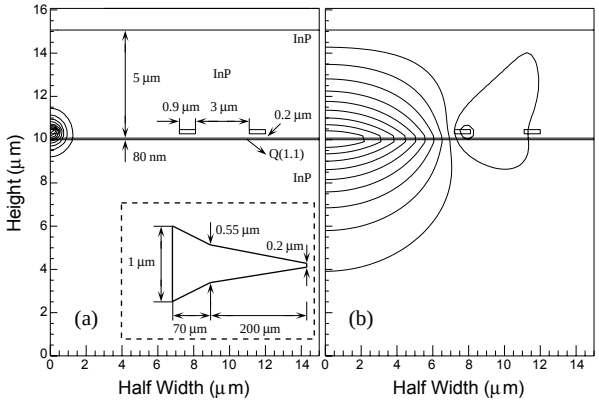


Figure C.17: Schematic structure of a buried variant of the proposed taper concept.

### C.4.5 Variant 2: Buried Laser

The mode transformation concept proposed in this section can also be integrated in a second variant, being a buried laser structure as shown in Fig. C.17. A 194 nm thick buried MQW active structure with an equivalent refractive index of 3.45 is tapered from 1 to 0.2 $\mu$m following the tapering shown in the inset of Fig. C.17(a). The 70 nm thin guiding layer of quaternary compound with $\lambda_g = 1.1$ $\mu$m is buried 0.2 $\mu$m beneath the active core. The optimum lateral confinement ARROW ribs are 0.9 $\mu$m wide and are separated by 2 $\mu$m. All this is embedded under a 5 $\mu$m thick top layer of InP.

The fact that the tapered active central core is totally embedded in InP makes the mode transformation efficiency much higher for buried than for rib structures. This is the reason why the length of the buried taper (270 $\mu$m) is much shorter than the rib taper (490 $\mu$m).

Simulation results on the propagation are shown in Table C.1. They show fiber butt coupling losses as low as 1.1 dB, beam divergence angles of $7.2° \times 9°$ (lat. $\times$ vert.), and alignment tolerances of $\pm 2.9 \times \pm 2.3$ $\mu$m (lat. $\times$ vert.), compared to the 8.5 dB coupling loss and $29° \times 32°$ divergence angles of the untapered devices.

## C.5 Conclusion

In this paper we have presented the use of optical confinement by the ARROW-concept for the fabrication of lasers with monolithically integrated spot size converters. This eliminates the need for thick $In_{1-x}Ga_xAs_yP_{1-y}$ layers and the consequential growth problems. The taper transforms the small active laser mode into the fiber-adapted mode of the large underlying mesa with vertical ARROW confinement. Threshold currents of around 50 mA were measured, which have to be compared with 30 mA for untapered reference lasers. The far-field FWHM divergence angles were significantly reduced and the coupling efficiency to single mode fiber was improved by 5.4 dB.

We also calculated that the ARROW cladding thickness can be reduced drastically by moving away from the optimal anti-resonance condition without introducing remarkable extra losses. The new structures significantly reduce the overall layer stack thickness while maintaining the far-field divergence angles and the fiber coupling efficiency of the optimum ARROW structures.

Lateral ARROW confinement, in combination with vertical confinement, was also successfully demonstrated. The lateral confinement of the fiber-matched mode is achieved by means of an antiresonant effect provided by two sets of lateral rib waveguides defined in the same etching process as the central active ridge. Therefore, only a single planar growth step and a single conventional etching process are required, leading to the simplest tapered laser concept ever reported. Threshold currents of around 50 mA were measured, which have to be compared with 30 mA for untapered lasers. The far-field FWHM divergence angles were significantly reduced and 4 dB improvement of the coupling efficiency to single mode fiber was observed.

Two variants of the demonstrated concept have also been analyzed by simulation and are expected to show a better performance. In a first variant a weakly-guiding slab waveguide substitutes the thicker core of the first structure. In a second variant the taper concept of this work is integrated in a buried laser structure. Simulation results show considerable improvements in the far-field divergence angles and fiber-coupling efficiencies.

## References

[1] I. Moerman, P. Van Daele, and P. M. Demeester, "A review on fabrication technologies for the monolithic integration of tapers with III-V semiconductor devices," *IEEE J. Select. Topics Quantum Electron.*, vol. 3, pp. 1308–1320, Dec. 1997.

[2] T. Alder, A. Sthr, R. Heinzelmann, and D. Jger, "High-efficiency fiber-to-chip coupling using low-loss tapered single-mode fiber," *IEEE Photon. Technol. Lett.*, vol. 12, pp. 1016–1018, Aug. 2000.

[3] Y. Suzaki, K. Magari, Y. Kondo, Y. Kawaguchi, Y. Kadota, and K. Yoshino, "High-gain array of semiconductor optical amplifier integrated with bent spot-size converter (BEND SS-SOA)," *IEEE J. Lightwave Technol.*, vol. 19, pp. 1745–1750, Nov. 2001.

[4] D. Jang, J. Shim, J. Lee, and Y. Eo, "Asymmetric output characteristics in 1.3-$\mu$m spot-size converted laser diodes," *IEEE J. Quantum Electron.*, vol. 37, pp. 1611–1617, Dec. 2001.

[5] S. S. Saini, F. G. Johnson, D. R. Stone, H. Shen, W. Zhou, and M. Dagenais, "Passive active resonant coupler (PARC) platform with mode expander," *IEEE Photon. Technol. Lett.*, vol. 12, pp. 1025–1027, Aug. 2000.

[6] G. A. Vawter, A. T. Sullivan, J. R. Wendt, R. E. Smith, H. Q. Hou, and J. F. Klem, "Tapered rib adiabatic following fiber couplers in etched GaAs materials for monolithic spot-size transformation," *IEEE J. Select. Topics Quantum Electron.*, vol. 3, pp. 1361–1371, Dec. 1997.

[7] K. De Mesel, R. Baets, C. Sys, S. Verstuyft, I. Moerman, and P. Van Daele, "First demonstration of a 980 nm oxide confined laser with integrated spot size converter," *Electron. Lett.*, vol. 36, pp. 1028–1029, Jun. 2000.

[8] V. Vusirikala, S. S. Saini, R. E. Bartolo, S. Agarwala, R. D. Whaley, F. G. Johnson, D. R. Stone, and M. Dagenais, "1.55-$\mu$ InGaAsP–InP laser arrays with integrated-mode expanders fabricated using a single epitaxial growth," *IEEE J. Select. Topics Quantum Electron.*, vol. 3, pp. 1332–1343, Dec. 1997.

[9] M. Galarza, K. De Mesel, S. Verstuyft, C. Aramburu, I. Moerman, P. Van Daele, R. Baets, M. Lopez-Amo, "1.55 $\mu$m InP–InGaAsP Fabry-Pérot lasers with integrated spot size converters using antiresonant reflecting optical waveguides", *IEEE Photon. Technol. Lett.*, vol. 14, pp. 1043–1045, Aug. 2002.

[10] M. A. Duguay, Y. Kokubun, T. L. Koch, and L. Pfeiffer, "Antiresonant reflecting optical waveguides in $SiO_2$-Si multilayer structures", *Appl. Phys. Lett.*, vol. 49, pp. 13–15, Jul. 1986.

[11] T. L. Koch, U. Koren, G. D. Boyd, P. J. Corvini, and M. A. Duguay, "Antiresonant reflecting optical waveguides for III-V integrated optics," *Electron. Lett.*, vol. 23, pp. 244–245, Feb. 1987.

[12] M. Galarza, K. De Mesel, D. Fuentes, R. Baets, M. Lopez-Amo, "Modeling of InGaAsP–InP 1.55 $\mu$m lasers with integrated mode expanders using fiber matched leaky waveguides," *Appl. Phys. B-Lasers Opt.*, vol. 73, pp. 585–588, Oct. 2001.

[13] M. Galarza, K. De Mesel, T. Van Caenegem, S. Verstuyft, C. Aramburu, I. Moerman, P. Van Daele, R. Baets, M. López-Amo, "InGaAsP–InP 1.55 $\mu$m lasers with integrated mode expanders using fiber-matched leaky waveguides", in *Proc. LEOS '01 Annual Meeting*, San Diego, California, USA, Nov. 2001, pp. 798–799.

[14] J. M. Kubica, "Numerical analysis of InP/InGaAsP ARROW waveguides using transfer matrix approach," *IEEE J. Lightwave Technol.*, vol. 10, pp. 767–771, June 1992.

[15] A. S. Sudbo, "Numerically stable formulation of the transverse resonance method for mode-field calculations in dielectric waveguides," *IEEE Photon. Technol. Lett.*, vol. 5, pp. 342–344, March 1993.

[16] M. Reed, T. M. Benson, P. C. Kendall, and P. Sewell, "Antireflection coated angled facet design," *IEE Proc. Pt J.*, 1996, pp. 214-220.

[17] J. Chilwell, and I. Hodgkinson, "Thin-films field-transfer matrix theory of planar multilayer waveguides and reflection from prism-loaded waveguides," *J. Opt. Soc. Am. B, vol. 1*, pp. 742–753, Jul. 1984.

[18] L. J. Mawst, D. Botez, C. Zmudzinski, and C. Tu, "Design optimization of ARROW-type diode lasers", *IEEE Photon. Technol. Lett.*, vol. 4, pp. 1204–1206, Nov. 1992.

[19] L. J. Mawst, D. Botez, C. Zmudzinski, and C. Tu, "Antiresonant reflecting optical waveguide-type, single-mode diode laser," *Appl. Phys. Lett.*, vol. 61, pp. 503–505, Aug. 1992.

[20] G. R. Hadley, "Two-dimensional coupled-mode theory for modeling leaky-mode arrays," *Opt. Lett.*, vol. 15, pp. 27–29, Jan. 1990.

## Publication D

# InGaAsP–InP 1.55 $\mu$m Lasers with Integrated Mode Expanders Using Fiber-Matched Leaky Waveguides

M. Galarza, K. De Mesel, T. Van Caenegem, S. Verstuyft, C. Aramburu, I. Moerman, P. Van Daele, R. Baets, and M. López-Amo

*LEOS '01 Annual Meeting*, San Diego, California, USA, pp. 798–799, Nov. 2001.

***Abstract***—A new concept for InGaAsP–InP 1.55 $\mu$m lasers integrated with spot size converters using antiresonant reflecting optical waveguides, is presented. The devices exhibit low radiation losses, and good fiber-coupling and far-field angles.

## D.1 Introduction

The packaging of optoelectronic integrated semiconductor circuits amounts up to about 80 % of the cost of the final module. Highly-efficient chip-to-fiber coupling with large alignment tolerances is a critical requirement to obtain low-cost optoelectronic devices. Problems arise from the optical field mismatch between the large circular fiber mode and the small asymmetric semiconductor waveguide mode. Directly butt-coupled devices present typically 7–10 dB fiber insertion loss and submicron alignment tolerances. To achieve both low coupling loss and large alignment tolerances it is necessary to transform the mode on-chip to better match the fiber. A large variety of integrated mode transformers have been proposed but they often require complex (re)growth and etching techniques [1]. The new taper concept presented in this work is based on the use of antiresonant reflecting optical waveguides (ARROW) [2] and simplifies the fabrication process to one planar growth step and one conventional non-critical etch step. The design, fabrication and performance of the new device are discussed.

## D.2 Design and Fabrication

The design of the proposed tapered laser is inspired by the more conventional approach as reported in [3] where a thin waveguide is defined on top of a large fiber-adapted mesa. The optical mode is confined in the upper waveguide when the upper rib is broad. A gradual narrowing of the upper rib expands the mode into the underlying mesa. In the new design the fiber-matched broad waveguide is a leaky waveguide where the vertical and lateral confinement of

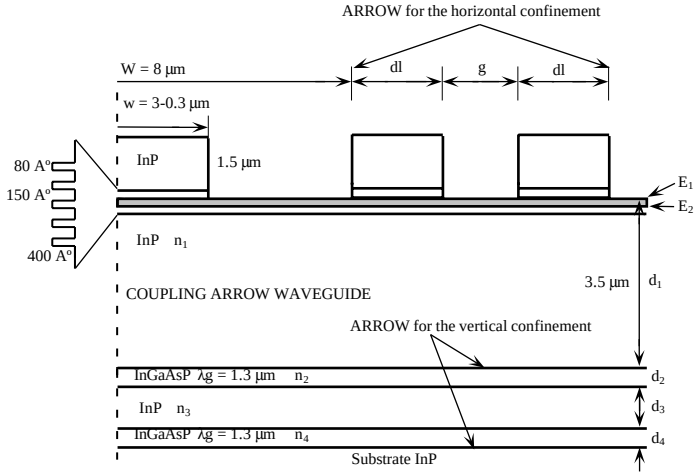


Figure D.1: Schematic drawing of the adiabatic mode expanded laser showing the tapered upper active rib and the underlying fiber-matched ARROW waveguide.

its mode are achieved by means of three antiresonant structures [4]. The transverse structure of the proposed laser is shown in Fig. D.1. The active layer consists of five 1 % compressively strained 80 Å-thick $In_{0.78}Ga_{0.22}As_{0.79}P_{0.21}$ quantum wells (QW) for emission at 1.55 $\mu$m, and four lattice-matched 150 Å-thick $In_{0.75}Ga_{0.25}As_{0.54}P_{0.46}$ barriers, surrounded by 400 Å-thick SCH regions. The vertical confinement in the lower large guide is provided by a conventional ARROW-structure. We choose a quaternary compound with $\lambda_g = 1.3$ $\mu$m for the two high refractive index ARROW layers. From the design formulas of the ARROW cladding layers reported in [2], we calculate $d_2 = d_4 = 0.32$ $\mu$m and $d_3 = 1.86$ $\mu$m. The lateral confinement is provided by two sets of lateral ARROW ribs defined in the same etch step as the central one. The design of the ribs differs from that employed for the vertical ARROW due to the guided modes of every rib guide [5, 6]. A sweep of the confinement of the output mode in the active layer in function of the lateral rib widths and gaps ($dl$, $g$) was done, and the minimum confinement was obtained for $dl = 1.5$ $\mu$m and $g < 1$ $\mu$m; nevertheless $g$ had to be increased to 1 $\mu$m because of fabrication tolerances. Fig. D.2 shows the evolution of the mode along the taper. The output leaky mode can be seen. The SEM photograph shown in Fig. D.3 clearly shows the lateral ribs. The depression in the electrode is due to misalignments in the etching of the insulating polyimide, and this does not effect the operation of the device.

The spot size converter was modeled with a 3D eigenmode expansion algorithm [7]. Small taper angles must be kept for the critical widths at which the mode transformation takes place to ensure an adiabatic mode transformation, while large taper angles are allowed for widths where the mode does not significantly change. Two different designs have been carried out for two differ-

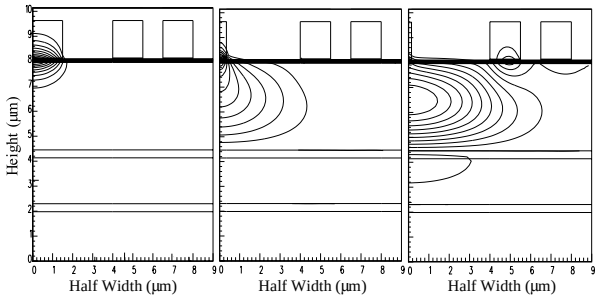


Figure D.2: Fundamental TE mode for $w = 3$, 0.7 and 0.3 $\mu$m.

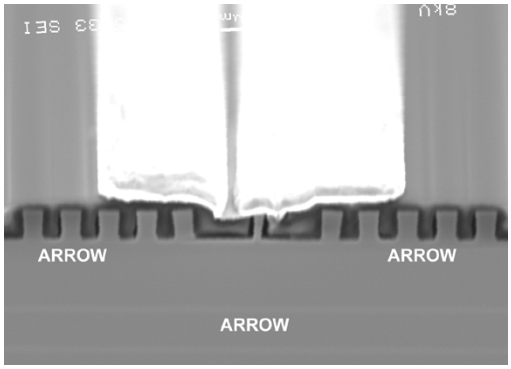


Figure D.3: SEM image of laser cross-section.

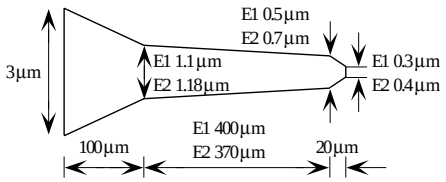


Figure D.4: The optimum taper shape is approximated by a piecewise linear device consisting of three linear sections.

ent etch depths. The implemented etch stop points are indicated as $E_1$, $E_2$ in Fig. D.1. The adiabatic shape designs for both options have been approximated by a piecewise linear device consisting of three linear sections and are sketched in Fig. D.4. A minimum narrowing of 100 nm per 77 $\mu$m propagation yields a safe design from the fabrication tolerances point of view.

Fig. D.5-a and D.5-b are simulations of the lateral and transversal view of the expanding field in the ARROW tapered devices. The propagation has been modeled using BPM to take into account the leaky losses of the device. The confinement provided by the antiresonant structures can be observed. Simulation results provide total transformation losses lower than 0.18 dB and coupling efficiencies to a standard SMF of 43 %.

## D.3 Results and Discussion

The metallisation covers the spot size converters over their entire length. This can have a negative impact on the threshold current and efficiency, but on the other hand it avoids the risk of high absorption losses in the passive section of the taper. The devices were operated in CW mode. Fig. D.6 shows the light power versus current ($L$–$I$) characteristics of 6 expanded mode devices and a control sample without any tapers. The tapered devices presenting the two best responses are also plotted. Untapered reference lasers ($L$ = 750 $\mu$m, $w$ = 3 $\mu$m) exhibit typical threshold currents $I_{th}$ of 30 mA. Expanded mode devices ($L_{active}$ = 500 $\mu$m) have $I_{th}$ around 60 and 70 mA for the, deeply and shallowly etched devices, respectively. This higher threshold current for the $E_1$ etch option is due to the higher confinement of the tapered mode in the QW's of the active layer that are not etched. The far-field emission patterns are shown in Fig. D.7. The horizontal and vertical full widths at half maximum (FWHM) are reduced from res. 33 and 36.2° (34 and 36.4°) for the untapered lasers to res. 7.6 and 25° (10.6 and 26.4°) for the tapered devices and etch option $E_1$ ($E_2$).

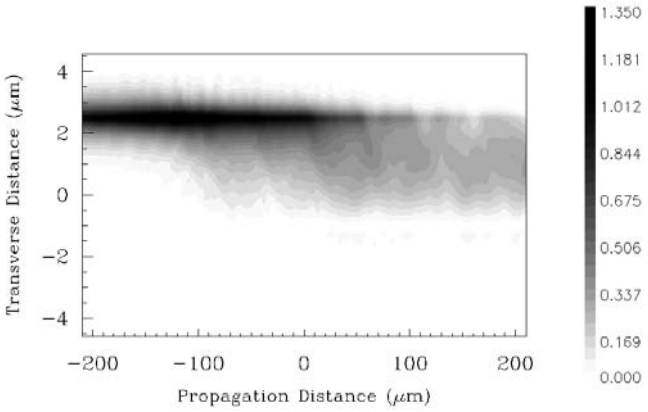


(a)

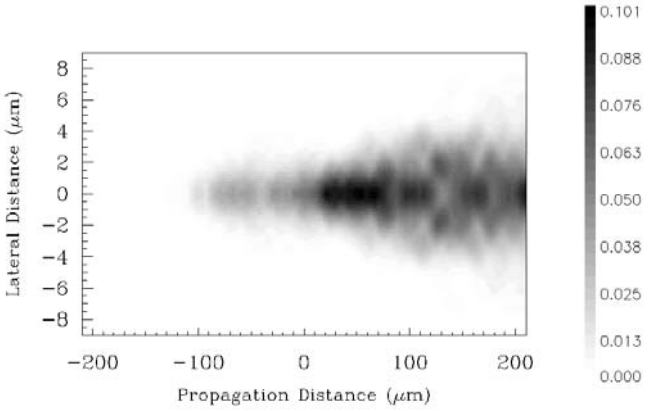


(b)

Figure D.5: (a) Lateral and (b) transversal view on the TE mode evolution in the device of Fig. D.1.

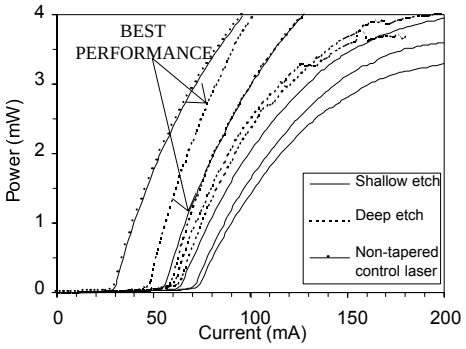


Figure D.6: $L$–$I$ characteristics of several mode expanded lasers compared to a control laser without any taper.

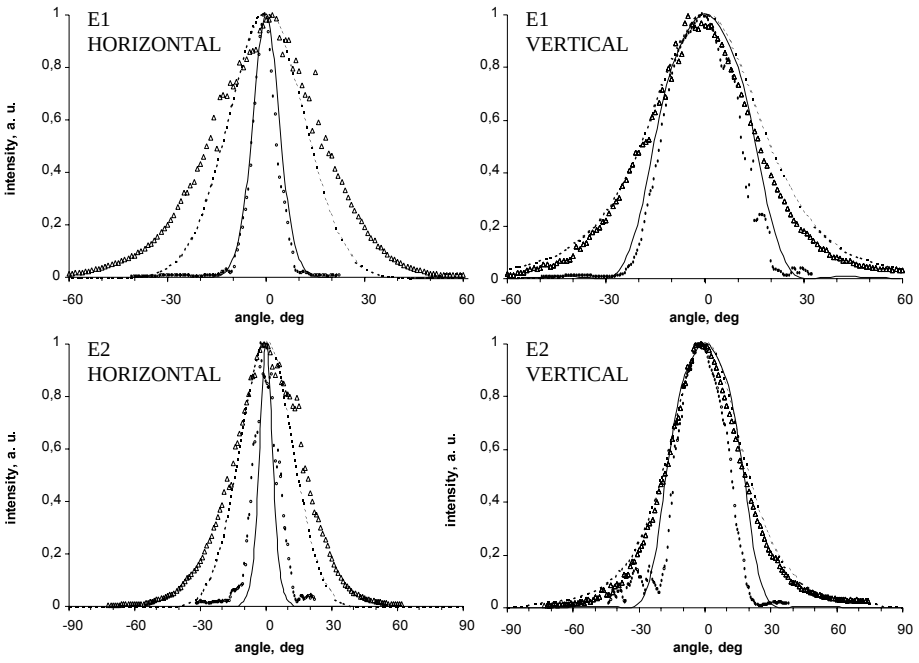


Figure D.7: Far-field emission patterns of tapered and untapered lasers and $E_1$ and $E_2$ etch options. — tapered laser, simulated; ∘ tapered laser, measured; - - - laser, simulated; △ laser, measured.

## D.4 Conclusion

We have successfully demonstrated a novel mode-expanded laser based on the adiabatic transformation of the laser rib mode into a fiber-matched ARROW waveguide. The fabrication is drastically simplified to one planar growth step and one conventional non-critical etch step. Efficient mode transformation and considerable reduction of the horizontal and vertical far-field FWHM have been achieved.

## References

[1] I. Moerman, P. P. Van Daele, P. M. Demeester: *IEEE J. Select. Topics Quantum Electron.* **3**, 6, pp. 1308–1320 (1997).

[2] J. M. Kubica: *IEEE J. Lightwave Technol.* **10**, 6, pp. 767–771 (1992).

[3] G. A. Vawter, R. E. Smith, H. Hou, J. R. Wendt: *IEEE Photonics Technol. Lett.* **9**, pp. 425–427 (1997).

[4] M. Galarza, K. De Mesel, R. Baets, M. López-Amo: *Proc. ECIO '01*, pp. 421–424 (2001).

[5] P. Yeh, C. Gu, D. Botez: *J. Opt. Soc. Am. B* **10**, 4, pp. 709–715 (1993).

[6] G. R. Hadley: *Opt. Lett.* **15**, 1, pp. 27–29 (1990).

[7] Fimmprop-3D propagation tool from Photon Design; `http://www.photond.com`

## Publication E

# A New Spot-Size Converter Concept Using Fiber-Matched Antiresonant Reflecting Optical Waveguides

M. Galarza, K. De Mesel, S. Verstuyft, C. Aramburu, M. López-Amo, I. Moerman, P. Van Daele, and R. Baets

*Journal of Lightwave Technology*, Accepted for publication, vol. 21, no. 1, Jan. 2003.

***Abstract***—We report on a new concept for InGaAsP–InP 1.55 $\mu$m lasers with integrated spot-size converters based on antiresonant reflecting optical waveguides (ARROW). The mode expanders consist of a laterally tapered active region on top of a fiber-matched passive slab waveguide. The large slab mode is laterally confined by an antiresonant configuration of a couple of lateral waveguides defined in the same fabrication process as the active ridge. This feature makes the presented spot-size transformer as simple to fabricate as a standard waveguide, only requiring a planar growth step and a single conventional etch process. The fabricated tapers exhibit a low transformation loss and reduce the coupling loss to standard single-mode fibers from 8 to 4 dB. We also analyze by simulation two variants of the concept proposed in this work, including a taper structure for a buried waveguide, which are expected to show better performance. Simulation results show fiber-coupling efficiencies as low as 2.4 and 1.1 dB for both variants.

## E.1 Introduction

There exist two rationales for the use of integrated spot-size converters (SSC) in the development of low-cost opto-electronic devices. One is the pigtailing or fiber attachment of III-V semiconductor photonic integrated circuits (PIC), mostly active devices containing lasers or semiconductor optical amplifiers; and the other is the integration of such PIC's with silica-on-silicon waveguides for the development of hybrid devices. The SSC's provide high coupling efficiencies and large alignment tolerances that enable the use of passive alignment schemes that drastically reduce the packaging cost. The function of an integrated SSC is to enlarge and to reshape the small and asymmetric mode of the III-V semiconductor waveguide component to a large and circular mode that is better adapted to the fiber or silica waveguide. Direct butt-coupling with an untapered device typically introduces 7–10 dB coupling loss. The use of microlenses or tapered/lensed fiber that reduce the size of the largest mode, improves the coupling loss but at

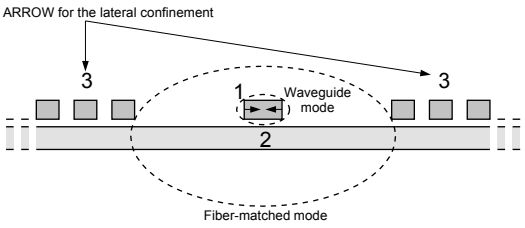


Figure E.1: Schematic (not to scale) of the new spot-size converter concept, using a fiber-matched ARROW waveguide.

the expense of the alignment tolerance, which remains under the micrometer.

Over the past ten years much research has focused on the integration of mode size converters with waveguide components in order to improve the coupling efficiency. Most of these approaches involve complex growth and/or processing steps, requiring extensive process development [1]. In this paper, we present a new concept for the fabrication of highly efficient and simple-to-fabricate SSC's by making use of ARROW waveguides. We experimentally demonstrate the concept for a 1.55 $\mu$m InGaAsP–InP laser and analyze and propose, by simulation, two interesting variants of the structure.

## E.2 Concept

A schematic of the SSC concept presented in this work is shown in Fig. E.1. The device consists of a standard waveguide that is laterally tapered along its propagation direction (region 1 in Fig. E.1) and placed on top of a fiber-matched (or silica waveguide-matched) slab waveguide (region 2 in Fig. E.1). Two sets of additional ridges are defined on both sides of the central standard waveguide in the same processing step (region 3 in Fig. E.1) that creates the tapered ridge one. The adiabatic lateral tapering causes the spreading of the small mode into the broader slab waveguide, increasing its size both laterally and vertically. The lateral guiding of the fiber-matched mode is provided by the two sets of lateral waveguides by means of an antiresonance effect, so this structure can be considered as an ARROW waveguide [2], [3]. As the lateral and central tapered waveguide can be defined in the same processing step, this taper is the simplest 2-D SSC demonstrated so far.

## E.3 Device Design and Theory

The transverse structure of the proposed mode-expanded laser is shown in Fig. E.2. The device consists of an active multi-quantum well rib waveguide that is laterally tapered from 3 to 0.3 $\mu$m, and that contains five 1 % compressively strained 80 Å-thick $In_{0.78}Ga_{0.22}As_{0.79}P_{0.21}$ wells for emission at 1.55 $\mu$m, and

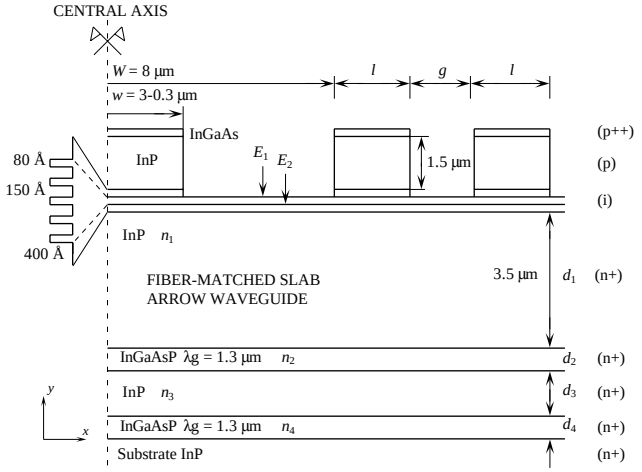


Figure E.2: Schematic drawing of the adiabatic mode-expanded laser showing the tapered upper active rib, the underlying fiber-matched ARROW slab waveguide and the lateral confinement rib waveguides.

four lattice-matched 150 Å-thick $In_{0.75}Ga_{0.25}As_{0.54}P_{0.46}$ barriers, surrounded by 400 Å-thick undoped confinement layers with the same composition as the barriers.

The underlying passive slab waveguide is realized by a standard vertical ARROW waveguide [4]. A quaternary compound with $\lambda_g = 1.3$ $\mu$m for the two high-refractive index ARROW layers was chosen. The thickness of the ARROW core was limited to 3.5 $\mu$m to avoid the loss of the lateral confinement effect when the slab core becomes too thick. The thickness of the corresponding cladding layers are: $d_{2,4} = 0.32$ $\mu$m and $d_3 = 1.86$ $\mu$m (TE polarization) [4]. The total epitaxial layer thickness is not attractive form a growth point of view, but we already demonstrated in previous work that they could be considerably reduced without altering the performance of the device [5].

A couple of appropriately designed rib waveguides placed on each side of the tapered central waveguide provides the lateral confinement of the guided mode. The behavior cannot be explained with the standard vertical ARROW formulas because of the guided modes that appear in the lateral ribs. Considering two-dimensional coupled-mode theory we can treat the new mode intuitively as an anti-symmetrical combination of the coupled modes of the upper lateral rib waveguides and the mode of the underlying InP slab ARROW core [6]. Thus, the shape of the output mode depends strongly on the width of the lateral ribs. Fig. E.3 shows the confinement of the fiber-matched leaky mode in the QW's of the lateral ribs for the structure of Fig. E.2 as a function of the lateral rib width $l$ while keeping the gap $g$ constant and equal to 1 $\mu$m. This confinement should be minimized in order to reduce absorption loss in the unpumped lateral ribs. The field profiles for different widths $l$ are also shown for illustration. A flat

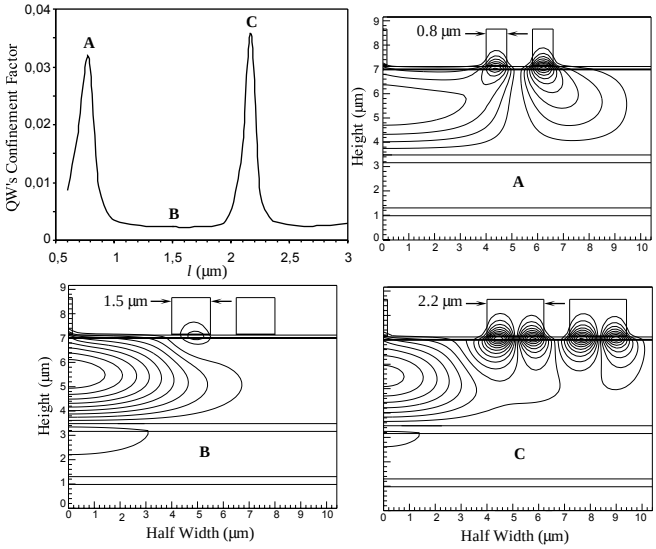


Figure E.3: Confinement of the output mode in the QW's of the active layer of a shallowly etched device as a function of the widths of the lateral ribs $l$, maintaining the gap $g$ between ribs constant. The field distributions of the modes at the points indicated in the graph are also shown.

and broad minimum confinement is found around $l = 1.5$ $\mu$m, where the output mode is fit for coupling to fiber. The broad minimum implies that the device is tolerant to fabrication errors. Two designs, with a different etch depth for the laser rib, are considered (shown as $E_1$, and $E_2$ in Fig. E.2) and the optimum width $l$ for the deeply etched device is also calculated and found to be 1.6 $\mu$m. In both etch options the optimum gap $g$ between lateral ribs is less than 1 $\mu$m, but has to be increased to 1 $\mu$m because of fabrication limitations. Fortunately, this does not change the modal shape significantly.

The evolution of the optical field as a function of the upper central rib is shown in Fig. E.4. As the active waveguide is tapered by reducing the ridge width from 3 to 0.3 $\mu$m, the mode couples adiabatically from the upper guide to the underlying ARROW waveguide (see Fig. E.4). The design of the lateral tapering is based on the adiabaticity of the mode transformation, and has been evaluated by means of a commercial 3-D eigenmode expansion algorithm based on a resonance method [7]. Low taper angles are needed for the range where the modal transformation is produced, in order to avoid radiation losses, while higher angles are allowed in the other regions. The adiabatic shape designs for both etching options have been approximated by a piecewise linear device consisting of three linear sections and are sketched in Fig. E.5. A minimum narrowing of 100 nm per 77 $\mu$m propagation length yields a safe design from the fabrication point of view. Both designs exhibit a calculated transformation loss of 1 dB.

When the mode is expanded in the shallowly etched device, it will be slightly

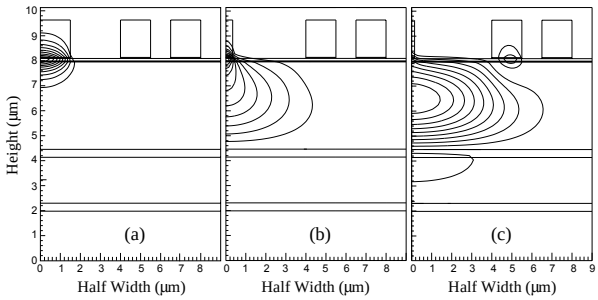


Figure E.4: Fundamental TE mode evolution along the taper structure of Fig. E.2 for (a) $w = 3$ $\mu$m, (b) $w = 0.9$ $\mu$m and (c) $w = 0.3$ $\mu$m. A shallow etch is simulated.

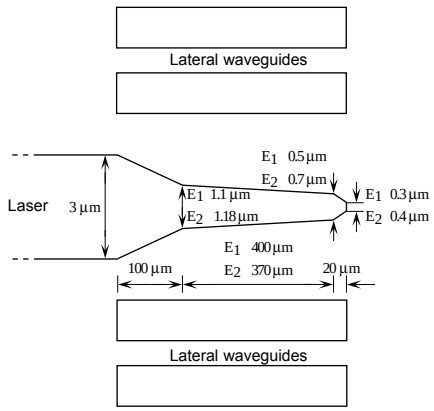


Figure E.5: The optimum taper shape is approximated by a piecewise linear device consisting of three linear sections. Tapers for both shallowly ($E_1$) and deeply ($E_2$) etched laser are designed.

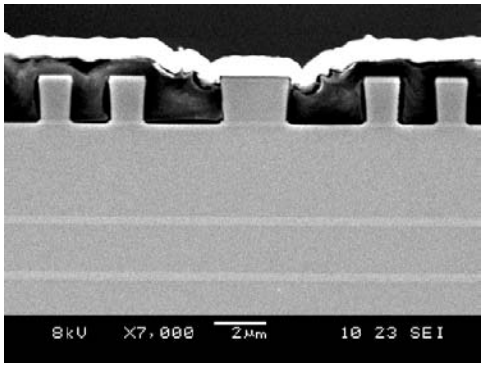


Figure E.6: SEM image of the laser cross-section, showing the electric contact over the central tapered rib, the good definition of the lateral ribs and the high index ARROW cladding layers.

confined in unpumped active quaternary layers [see Fig. E.4(c)]. This may introduce some absorption losses in the shallowly etched lasers that are not present in the deeply etched designs.

## E.4 Device Processing

The epitaxial layers were grown by metal organic chemical vapor deposition (MOCVD). By plasma etching we defined the SiOx pattern with conventional photoresist as a mask. The central and lateral ribs were etched by RIE to a depth 100 nm above the active layer. Next, a selective wet etch of the remaining InP down to the confinig layer of the active layer was carried out. This etch was done using $H_3PO_4$:HCl (7:3). Finally, an extra 40 nm (shallow etch) or 140 nm (deep etch) of RIE etching into the active layer was performed. Next, polyimide was spin-coated on the sample to form an insulation layer. The thickness of the polyimide is less on top of the ridges compared to the rest of the sample. Therefore, by a controlled plasma etch, the dielectric was removed on the ridge while dielectric coverage remained elsewhere resulting in good electric isolation [8]. SEM pictures of the taper (Fig. E.6) revealed that the metal contact over this upper ridge was good and that the thin ribs were fabricated reproducibly. Next, using a negative photoresist and a metal liftoff process, the metallization pattern was defined. Finally, the thinning of the substrate was done and the back contact was deposited. Arrays of devices, each with 520 $\mu$m long straight active sections, were mounted on electrically cooled copper heatsinks with silver epoxy and were tested without any coatings. The entire device is electrically pumped because the metallization also covers the entire length of the spot size converters. This can have a negative impact on the threshold current and efficiency, but on the other hand it avoids the risk of high absorption losses in the passive section of the taper. Untapered lasers 750 $\mu$m long and 3 $\mu$m wide and fabricated from

| Laser | $I_{th}$ (mA) | $\eta_d$ (W/A) | $L$ (μm) | $FC$ (dB) | $FF$ (Deg.) | *Tol.* (μm) |
|---|---|---|---|---|---|---|
| Reference, $E_1$ | 35 | 0.12 | 0 | –8 | 31.5×42.8 | ±1.6×±2 |
| Reference, $E_2$ | 28 | 0.12 | 0 | –8.3 | 30.7×40.6 | ±1.5×±2 |
| Tapered, $E_1$ | 55 | 0.1 | 520 | –4 | 13.8×30.8 | ±2.3×±2.4 |
| Tapered, $E_2$ | 48 | 0.12 | 490 | –4.3 | 13×32.7 | ±2.2×±2.3 |
| Variant 1 (Fig. E9) | – | – | 490 | –2.4 | 7.2×14 | ±2.3×±1.9 |
| Variant 2 (Fig. E10) | – | – | 270 | –1.1 | 7.2×9 | ±2.9×±2.3 |

Table E.1: Measurement and simulation results on the integrated mode expanded lasers considered in this work.

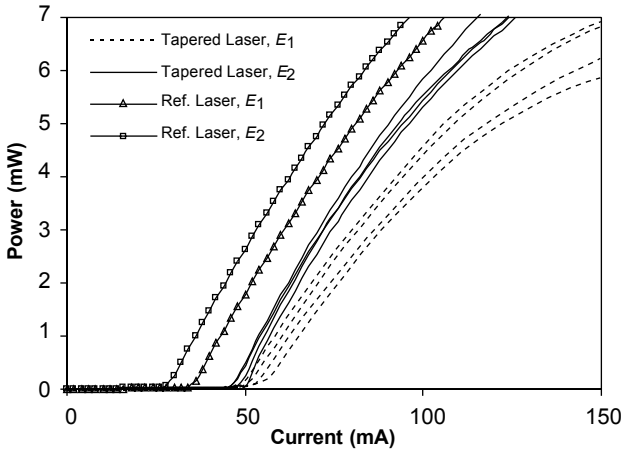


Figure E.7: $L$–$I$ characteristics of several shallowly ($E_1$) and deeply ($E_2$) etched mode-expanded and untapered reference lasers.

the same wafer as the tapered lasers were also prepared as a reference. Both reference and tapered lasers have a similar total active area.

## E.5 Results and Discussion

All the measured parameters are shown in Table E.1. The devices were operated in continuous wave (CW) operation. The room temperature light intensity versus current ($L$–$I$) curves of mode-expanded and untapered reference lasers are shown in Fig. E.7 for both etch depths. The deeply etched reference devices,

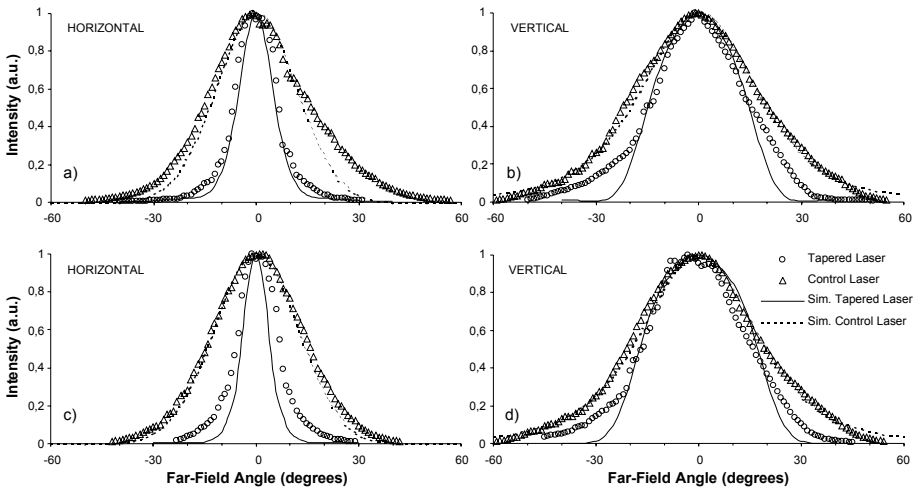


Figure E.8: Far-field emission patterns of tapered and untapered lasers. Shallowly etched lasers (a) lateral and (b) vertical. Deeply etched lasers (c) lateral and (d) vertical.

with a threshold current of 28 mA, present a better laser performance than the shallowly etched ones (35 mA). Fairly uniform threshold current distributions were found along the laser array.

Regarding the mode-expanded lasers, an increase of about 20 mA in the threshold current with respect to the reference lasers is found. This can be attributed to the mode transformation loss within the taper, to the losses in the $n$-doped thick InP ARROW core layer, and to the non-uniform pumping of the tapered active rib as a function of its width. The fact that the power of the tapered device is measured at the expanded mode facet, which has a lower reflection coefficient than the reference laser facet, influences positively in the external efficiency of the lasers. Nevertheless, the higher absorption loss in the unpumped QW's of the lateral ARROW rib waveguides for the shallowly etched devices [see Fig. E.4(c)] causes a decrease of the external efficiency of the laser from 0.12 W/A, for the reference lasers, to 0.1 W/A. This fact is not observed in the deeply etched devices that maintain the same external efficiency as the reference lasers.

Far-field emission patterns for both tapered and reference lasers were measured by using a rotating stage and a pinhole detector (see Fig. E.8). The theoretical curves obtained from the Fourier transform of the theoretical near fields are also overlaid in Fig. E.8, for comparison. The measured full width at half-maximum (FWHM) values are shown in Table E.1. A considerably lateral divergence improvement is achieved in the lateral direction for both groups of lasers, reaching a minimum of 13° for the deeply etched lasers. On the other hand, due to the not so thick ARROW slab core (3.5 $\mu$m), the achieved vertical

field divergence is still slightly higher than 30°, improving it by 10° with respect to the reference laser. A further improvement in the vertical far-field pattern could be obtained by thickening the ARROW core layer and defining more than two ribs on each side of the output ARROW waveguide in order to provide a good lateral confinement for thick cores.

A coupling efficiency measurement was performed between the expanded mode laser and a standard cleaved single mode fiber with a spot size of 10 $\mu$m at 1.55 $\mu$m. Maximum fiber coupling efficiencies of around $-4$ dB are obtained for both etch depths, including the Fresnel losses occurring at the air-glass interface. The improvement in the fiber coupling with respect to the untapered devices amounts up to 4 dB (see Table E.1). As the alignment tolerance with respect to the fiber depends on the large fiber mode, only slight improvements in the lateral direction are observed with respect to the reference untapered lasers. A maximum 1-dB alignment tolerance of $\pm 2.3$ (lat.)$\times \pm 2.4$ (vert.) is obtained for the shallowly etched devices. The fact that the vertical alignment tolerance is higher than the lateral value is due to the fact that the fiber facet was somewhat moved away from the taper output facet. These measurement restrictions were considered to avoid the contact of the fiber end with the laser output facet during the sweep of the transverse position of the fiber.

All the results are in good agreement with theoretical calculations.

## E.6 Variant 1: Weakly Guiding Fiber-Adapted Waveguide

The SSC concept proposed in this work has been demonstrated experimentally as discussed in the last section. Nevertheless, the waveguide structure of Fig. E.2 has a limitation on the vertical direction because the lateral ribs lose their confinement effect when the slab core becomes too thick. The structure of Fig. E.9 is similar to that of Fig. E.2 but it makes use of a thin weakly-guiding core of only 80 nm and buried in InP beneath the active layer. The mode at the active rib and the mode at the end of the tapering are also shown. The MQW gain in the straight section of the laser remains unalterable (see Fig. E.4(a) and E.9(a) for comparison). The fiber-matched mode presents a quite asymmetrical field distribution in the vertical direction, but the fact that its maximum is closer to the upper lateral couple of ribs strengthens their influence. Moreover, from a coupling and far-field point of view the typical exponential decay of weakly guiding waveguides induces an improvement of the coupling efficiency and FWHM of the output beam, in spite of its asymmetrical shape.

Simulation results on the propagation of this new structure are shown in Table E.1. Only the design for the deep etching through the QW's has been considered (see Fig. E.2) because of its better lasing performance. The same tapering sketched in Fig. E.5 has been simulated, because it also provides an adiabatic mode transformation for this new structure. We observe that the beam divergence angles and the coupling efficiency are improved to $7.2° \times 14°$ and $-2.4$ dB, respectively. Due to the vertically asymmetric modal shape, the

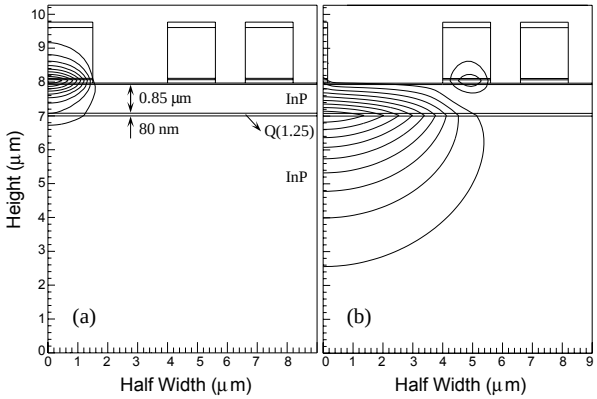


Figure E.9: Schematic structure of the SSC using a weakly guiding underlying slab waveguide. The active layer and upper rib waveguides are identical to that of Fig. E.2.

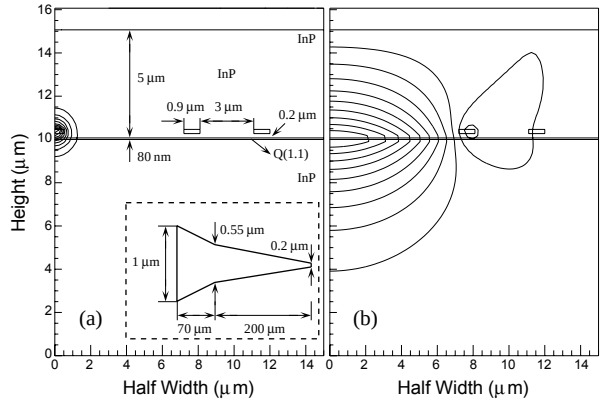


Figure E.10: Schematic structure of a buried variant of the proposed SSC concept. Higher and more efficient mode transformation efficiencies can be achieved in buried structures.

vertical alignment tolerance is slightly reduced to $\pm 1.9$ $\mu$m, while the lateral value is maintained.

## E.7 Variant 2: Buried Laser

The mode transformation concept proposed in the present work can also be integrated in a second variant, being a buried laser structure as shown in Fig. E.10. A buried 194 nm thick MQW active layer having an equivalent refractive in-

dex of 3.45 is tapered from 1 to 0.2 $\mu$m following the tapering shown in the inset of Fig. E.10(a). The slab waveguide core of quaternary compound with $\lambda_g = 1.1$ $\mu$m Q(1.1) is buried 0.2 $\mu$m beneath the active core and is 70 nm thick. The optimum lateral confinement ARROW ribs are 0.9 $\mu$m wide and are separated by 2 $\mu$m. All this is embedded under a 5 $\mu$m thick top layer of InP.

The fact that the tapered active central core is totally embedded in InP makes the mode transformation efficiency much higher for buried than for rib structures. This is the reason why the length of the buried SSC (270 $\mu$m) is much shorter than the rib SSC (490 $\mu$m).

Simulation results on the SSC propagation are shown in Table E.1. They show fiber butt coupling losses as low as 1.1 dB, beam divergence angles of $7.2° \times 9°$, and alignment tolerances of $\pm 2.9 \times \pm 2.3$ $\mu$m, compared to the 8.5 dB coupling loss and $29° \times 32°$ divergence angles of the untapered devices.

## E.8 Conclusion

In this paper we have presented a new concept for the fabrication of highly efficient and simple-to-fabricate SSC's that make use of the ARROW-concept for both the lateral and vertical optical confinement. InGaAsP–InP rib lasers with monolithically integrated SSC's have been demonstrated. The taper transforms the small active laser mode into the fiber-adapted mode of the underlying slab ARROW waveguide. The lateral confinement of the slab mode is achieved by means of an antiresonant effect provided by two sets of lateral rib waveguides defined in the same etch process as the central active ridge. Therefore, only a single planar growth step and a single conventional etching process are required, leading to the simplest SSC concept ever reported. Threshold currents of around 50 mA were measured, which have to be compared with 30 mA for untapered lasers. The far-field FWHM divergence angles were significantly reduced and 4 dB improvement of the coupling efficiency to single mode fiber was observed.

Two variants of the demonstrated concept have also been analyzed by simulation and are expected to show a better performance. In a first variant a weakly-guiding slab waveguide substitutes the thicker slab core of the first structure. In a second variant the SSC concept of this work is integrated in a buried laser structure. Simulation results show considerable improvements in the far-field divergence angles and fiber-coupling efficiencies.

## References

[1] I. Moerman, P. Van Daele, and P. M. Demeester, "A review on fabrication technologies for the monolithic integration of tapers with III-V semiconductor devices," *IEEE J. Select. Topics Quantum Electron.*, vol. 3, pp. 1308–1320, Dec. 1997.

[2] I. V. Golster, L. J. Mawst, and D. Botez, "Single-cladding antiresonant reflecting optical waveguide-type diode laser," *Opt. Lett.*, vol. 20, pp. 2219–

2221, Nov. 1995.

[3] M. Galarza, K. De Mesel, R. Baets, and M. Lopez-Amo, "Modelling of InGaAsP–InP 1.55 $\mu$m lasers with integrated mode expanders using fiber-matched antiresonant reflecting optical waveguides," in *Proc. Eur. Conf. Integrated Optics (ECIO '01)*, Paderborn, Germany, pp. 421–424.

[4] J. M. Kubica, "Numerical analysis of InP/InGaAsP ARROW waveguides using transfer matrix approach," *IEEE J. Lightwave Technol.*, vol. 10, pp. 767–771, Jun. 1992.

[5] M. Galarza, K. De Mesel, D. Fuentes, R. Baets, and M. Lopez-Amo, "Modelling of InGaAsP–InP 1.55 $\mu$m lasers with integrated mode expanders using fiber-matched leaky waveguides," *Appl. Phys. B-Lasers Opt.*, vol. B 73, pp. 585–588, Oct. 2001.

[6] G. R. Hadley, "Two-dimensional coupled-mode theory for modeling leaky-mode arrays," *Opt. Lett.*, vol. 15, pp. 27–29, Jan. 1990.

[7] A. S. Sudbo, "Numerically stable formulation of the transverse resonance method for mode-field calculations in dielectric waveguides," *IEEE Photon. Technol. Lett.*, vol. 5, pp. 342–344, Mar. 1993.

[8] V. Vusirikala, S. S. Saini, R. E. Bartolo, S. Agarwala, R. D. Whaley, F. G. Johnson, D. R. Stone, and M. Dagenais, "1.55-$\mu$m InGaAsP–InP laser arrays with integrated-mode expanders fabricated using a single epitaxial growth," *IEEE J. Select. Topics Quantum Electron.*, vol. 3, pp. 1332–1343, Dec. 1997.

## Publication F

# Compact Spot-Size Converters Using Fiber-Matched Antiresonant Reflecting Optical Waveguides

M. Galarza, K. De Mesel, A. Martínez, C. Aramburu, M. López-Amo, and R. Baets

*Applied Optics*, Submitted for publication, Nov. 2002.

***Abstract***—We propose a new concept for InGaAsP-InP 1.55 $\mu$m lasers integrated with spot-size converters based on modal interference between the modes of the structure formed by an active waveguide and an underlying fiber-matched ARROW waveguide. Simulation results show that the spot-size converters exhibit low transformation loss, narrowed far-field emission patterns ($10° \times 20°$) and reduce the coupling loss to standard single-mode fibers from 8 dB to 2.6 dB over lengths about 200 $\mu$m shorter than the adiabatic concept. A tolerant design to fabrication variations is also proposed, which could be realized using standard processing techniques.

## F.1 Introduction

The function of integrated spot-size converter (SSC's) is to enlarge and reshape the small and asymmetric mode of a III-V semiconductor waveguide component to a large and circular mode that is better adapted to the fiber or (in case of hybrid integration) the silica waveguide [1]. In this way, it provides high coupling efficiencies and large alignment tolerances that enable the use of passive alignment schemes that drastically reduce the packaging cost. The use of microlenses or tapered/lensed fibers [2] that image one mode onto the other is an alternative solution that also improves the coupling loss, but at the expense of the alignment tolerances, which are then in the submicron range.

Over the past ten years much research has focused on the integration of mode size converters with waveguide components in order to improve the coupling efficiency. Most of these approaches involve complex growth and/or processing steps, requiring extensive process development. Nevertheless, there is one group of devices that is particularly interesting since it only requires a single standard planar epitaxial growth step and conventional lithography and etching processes [3]–[5]. These devices incorporate a large fiber-matched rib waveguide that operates close to cutoff. In InP technology this involves the growth of quaternary materials exhibiting a slightly higher refractive index than the InP-substrate.

These low-refractive indexes are achieved by means of low Ga- and As-fraction quaternary materials, which are difficult to grow. This problem was solved in [6], by introducing a diluted structure.

We have demonstrated an alternative solution in recent work [7], where the thick quaternary layer is replaced by an easy-to-grow InP layer in an ARROW configuration [8], [9]. In the tapered 1.55 $\mu$m laser presented in [7], a laser rib is laterally tapered so that its guided mode is transformed into the fundamental mode of the fiber-matched ARROW waveguide over a length long enough to ensure minimum mode transformation losses. In this paper, we propose an approach for 1.55-$\mu$m mode-expanded lasers based on modal interference between the two supermodes supported by the taper structure formed by the laser rib waveguide and the fiber-matched ARROW waveguide [10], [11]. This concept provides the same performance and mode transformation loss as the adiabatic approach [7], but over a considerably shorter length. Section F.2 of this paper presents the concept for compact spot-size converters. In Section F.3, the waveguide structure and taper design are outlined. In Section F.4 we present the simulation results on mode transformation and fiber-coupling efficiency, as well as a tolerance analysis to width and etching depth variations. In order to relax the fabrication of such devices a tolerant design is carried out in Section F.5. Section F.6 finally summarizes and concludes this work.

## F.2 Concept

Fig. F.1(a) shows a simplified two dimensional representation of the adiabatic mode transformation produced in a double core rib taper (the lateral tapering of the real SSC's is shown as a vertical tapering in the figure for clarity purposes). The mode generated in the upper active waveguide is in fact the even supermode $\psi_e$ of the complete structure formed by the active and the lower fiber-matched passive waveguides. In an adiabatic taper this mode carries all the power while it is being transformed and expanded. The odd supermode $\psi_o$ supported by the structure is shown in Fig. F.1(b) for the same taper. This mode is not excited in the adiabatic regime and when the tapered upper rib waveguide reaches cut-off due to the tapering, this mode is not a guided mode any more and becomes a radiation mode.

The mode transformation concept based on the bimodal interference between the two guided supermodes of the taper structure is schematically shown in Fig. F.2. The taper has been drawn twice, one for each supermode, for clarity. Region $A$ represents the mode generated in the straight laser $\psi_e$. In region $B$, an abrupt tapering of the waveguide provokes the transfer of power from this fundamental even mode to the odd mode $\psi_o$ of the structure. In the straight section of region $C$ the two modes propagate without loss and interfere. At the beginning of region $C$ the field is concentrated in the upper active waveguide, but when the supermodes reach the coupling length (when their phase difference $\Delta\phi = \pi$), the field spreads considerably in the lower passive waveguide. In the last section of the taper (region $D$) two relevant phenomena occur. The

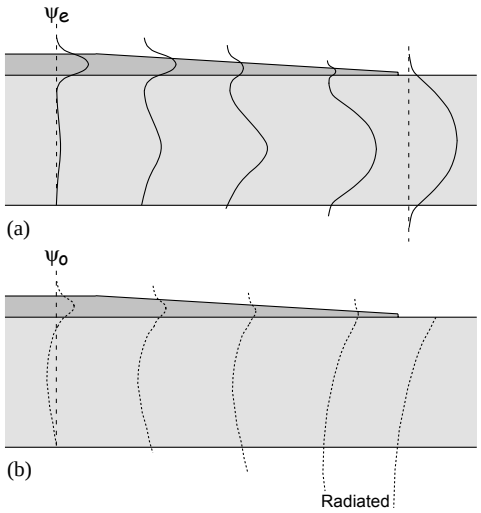


Figure F.1: In the adiabatic mode transformation concept, (a) the even supermode of the taper $\psi_e$ is smoothly transformed into the passive broad mode without loosing any power, and (b) the odd supermode $\psi_o$, which is not excited during the transformation, becomes a radiation mode.

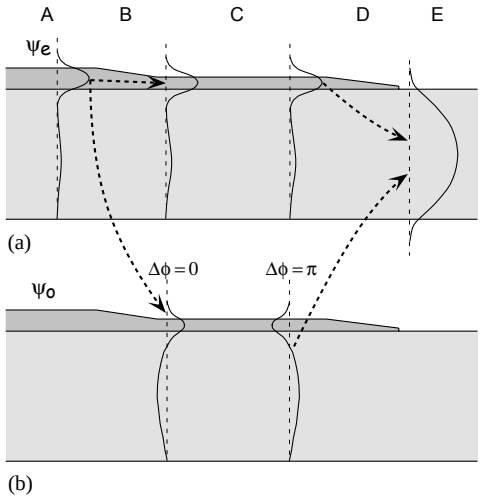


Figure F.2: Bimodal interference taper concept. (a) The fundamental supermode $\psi_e$ transfers power to (b) the odd one $\psi_o$ and the interference between them spreads the field in the fiber-matched waveguide. In the final section, the power couples back to the fundamental mode of the taper.

even mode $\psi_e$ is transformed into the fundamental mode of the underlying fiber-matched waveguide (region $E$); and the power carried by $\psi_o$ is transferred to $\psi_e$ before it becomes a radiation mode.

The technique used to transfer power from the even eigenmode $\psi_e$ to the odd one $\psi_o$ can be understood by the adiabaticity criteria described in [12] that is developed to design tapered single-mode devices. In the classical equation in the coupled mode theory it is assumed that the transfer of power from the fundamental mode of a taper will be predominantly to the higher order mode with a propagation constant closest to that of the fundamental mode. In the cases we are considering this power-receiving mode is the odd supermode $\psi_o$. Therefore, using slopes that are beyond the critical slope in region $B$ and $D$ we force the power transfer between the fundamental even mode $\psi_e$ and the odd mode $\psi_o$. However, if the slope of this tapering is too sharp we will have undesired radiation to higher order radiation modes that decrease the taper efficiency; thus a compromise between intermodal power transfer and taper efficiency has to be found. Fig. F.3 shows the shape of the lateral tapering of a taper based on bimodal interference. The two abrupt tapers provide the power transfer between the supermodes and in the central straight section the modal interference is produced.

In previous theoretical works [10], [13] the authors do not consider the influence of the underlying slab waveguide in the calculation of the mode of the laser waveguide and they just use a transition of waveguides to excite the two supermodes of the taper structure that induces the power transfer form the upper to the lower waveguide. However, although they do not mention it, this approach could not be used on structures grown on the same wafer and defined using standard processing techniques because the underlying slab core is everywhere on the wafer influencing the shape of the laser mode.

In [11] the authors make use of the modal interference to reduce the length of the SSC, but they do not give a theoretical explanation of the technique they use to excite the odd supermode of a rib structure similar to the structures considered in this work.

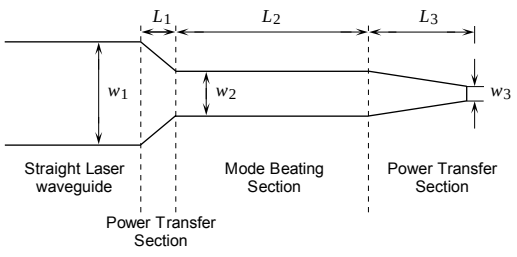


Figure F.3: Shape of the lateral tapering in a compact taper based on modal interference.

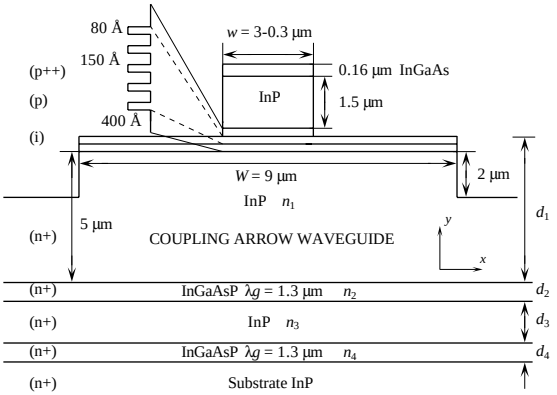


Figure F.4: Schematic drawing of the mode-expanded laser showing the tapered upper active rib and the underlying fiber-matched ARROW waveguide.

## F.3 Design

### F.3.1 Waveguide Structure

The transverse structure of the proposed mode-expanded laser is shown in Fig. F.4 and is identical to the one used in [7], [14] for the adiabatic design. The device consists of an active multi-quantum well rib waveguide that is laterally tapered from 3 to 0.3 $\mu$m. It contains five 1 % compressively strained 80 Å-thick $In_{0.78}Ga_{0.22}As_{0.79}P_{0.21}$ wells for emission at 1.55 $\mu$m, and four lattice-matched 150 Å-thick $In_{0.75}Ga_{0.25}As_{0.54}P_{0.46}$ barriers, surrounded by 400 Å-thick undoped confining layers having the same composition as the barriers.

The underlying rib waveguide is optimized for coupling to an optical fiber. The vertical confinement of this fiber-matched mode is achieved by means of an ARROW geometry that consists of a 5-$\mu$m thick InP core layer and an interference cladding system formed by two high index cladding layers made of quaternary material and a separating InP film. This structure supports a certain number of bound modes in the high index claddings and several leaky modes. The fundamental leaky mode is confined in the lower index InP core layer and propagates with very low loss. Considering the ray model we can treat it as a case where light coupled into the core undergoes total internal reflection at the upper surface and very high reflections from the sequence of antiresonant Fabry-Pérot resonators formed by the InP-InGaAsP interfaces. The relaxed ARROW cladding structure demonstrated in [7] used for simulations in this work provides a considerable thin cladding structure ($d_{2,4} = 0.31$ $\mu$m, $d_3 = 0.5$ $\mu$m), while keeping the leakage losses of the fundamental ARROW mode negligibly low. We refer to [7], [14] for design details.

Fig. F.5 shows the two 2D supermodes supported by the taper structure considered in this work and for a width of the active rib of 0.92 $\mu$m.

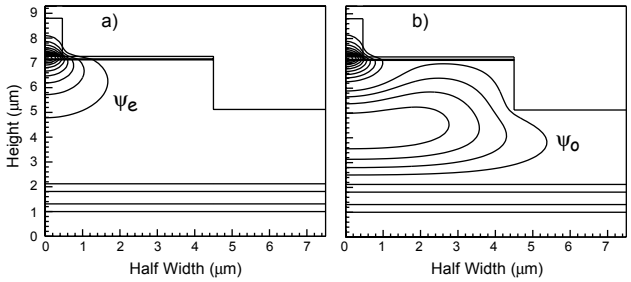


Figure F.5: (a) Even and (b) odd supermodes supported by the taper structure.

### F.3.2 Taper Design

Commercial three-dimensional beam propagation method (3-D BPM) software (BPM_CAD, Optiwave Corporation) was used to design and analyze the proposed compact mode expanders. The most important and critical section to be designed is the first abrupt tapering (defined by $w_1$, $w_2$, $L_1$) where the power transfer takes place. The initial width $w_1$ is defined by the width of the laser straight section, which is 3 $\mu$m. Therefore, the length $L_1$ and the final width $w_2$ of the sharp tapering have to be chosen. Using BPM, the shape schematized in Fig. F.6(a) was simulated for different values of these parameters. The central width $w_2$ was swept from 0.84 to 0.94 $\mu$m in steps of 0.02 $\mu$m and the length $L_1$ from 20 to 40 $\mu$m in steps of 5 $\mu$m. Two different regimes where observed as a function of $w_2$, while no influence of $L_1$ was noticed. For widths $w_2$ larger than 0.88 $\mu$m the field smoothly goes down, spreads in the lower waveguide at the beat length, and goes up again repeating this behavior periodically (see Fig. F.6(b)). Moreover, the light power in the simulation window at the end of the propagation reaches 90 % of the input power, demonstrating efficient excitement of $\psi_o$. However, for widths smaller than 0.88 $\mu$m, high excitement of radiation modes is produced and the spreading of light due to modal interference is lost. From this first design step, we choose $w_2 = 0.92$ $\mu$m and $L_2 = 143$ $\mu$m. A narrower width could have too low fabrication tolerances and a wider width could avoid an extensive broadening of light. As the length of the first section did not influence the performance of the resonant taper, we chose a short $L_1 = 20$ $\mu$m.

The final parameter that must be designed is the length of the last section $L_3$ where the width is tapered until the active waveguide reaches cut-off ($w_3 = 0.3$ $\mu$m). Fig. F.7 shows the mode transformation loss and the fiber coupling loss of the taper to a cleaved single mode fiber as a function of $L_3$. We observe that the transformation loss decreases for increasing lengths of $L_3$, but that the fiber coupling loss is quite stable. We chose $L_3 = 100$ $\mu$m for the design leading to 1 dB mode transformation loss, the same loss the adiabatic mode expanders exhibited in [7]. The final design of the compact mode expanders using vertical ARROW fiber-matched waveguides is shown in Fig. F.8. The total length is 263 $\mu$m. A length reduction of 207 $\mu$m has been achieved compared

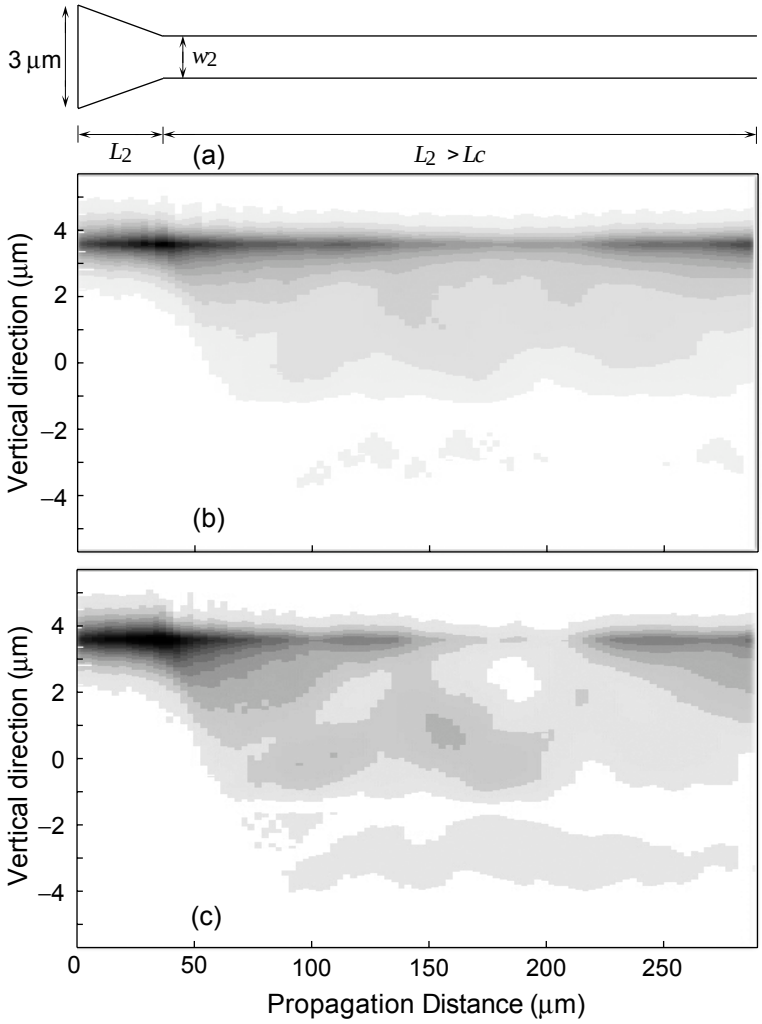


Figure F.6: Field distribution as a function of the distance for the taper shape shown in (a).(b) $w_2 = 0.92$ $\mu$m, (c) $w_2 = 0.86$ $\mu$m. In both cases $L_1 = 40$ $\mu$m.

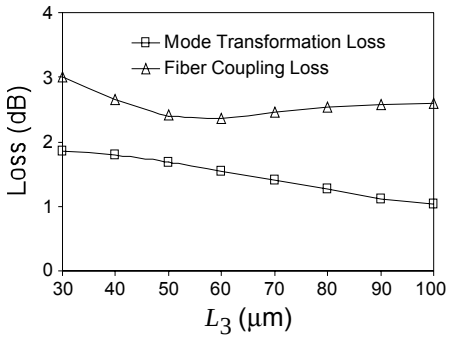


Figure F.7: Mode transformation and fiber-coupling loss as a function of $L_3$. $L_1 = 20$ $\mu$m, $L_2 = 143$ $\mu$m, $w_2 = 0.92$ $\mu$m, $w_3 = 0.3$ $\mu$m.

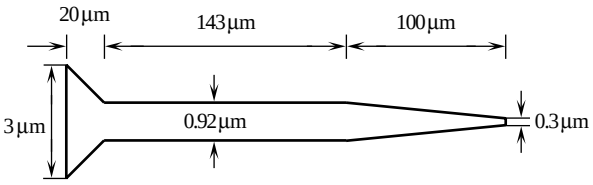


Figure F.8: Compact taper shape.

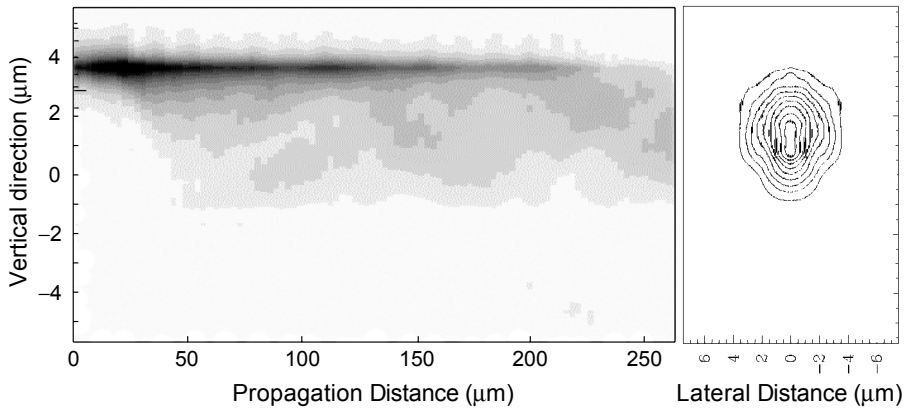


Figure F.9: Transverse plot of the propagating field and intensity plot of the fiber-matched output mode.

to the adiabatic method [7], which required 470 $\mu$m to reach a similar mode transformation loss.

## F.4 Simulation Results

Fig. F.9 shows the transverse plot of the field spreading along the taper, as well as the intensity plot of the output ARROW mode. Semivectorial (TE) calculations were used for propagation. Butt-coupling efficiencies to a standard single mode fiber of $-2.6$ dB are found (see Fig. F.7). Full width at half maximum (FWHM) divergence angles of 10° (lat.) $\times$ 20° (vert.) were obtained. All these results are in good agreement with the measured values for the mode expanders in adiabatic configuration [7].

As the performance of the compact mode expander depends strongly on the width of the straight waveguide section, a deep tolerance analysis is mandatory. We have investigated the influence of changes in the width $\Delta w$ and the etching depth $\Delta e$ of the active region. The results are shown in Fig. F.10. If the efficiency is taken as a figure of merit in this analysis we obtain a 3-dB tolerance of $\Delta w = \pm 55$ nm and $\Delta e = \pm 30$ nm. Unfortunately, these values are rather low considering the fabrication tolerances of standard growth and processing techniques.

## F.5 Tolerant Design

It is expected that by applying a slight slope to the central (and previously straight) section $L_2$ and defining it somewhat longer, the tolerances to fabrication variations will improve. The slope of this central section must be steep

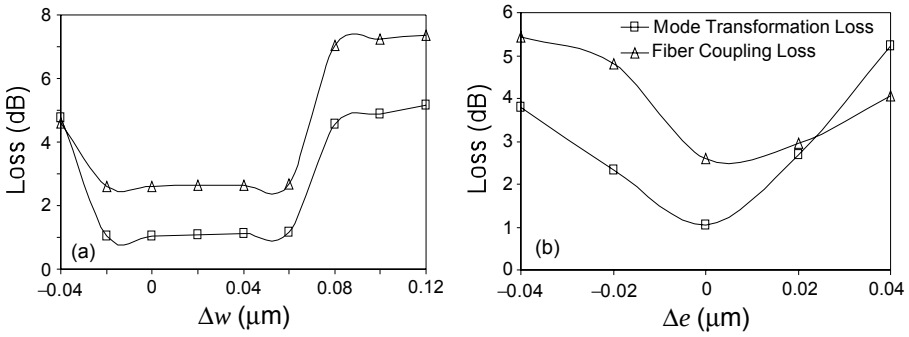


Figure F.10: Mode transformation and fiber-coupling loss as a function of variations in (a) the width of the taper $\Delta w$, and (b) the etching depth of the laser rib $\Delta e$.

enough in order to overcome the fabrication minimum slope, which we considered as 90 nm/100 $\mu$m. The initial and final widths of the central section, as well as the rest of the parameters, are carefully chosen by simulation. Fig. F.11 shows the resulting tolerant design that provides the reference 1-dB mode transformation loss. The new beat length turned out to be 173 $\mu$m, only 30 $\mu$m longer than for the previous straight case, while $L_1$ and $L_3$ do not change.

The simulation of the propagation provides the field distribution in a transversal cut shown in Fig. F.12. A smooth and continuous mode transformation is observed. The intensity plot of the broad mode is shown as well. The same fiber-coupling efficiency and far-field divergence angles as in the straight design are obtained.

The results on the tolerance analysis are shown in Fig. F.13. The tolerance ranges in width and etching depth are $\Delta w > \pm 125$ nm and $\Delta e > \pm 40$ nm, respectively. These values are higher than the standard fabrication tolerances. Regarding the length, the tolerant design is still 177 $\mu$m shorter than the adiabatic taper that provided the same mode transformation efficiency.

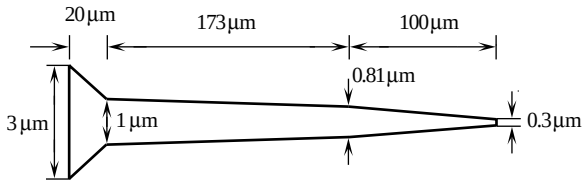


Figure F.11: Taper shape presenting a smooth slope in the mode beating section.

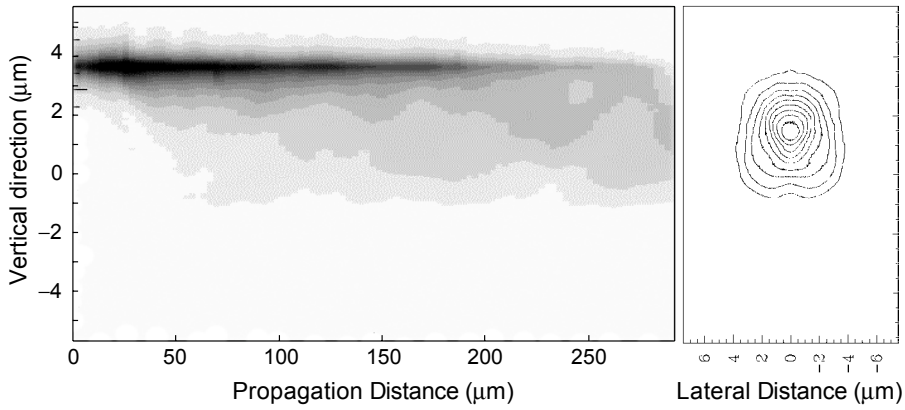


Figure F.12: Transverse plot of the propagating field and intensity plot of the fiber-matched output mode in the tolerant mode expander.

## F.6 Conclusion

In this work, we have presented mode expanders based on modal interference between the supermodes in the taper structure formed by an active rib waveguide and an underlying fiber-matched ARROW waveguide. Low-loss mode transformation and good fiber-coupling efficiencies and far-field divergence angles were obtained for much shorter lengths as compared to adiabatic tapers. Simulations show that applying a smooth slope to the mode beating section of the taper results in tolerant designs to variations in waveguide widths and etching depths.

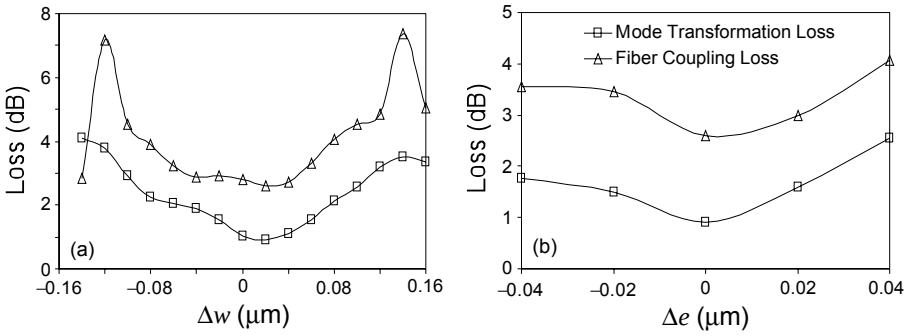


Figure F.13: Tolerance analysis results for the tolerant design.

## References

[1] I. Moerman, P. Van Daele, and P. M. Demeester, "A review on fabrication technologies for the monolithic integration of tapers with III-V semiconductor devices," *IEEE J. Select. Topics Quantum Electron.*, vol. 3, pp. 1308–1320, Dec. 1997.

[2] T. Alder, A. Stöhr, R. Heinzelmann, and D. Jäger, "High-efficiency fiber-to-chip coupling using low-loss tapered single-mode fiber," *IEEE Photon. Technol. Lett.*, vol. 12, pp. 1016–1018, Aug. 2000.

[3] S. S. Saini, F. G. Johnson, D. R. Stone, H. Shen, W. Zhou, and M. Dagenais, "Passive active resonant coupler (PARC) platform with mode expander," *IEEE Photon. Technol. Lett.*, vol. 12, pp. 1025–1027, Aug. 2000.

[4] G. A. Vawter, A. T. Sullivan, J. R. Wendt, R. E. Smith, H. Q. Hou, and J. F. Klem, "Tapered rib adiabatic following fiber couplers in etched GaAs materials for monolithic spot-size transformation," *IEEE J. Select. Topics Quantum Electron.*, vol. 3, pp. 1361–1371, Dec. 1997.

[5] K. De Mesel, R. Baets, C. Sys, S. Verstuyft, I. Moerman, and P. Van Daele, "First demonstration of a 980 nm oxide confined laser with integrated spot size converter," *Electron. Lett.*, vol. 36, pp. 1028–1029, Jun. 2000.

[6] V. Vusirikala, S. S. Saini, R. E. Bartolo, S. Agarwala, R. D. Whaley, F. G. Johnson, D. R. Stone, and M. Dagenais, "1.55-$\mu$m InGaAsP-InP laser arrays with integrated-mode expanders fabricated using a single epitaxial growth," *IEEE J. Select. Topics Quantum Electron.*, vol. 3, pp. 1332–1343, Dec. 1997.

[7] M. Galarza, K. De Mesel, S. Verstuyft, D. Fuentes, C. Aramburu, M. López-Amo, I. Moerman, P. Van Daele, and R. Baets, "Mode-Expanded 1.55 $\mu$m InP-InGaAsP Fabry-Pérot Lasers Using ARROW Waveguides for Efficient Fiber Coupling," *IEEE J. Select. Topics Quantum Electron.*, Accepted for publication.

[8] M. A. Duguay, Y. Kokubun, T. L. Koch, and L. Pfeiffer, "Antiresonant reflecting optical waveguides in $SiO_2$-Si multilayer structures," *Appl. Phys. Lett.*, vol. 49, pp. 13–15, Jul. 1986.

[9] T. L. Koch, U. Koren, G. D. Boyd, P. J. Corvini, and M. A. Duguay, "Antiresonant reflecting optical waveguides for III-V integrated optics," *Electron. Lett.*, vol. 23, pp. 244–245, Feb. 1987.

[10] B. M. A. Rahman, M. Rajarajan, T. Wongchaeron, and K. T. V. Grattan, "Improved laser-fiber coupling by using spot-size transformers," *IEEE Photon. Technol. Lett.*, vol. 8, pp. 557–559, Apr. 1996.

[11] V. Vusirikala, S. S. Saini, R. E. Bartolo, M. Dagenais, and D. R. Stone, "Compact mode expanders using resonant coupling between a tapered active region and an underlying coupling waveguide," *IEEE Photon. Technol. Lett.*, vol. 10, pp. 203–205, Feb. 1998.

[12] J. D. Love, W. M. Henry, W. J. Stewart, R. J. Black, S. Lacroix, and F. Gonthier, "Tapered single-mode fibers and devices. Part 1: Adiabaticity criteria," *IEE Proc.-J*, vol. 138, pp. 343–354, Oct. 1991.

[13] T. Wongchaeron, B. M. A. Rahman, R. Rajarajan, and K. T. V. Grattan, "Spot-size conversion using uniform waveguide sections for efficient laser-fiber coupling," *J. Lightwave Technol.*, vol. 19, pp. 708–716, May 2001.

[14] M. Galarza, K. De Mesel, D. Fuentes, R. Baets, M. Lopez-Amo, "Modeling of InGaAsP-InP 1.55 $\mu$m lasers with integrated mode expanders using fiber matched leaky waveguides," *Appl. Phys. B-Lasers Opt.*, vol. 73, pp. 585–588, Oct. 2001.

## Publication G

# Simple Low-Loss Waveguide Bends Using ARROW Effect

M. Galarza, K. De Mesel, I. Christiaens, C. Aramburu, M. López-Amo, and R. Baets

*Optics Letters*, Submitted for publication, Nov. 2002.

***Abstract***—A new concept for reducing bend loss in dielectric planar waveguides is presented. It is based on the introduction of a set of antiresonant reflecting optical waveguides (ARROW) on the outside of the bent core and defined in the same fabrication step as the main bend. It has been ascertained by simulation that the bending loss can be significantly reduced.

Curved waveguides are key components in photonic integrated circuits and are mainly used to change the direction of light or to introduce a lateral displacement. In order to achieve a high packing density in limited chip areas, it is mandatory to minimize bend radius as much a possible, without introducing significant bend loss. Unfortunately, bend loss increases almost exponentially with decreasing radius of curvature.

There exist three major methods for reducing bend loss. One method is the introduction of refractive index changes in order to increase the relative index difference between the core and the cladding [1] or to accelerate the phase fronts at the outer side of the bend [2]. A second method replaces the bend by a coherently coupled multisection bend to reduce the loss [3]. The introduction of an isolation trench [4], corner mirror [5] or outrigger waveguide of higher refractive index [6] on the outside of the bent core decreases the evanescent modal field more rapidly in the region between the waveguide core and the apparent origin of radiation, so that radiation loss is also reduced. Nevertheless, most of these strategies involve additional processing steps during fabrication or cumbersome designs.

In this paper, we propose a novel and straightforward technique that has the advantage that it does not require any extra processing step. Fig. G.1 shows a bend structure with a set of $N$ concentric waveguides on its outer side and defined in the same step as the main bend. They are designed to provide antiresonant reflection to the radiated light in a typical ARROW (antiresonant reflecting optical waveguide) configuration [7].

Fig. G.2 shows the concept simplified to a two-dimensional (2-D) geometry using the effective index method. A ray radiated from the bend will undergo multiple reflection at each interface defined by the ARROW structure, which

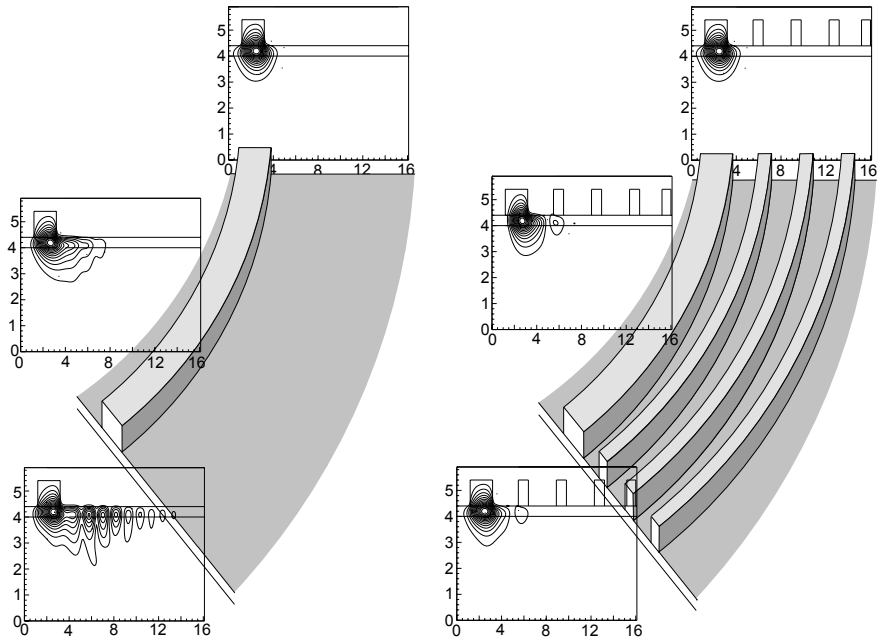


(a) (b)

Figure G.1: (a) Field distribution in a curved InP ridge waveguide. The radius of curvature is 160 $\mu$m and therefore, strong leakage can be observed at a distance of propagation of only 50 $\mu$m. (b) The same bend does not lose so much light power if a set of antiresonant ARROW waveguides are defined in the outer side of the bend.

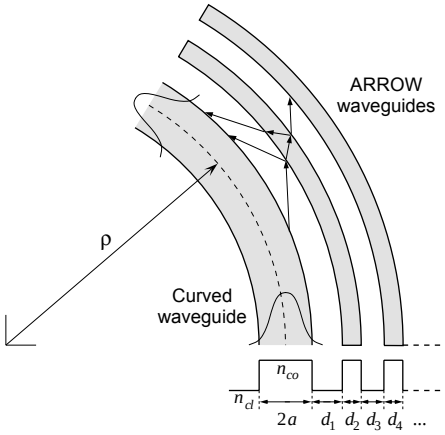


Figure G.2: Schematic drawing of the proposed bend concept.

under appropriate design, provides the same phase to the rays coming back to the curved waveguide.

By the conformal transformation $W = \rho \ln(Z/\rho)$ we transform the step-wise constant refractive index profile of the 2-D circular geometry $(\rho, \varphi)$ to an exponential refractive index profile in a straight geometry $(u, v)$ in order to simplify the design [8]. Fig. G.3 shows the equivalent structure in the $(u, v)$ plane. We see the oblique path defined by the rays that is due to the exponentially increasing refractive index. If we consider as a starting design value the angle $\theta_0$ (see

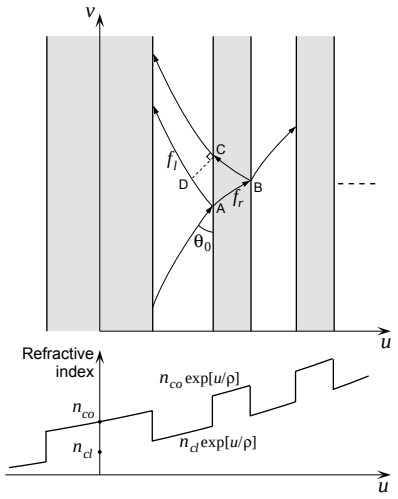


Figure G.3: Equivalent straight waveguide and modified index profile.

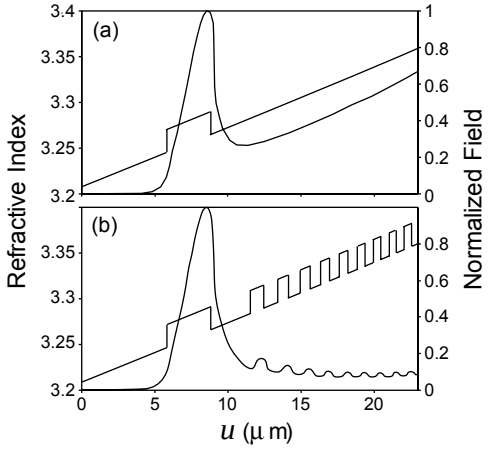


Figure G.4: Magnitude of the electric field in (a) standard InP bend waveguide and (b) same bend with 9 lateral ARROW waveguides ($\rho = 500$ $\mu$m).

Fig. G.3), defined by a radiated ray when reaching the first ARROW interface, it is straightforward to calculate the ray paths $f_l$ and $f_r$ defined in each medium using Snell's law (see Fig. G.3). Then, emulating the ARROW design theory for multilayer structures of step-wise constant index, the antiresonant condition of each lateral waveguide or gap $d_j$ is numerically calculated from:

$$k_0 \left( 2 \int_{\mathrm{A}}^{\mathrm{B}} f_r(u) n(u) \mathrm{d}u - \int_{\mathrm{A}}^{\mathrm{D}} f_l(u) n(u) \mathrm{d}u \right) + \pi = 2M\pi \qquad (M = 0, 1, 2 \ldots) \tag{G.1}$$

where $k_0$ is the wavenumber in vacuum, $f_l(u)$ and $f_r(u)$ are the path described by two adjacent rays in the mediums of both sides of the interface, $n(u)$ is the exponential equivalent refractive index distribution, and A, B, C and D are the points indicated in Fig. G.3. A small error is introduced using this analysis because, due to the curve, a mismatch in the travelling direction of two adjacent rays is produced. This error will be bigger for smaller radius, but the simple design in (G.1) remains valid for practical applications because of the typical flat and wide response of antiresonant structures.

To quantify the improvement achieved with this concept, we used a numerical simulation based on eigenmode expansion and perfectly matched layers [9]. For a first example, we assume a typical InP/InGaAsP step-profile waveguide with core index $n_{co} = 3.279$ , cladding index $n_{cl} = 3.254$, core half-width $a = 1.5$ $\mu$m, and operating wavelength $\lambda = 1.55$ $\mu$m.

Fig. G.4(a) shows the magnitude of the electric field for transverse magnetic (TM) polarization, together with the transformed index profile of a standard bend. Fig. G.4(b) shows the corresponding ARROW bend with $N = 9$ lateral waveguides. The radius of the main bend is 500 $\mu$m. It is clearly visible that

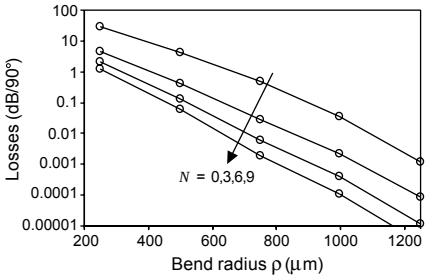


Figure G.5: Bending loss per 90° as a function of bend radius and number of lateral waveguides for the InP structure.

the standard mode leaks a lot more power to the outside of the bend (right side of the figure), and that it better matches the symmetric mode of the straight waveguide, also leading to lower transition losses.

Fig. G.5 shows the calculated radiation losses of the waveguide, as a function of bending radius $\rho$ and number of lateral ARROW waveguides $N$. TM polarization has been chosen because the ARROW effect is less efficient than for TE polarization and, therefore, the worst case is considered. We have observed that the optimum design is not very dependent on the width of the first gap $d_1$ and that this parameter can be chosen from the point where the radiation due to the bending is located. An analytical analysis is outlined in [10] from which this parameter is easily calculated. For the optimization of the first incidence angle $\theta_0$, a sweep has to be done to obtain the minimum loss point. We observe from Fig. G.5 that the loss in dB is reduced by a factor of 10 using only 3 lateral ribs, and that this loss still decreases approximately another factor of 10 using 9 lateral ribs. The improvement factor is higher for big radii than for small ones. From the integration area point of view, we observe that for a certain loss it would be possible to reduce the radius of the bend by a factor of 2, which means that the area can be reduced by a factor of 4. Naturally, the reduction ratio could still be increased defining more than 9 lateral ribs.

As mentioned above, the simulated designs were optimized for TM polarization. Propagating a TE mode over a sharp ARROW bend with a radius $\rho = 250$ $\mu$m and optimized for TM polarization provides a loss of 7.3 dB/90° whereas the optimum TE design provides 6.6 dB/90°. Naturally, even lower influence can be expected for more practical radii and loss range. This fact shows the polarization independence of these new bend structures.

The tolerance for changes in etch-depth of the ribs has also been studied. We have observed that variations of $\pm$100 nm in the etching depth of the considered rib waveguide decrease the optimum bend loss in less than 1 dB. This fact means that the ARROW bend concept is also very tolerant to variations in the etching depth of rib waveguides.

The performance of ARROW bends as a function of variations in the width of the lateral ribs has also been studied. It is very common to have this kind of

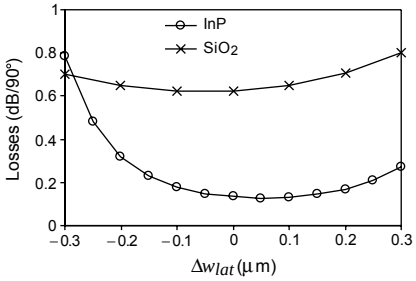


Figure G.6: Calculated loss as a function of general variation in the widths of the lateral ARROW waveguides.

variations during the processing of the devices. Fig. G.6 shows the calculated radiation losses of an ARROW bend structure having a radius $\rho = 500$ $\mu$m and $N = 6$ lateral ribs as a function of a general variation in the widths of the lateral ribs. We observe a smooth increase of the loss by less than 1 dB in a safe lithographic range of $\pm 0.3$ $\mu$m.

As a second example we consider a silica-on-silicon waveguide with effective core index $n_{co} = 1.452$, cladding index $n_{cl} = 1.444$, core half-width $a = 2.75$ $\mu$m, and operating wavelength $\lambda = 1.55$ $\mu$m. The required high bending radius due to a low index contrast, is the main disadvantage of silica-on-silicon technology. Fig. G.7 shows the calculated bending losses of this new waveguide structure as a function of bending radius $\rho$ and number of lateral ribs $N$, again for TM polarization. Due to the lower index contrast, a higher number of lateral waveguides are needed to reduce the radiation losses compared with the InP technology. A bending-loss reduction factor of around 10 is reached with 9 lateral waveguides. Naturally, there is no a priori limitation in the number of lateral buried waveguides that can be defined in the outer side of the bend. Therefore, it would be possible to reduce optical power leakage just defining more than 9 lateral ribs.

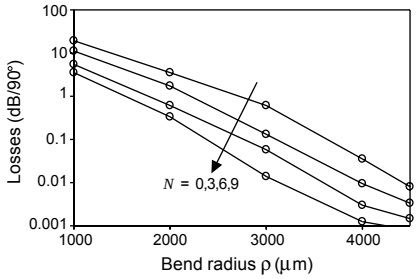


Figure G.7: Bending loss per 90° as a function of bend radius and number of lateral waveguides for the $SiO_2$–Si buried waveguide.

It does not make sense to study the tolerances to possible variations in the etching depth of the silica waveguide because it is a buried waveguide. The influence of possible variations in the width of the lateral ARROW waveguides is shown in Fig. G.6. We see a smooth increase of the loss, which is not worrying from a fabrication point of view.

In conclusion, we have proposed and analyzed a new bend concept based on the ARROW effect provided by a set of properly designed waveguides. These are defined in the same processing step as the central one, and thus, do not require any additional processing. Applicability on InP and Si technologies has been analyzed and significant bending-loss reduction has been observed. The concept is compatible with other bending-loss reduction techniques using one photolithography step, such as S-shaped bends, continuous waveguide widening and bending, and even with multisectional bends [3], as well as with most of the transition loss reduction techniques. It would also be applicable to singlemode fibers.

## References

[1] R. A. Jarvis, J. D. Love, and F. Ladouceur, "Bend-radius reduction in planar waveguides using UV post-tuning," *Electron. Lett.* **33**, 10, 892–894 (1997).

[2] S. Tomljenovic-Hanic, J. D. Love, and A. Ankiewicz, "Low-loss singlemode waveguide and fibre bends," *Electron. Lett.* **38**, 5, 220–222 (2002).

[3] J.-J. Su and W.-S. Wang, "Novel coherently coupled multisectional bending optical waveguide," *IEEE Photon. Technol. Lett.* **14**, 8, 1112–1114 (2002).

[4] C. Seo and J. C. Chen, "Low transition losses in bent rib waveguides," *J. Lightwave Technol.* **14**, 10, 2255–2259 (1996).

[5] L. H. Spiekman, Y. S. Oei, E. G. Metaal, F. H. Groen, P. Demeester, and M. K. Smit, "Ultrasmall waveguide bends: the corner mirrors of the future?," *IEE Proc.-Optoelectron.* **142**, 1, 61–65 (1995).

[6] S. N. Radcliffe and T. P. Young, "New low-loss bend structures for high-density integrated optical switch arrays," *IEEE J. Select. Area. Commun.* **6**, 8, 1169–1177 (1988).

[7] M. A. Duguay, Y. Kokubun, T. L. Koch, and L. Pfeiffer, "Antiresonant reflecting optical waveguides in $SiO_2$-Si multilayer structures," *Appl. Phys. Lett.* **49**, 1, 13–15 (1986).

[8] M. Heiblum and J. H. Harris, "Analysis of curved optical waveguides by conformal transformation," *IEEE J. Quantum Electron.* **QE-11**, 2, 75–83 (1975).

[9] P. Bienstman, E. Six, M. Roelens, M. Vanwolleghem, and R. Baets, "Calculation of bending losses in dielectric waveguides using eigenmode expansion and perfectly matched layers," *IEEE Photon. Technol. Lett.* **14**, 2, 164–166 (2002).

[10] A. Kumar and R. L. Gallawa, "Bending-induced phase shifts in dual-mode planar optical waveguides," *Opt. Lett.* **18**, 17, 1415–1417 (1993).

# Other Publications and Patents

## Journals

- T. Van Caenegem, D. Van Thourhout, M. Galarza, S. Verstuyft, I. Moerman, P. Van Daele, R. Baets, P. Demeester, C. G. P. Herben, X. J. M. Leijtens, M. K. Smit, "Monolithically integrated multi-wavelength laser by selective area growth with metal organic vapour phase epitaxy", *Electron. Lett.*, vol. 37. no. 5, pp. 296–298, Mar. 2001.

- C. Vazquez, C. Aramburu, M. Galarza, M. Lopez-Amo, "Experimental assessment of access guides first-order mode effect on MMI couplers", *Opt. Eng.*, vol. 40, no. 7, pp. 1160–1162, Jul. 2001.

- C. Aramburu, C. Vazquez, M. Galarza, M. Lopez-Amo, J. M. S. Pena, "Mode filter using multimode interference principles: design and tolerance analysis for accessing waveguides supporting two guided modes", *Microw. Opt. Technol. Lett*, vol. 26, no. 2, pp. 140–142, Jul. 2000.

## Conferences

- M. Galarza, K. De Mesel, R. Baets, "Improving the coupling between lasers and optical fibers", RUG-FTW Ph.D. Symposium, Dec. 2002.

- M. Galarza, K. De Mesel, S. Verstuyft, C. Aramburu, I. Moerman, P. Van Daele, R. Baets, M. Lopez-Amo, "Simple to fabricate and highly efficient spot size converters", *SPIE's International Symposium*, Brugge, Belgium, Oct. 2002.

- M. Galarza, K. De Mesel, R. Baets, M. Lopez-Amo, "Modelling of InGaAsP–InP 1.55 $\mu$m lasers with integrated mode expanders using fiber-matched antiresonant reflecting optical waveguides", in *Proc. 10th Eur. Conf. Integrated Optics (ECIO '01)*, Paderborn, Germany, pp. 421–424, Apr. 2001.

- M. Galarza, K. De Mesel, R. Baets, M. Lopez-Amo, "Design of InGaAsP–InP tapered ridge mode transformer using an underlying ARROW cou-

pling waveguide", *IEEE/LEOS Symposium Benelux Chapter*, Delft, Holland, pp. 79–82, Oct. 2000.

- M. Galarza, K. De Mesel, S. Verstuyft, I. Moerman, P. Van Daele, R. Baets, M. Lopez-Amo, "InGaAsP–InP 1.55 $\mu$m lasers with integrated mode expanders using fibre-matched antiresonant reflecting optical waveguides", *European Semiconductor Laser Workshop*, Gent, Belgium, Sep. 2001.

- T. Van Caenegem, D. Van Thourhout, M. Galarza, S. Verstuyft, I. Moerman, P. Van Daele, R. Baets, P. Demeester, C. G. P. Herben, X. J. M. Leijtens, M. K. Smit, "Successful demonstration of active-passive integration technology by selective area growth for realization of photonic IC's", *European Workshop MOVPE IX*, Wrexham, Wales, UK, Jun. 2001.

## Patent applications

- M. Galarza, K. De Mesel, C. Aramburu, R. Baets, "Waveguide taper with lateral rib confinement waveguides", Application number EP02076214.2-2205.